SPECTROSCOPIC IDENTIFICATION OF WATER-OXYGEN AND WATER-HYDROXYL COMPLEXES AND THEIR IMPORTANCE TO ICY OUTER SOLAR SYSTEM BODIES.

By

Paul Cooper, BSc. (Hons)

This thesis is presented for the degree of Doctor of Philosophy of
The University of Western Australia

Chemistry
School of Biomedical and Chemical Sciences

2004

SUMMARY

This thesis studies hydrated oxygen and hydroxyl radicals as a basis for understanding the species formed in the icy surfaces of outer solar system bodies. Infrared spectroscopy is used to identify the species water-oxygen ($H_2O \cdot O_2$) and water-hydroxyl ($H_2O \cdot HO$) complexes in inert gas matrices and presents a new mechanism for O_2 formation in irradiated ices.

The $H_2O \cdot O_2$ Complex

The $H_2O \cdot O_2$ complex was identified in solid argon matrices at 11 K by measuring the infrared spectra of $H_2O/O_2/Ar$ matrices. Absorption bands at 3731.6, 3638.3, 1590.2/1593.6 and 1551.9/1548.8 cm^{-1} were respectively assigned to asymmetric OH water stretching, symmetric OH water stretching, H_2O bending, and the O_2 stretching vibrations. This experimental data was in good agreement with the results of quantum mechanical calculations that predict the vibrational frequencies and intensities for $H_2O \cdot O_2$. These calculations gave a binding energy of 0.72 kcal mol^{-1} for the complex.

The $H_2O \cdot HO$ Complex

The $H_2O \cdot HO$ complex was identified in solid argon matrices at 11 K by measuring the infrared spectra of $OH/H_2O/Ar$ matrices. The OH was formed in a Tesla coil discharge of an H_2O/Ar gas stream. This gas stream also provided the source of H_2O and Ar needed for the experiments. Three absorption bands were assigned to the OH stretch of the hydroxyl group in the complex. These three bands were caused by the occupancy of three different lattice sites. This experimental data was in good agreement with quantum mechanical calculations that predict the vibrational frequencies and intensities for $H_2O \cdot HO$. These calculations gave a binding energy of 5.69 kcal mol^{-1} for the complex.

O_2 Formation in Irradiated Ice

A new mechanism for O_2 formation in irradiated ice is presented. This mechanism draws on experimental evidence in the literature to explain the observations of solid O_2 on or near the surface of the icy Galilean satellites, Europa and Ganymede. It is proposed that on these bodies, hydrogen peroxide, formed from the radiolysis and photolysis of the ice, is present in highly localized aggregates that hinder O_2 diffusion out of the icy surface into the tenuous atmosphere. Further radiolysis and photolysis of these hydrogen peroxide aggregates can then lead to O_2 formation via the formation of a short lived water-oxygen atom complex, $H_2O{\cdot}O$. The O atoms of a pair of these complexes then react rapidly to form O_2.

ACKNOWLEDGMENTS

I would firstly like to thank my supervisor Dr. Terry Quickenden, without whom this thesis would not have been possible. His guidance and advice is very much appreciated. In addition, I would like to acknowledge the invaluable support of Dr. Allan McKinley towards this project.

I must also acknowledge the many helpful discussions with Professor R. E. Johnson of the University of Virginia, as well as Dr. Colin Freeman and Dr. Vaughan Langford, both of the University of Christchurch.

Many thanks must go to Mr. Nigel Hamilton of the Workshop in the School of Biomedical and Chemical Sciences for his excellent maintenance of the matrix-isolation equipment.

Financial support for this thesis has been provided by the Australian Government via an Australian Postgraduate Award and The University of Western Australia with a Completion Scholarship and a Postgraduate Travel Award. In addition, support from the School of Biomedical and Chemical Sciences was provided for travel.

Thank you to all the members of the Quickenden research group that I have had the pleasure of working along side. Thanks also to my friends outside of Chemistry who have always been there to distract me from my university life when needed.

Lastly, I would like to acknowledge the support of my family - in particular my parents, who have put food on the table and a roof over my head. Hopefully now Dad, I *will* be getting a 'real' job.

TABLE OF CONTENTS

Page No.

Page No.

Page No.

LIST OF FIGURES

Page No.

Chapter 1

Chapter 2

Page No.

Chapter 3

Page No.

Chapter 4

Page No.

LIST OF TABLES

PUBLICATIONS ARISING FROM THIS WORK

Cooper, P. D., Johnson, R. E., and Quickenden, T. I. "A review of the possible optical absorption features of oxygen molecules in the icy surfaces of outer solar system bodies" *Planet Space Sci*. **51**, 2003, 183–192.

Cooper, P. D., Kjaergaard, H. G., Langford, V. S., McKinley, A. J., Quickenden, T. I., Schofield, D. P., "Infrared measurements and calculations on $H_2O{\cdot}HO$" *J. Am. Chem. Soc*. 125, 6048-6049 (2003)

Cooper, P. D., Johnson, R. E., and Quickenden, T. I. "Hydrogen peroxide dimers and the production of O_2 in icy satellite surfaces" *Icarus* **166**, 2003, 444–446.

Johnson, R. E., Quickenden, T. I., Cooper, P. D., McKinley, A. J., Freeman, C. G., "The production of oxidants in Europa's surface" *Astrobiology*, **3**, 2003, 823-850.

Cooper, P. D., Kjaergaard, H. G., Langford, V. S., McKinley, A. J., Quickenden, T. I., Schofield, Robinson, T. W., D. P., "Infrared identification of matrix isolated $H_2O{\cdot}O_2$" submitted.

Conference Papers

Cooper, P. D., Quickenden, T. I., Ennis, C. E., Johnson, R. E., "The Production of Oxygen by Radiolysis and Photolysis of Ice", Asia-Oceania Geosciences Society, 1st Annual Meeting, Singapore, July 2004.

Chapter 1 – Introduction

1.1 Jupiter and the Galilean satellites

1.1.1. Jupiter

Jupiter is the largest planet in our Solar System and is named after the Roman King of the Gods. Along with Saturn, Jupiter is classed as 'a gas giant', referring to its massive gaseous atmosphere containing primarily hydrogen and helium, as well as small amounts of ammonia, methane, water, carbon dioxide and other constituents (Gehrels, 1976). Unlike the inner planets of the solar system, gas giants do not have a solid surface. Instead they consist of swirling streams of gases that get hotter and denser nearer to the core from the pressure exerted by the atmosphere above. This pressure causes conditions so extreme at its centre that a soup-like dense form of liquid metallic hydrogen is thought to be present (Gehrels, 1976). If Jupiter was 100 times more massive, the extra pressure exerted on the core by the extra mass above would be enough to ignite thermonuclear fusion of this hydrogen and our solar system would then contain two stars.

The large electrical current flow within the liquid metallic hydrogen core of Jupiter induces a magnetic field around the planet. This magnetosphere is the largest object in the solar system and traps plasma in the vicinity of Jupiter and its satellites. Some of these satellites orbit within the magnetosphere, whence their surfaces are bombarded with highly energetic charged particles. Some satellites actually contribute particles to the plasma by the escape of gaseous molecules from their weak atmospheres (Sill and Clark, 1982).

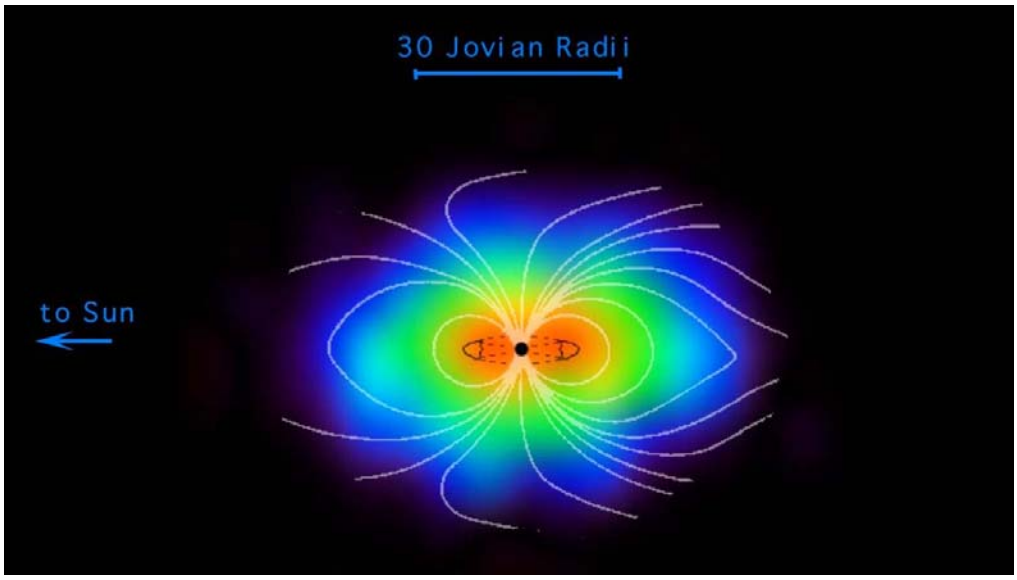

Figure 1.1: *Jupiter's magnetosphere (Image courtesy of NASA/JPL-Caltech)*

For example, Io's volcanic eruptions eject molten sulfur, via volcanic plumes that reach up to 300 kilometres above the satellite's surface, producing a weak SO_2 atmosphere (Johnson and Soderblom, 1982). As Io orbits within Jupiter's magnetosphere about 1000 kilograms of material is lost per second to the magnetic field (Johnson and Soderblum, 1982). Here, it is ionised and a plasma torus of S^+, O^+ and other ions is formed in the wake of Io's orbit. Some of these particles follow Jupiter's magnetic field lines and cause aurora, which are observed at Jupiter's poles. Other particles may drift from the plasma torus and intersect orbits with the other satellites where they bombard their surfaces.

1.1.2. Galilean Satellites

Galileo Galilei first observed four "stars" that appeared to orbit Jupiter in 1610 using a self-made telescope. He quickly realised that these four objects, Io, Europa, Ganymede and Callisto (in order of distance from Jupiter) were not stars, but were in fact moons of Jupiter. This controversial discovery provided evidence against the then accepted notion of an Earth-centred Universe.

The four Galilean satellites are all very different from one another. This thesis is primarily concerned with the two middle satellites, Europa and Ganymede. While the chemistry of Io's volcanoes and atmosphere is very interesting, this thesis relates to the chemistry of the ice present on outer solar system bodies that are exposed to radiation. Io, which possesses no icy surface, is thereby not of interest to the following discussions.

Figure 1.2: *The four Galilean satellites. From left to right: Callisto, Ganymede, Europa and Io. (Image courtesy of NASA/JPL-Caltech)*

The geological activity on the outer Galilean satellite, Callisto, is negligible compared with Io's geological activity. In contrast with Io, whose interior is made molten by the gravitational forces between Jupiter and the other satellites, Callisto is geologically dead. Its four billion-year-old surface is pitted with craters – evidence that no resurfacing of its crust has taken place in this time. Callisto does have a thin covering of ice, but as it is the most outer of the four Galilean satellites, it is not exposed to as much radiation as the inner three.

Ganymede, the third most distant Galilean satellite from Jupiter, is somewhat similar to Callisto in that its surface is thought to consist mainly of ice and rock. Ganymede orbits sufficiently close to Jupiter for charged particles trapped in Jupiter's magnetosphere to bombard its surface. However, Ganymede itself has its own

magnetosphere, thought to be created by an iron core, which interacts with the magnetic field of Jupiter. This interaction results in charged particles, trapped in Jupiter's magnetosphere, bombarding its trailing side (with respect to its orbital motion) and also causes polar aurorae (e.g. Grodent et al. 2003). Ganymede, like the other Galilean satellites, is tidally locked to Jupiter – the same hemisphere always facing Jupiter. The lack of rotation of Ganymede about its own axis means that its leading and trailing hemispheres are always the same geographical hemispheres. This leads to a hemispherical albedo dichotomy where the trailing hemisphere is darker than the leading hemisphere. This is attributed to the plasma bombardment or radiative 'gardening' of the surface on the trailing side.

Europa has the intermediate physical characteristics that one might expect seeing that it sits between Io and Ganymede in the order of the Galilean satellites. Like Ganymede, Europa has an icy regolith. Because of the absence of any significant atmosphere, the radiation chemistry of Europa bears some similarity to that of Ganymede. However, there are some substantial differences between these two neighbouring satellites. Firstly, the surface of Europa is dramatically different in appearance, being extremely smooth in geological terms. The lack of visible cratering is a valuable observation as astronomers determine the age of a solar system body's surface from the number of craters. The flux of meteorite impacts in our solar system is quite well known and so this provides a relationship between the number of craters and the age of a surface. If the surface has many craters, as is the case with Callisto, then it can be inferred that it is old and that there have been no geological processes (volcanism, tectonics, etc) occurring to produce new un-cratered regolith. Conversely, in the case of Europa, there must be a very geologically active process that continually renews the surface (Lucchitta and Soderblum, 1982).

It is believed that as in the case of Io, Europa's core is warmed by its motion through gravitational fields imposed by Jupiter and the other satellites. However, the extent of this tidal warming does not produce the volcanism that Io exhibits, but may be sufficient to melt ice to create a sub-surface ocean. Additional heating from radiogenic sources may also contribute to the melting (Spohn and Schubert, 2003) Furthermore, the presence of salts may act as an 'anti-freeze', to also assist in keeping the ocean from freezing. However, unlike Earth's ocean that is largely liquid at the surface, an icy crust is believed to entirely cap Europa's ocean. Estimates of the thickness of this crust range from a few kilometres to a few hundred kilometres. In any case, it is evident (Lucchitta and Soderblum, 1982) that there are processes available that enable the rapid (in geological time scales) movement of material up to the surface from below, to continually renew the surface. If these processes are indeed occurring then not only is fresh icy material being brought up to the surface, but some of the icy material at the surface which has been altered by radiolysis is being forced down below the surface. The trapped radiolytic and photolytic products are thus subducted within these ice sheets and may provide a source of oxygen to the sub-surface ocean (see Section 1.3). This process makes Europa one of the best possible candidates for finding life beyond the Earth in our solar system.

1.2 Radiolytic and Photolytic Destruction of Ice

While the discussion in Section 1.1 provides an overview of the environment that icy outer solar system bodies are likely to experience, the next question that has to be asked is 'what chemical changes are caused in surface ice when it is bombarded with radiation?'. There is an obvious need to understand the fundamental chemical processes that occur when high energy, damaging radiation is incident upon ice in order to explain

the processes occurring on the surface of icy outer solar system bodies, such as Ganymede and Europa.

Ions and electrons are very damaging to the surface of icy bodies. With each impact, chemical changes occur in the ice. New species such as H, H_2, OH, HO_2, H_2O_2, O, O_2, and O_3 may form as primary, secondary and tertiary products from the destruction of ice. Typically, H atoms are lost from the ice as they diffuse out to the tenuous atmosphere. The gravitational fields of Europa and Ganymede are unable to trap H, and so upon ionisation, this provides a source of protons and electrons that contribute to the plasma trapped within the Jovian magnetosphere. On the other hand, O containing species remain trapped in the icy regolith (Johnson and Quickenden, 1997)

Quite a bit of work has been undertaken over the last 40-50 years to identify radiolytically and photolytically produced species in ice and in understanding the mechanisms by which they are produced. Nevertheless, there are astronomical observations of the icy surfaces of Ganymede and Europa that are unaccounted for by our current understanding of these processes (see Section 1.3). The matter is further complicated because the ices on the cosmic bodies of interest are typically impure. This increases the complexity of the chemistry of such ices compared with pure ice, but at the same time is particularly interesting because of the possibility of forming prebiotic molecules. However, as we still do not fully understand the chemistry of even pure ice, this does indeed pose a problem. In the present study, the chemistry of highly doped ices shall be put aside, and the chemistry of pure ice examined. The initial processes in the decomposition of pure ice are not fully known, but Figure 1.1 shows some of these possible pathways.

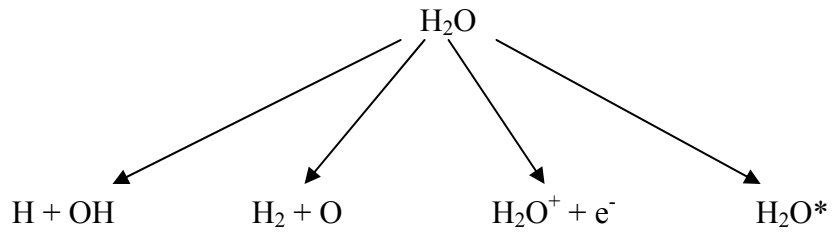

Figure 1.3: *Possible primary products from the radiolytic and photolytic destruction of ice. The pathways shown represent the first step in this process. The above species will continue to react in the system.*

Clearly, there are many possible pathways for the production of secondary and higher order radiation products. Understanding these processes is not trivial because there are many variables (Johnson et al., 2003) such as the type of radiation, the radiation energy, the temperature, the ice morphology, and the ice thickness. Making comparisons between different worker's results can be complicated by variations in these factors. The scientific community needs to develop a more systematic approach to rigorously test the current theories.

1.3 The Implications of O_2 on Galilean Satellites.

The discovery of oxygen molecules on the icy surfaces of Jupiter's satellites, Ganymede (Spencer et al., 1995) and Europa (Spencer and Calvin, 2002) has excited, but puzzled astronomers and astrophysicists alike. Not only is the question of the origin and evolution of the observed oxygen important for these icy bodies, but it is also important for many of the outer planets having satellites with water-dominated icy surfaces. It is also important for cometary nuclei which are also predominantly comprised of water. Furthermore, oxygen ice chemistry is even thought to be important

on grains in the interstellar medium that contain water ice and are exposed to various irradiation environments.

The current emphasis on the search for life processes focuses on oxygen as it is one of the principal energy sources for aerobic biology. Oxygen atoms from dissociated water can oxidize carbon to form carbon dioxide. More complex reactions with carbon, nitrogen and hydrogen form amino acids, the building blocks for proteins. Locating these elements in various chemical forms is an important step in understanding dominant chemical pathways and identifying available energy sources for possible extraterrestrial microbial life.

One of the most exciting possible venues for finding extra-terrestrial biological processes in our Solar System is on Europa. The interior of Europa is tidally warmed by the gravitational forces exerted upon it by Jupiter and the other nearby Jovian satellites. Europa's icy surface is bombarded by Jupiter's magnetospheric radiation, which is the principal driving force for Europa's ice chemistry. This radiation could provide the energy needed to form complex molecules from otherwise labile species. Europa's 'fertile' surface ice (containing oxygen, hydrogen, sulfur, and carbon species) is subjected to irradiative processing by:

- Charged particles in the form of keV-MeV protons and keV electrons from Jupiter's magnetospheric plasma. These are the dominant energy flux incident at Europa's icy surface (Cooper et al., 2001; Paranicas et al., 2001). These energetic particles cause substantial radiation damage extending down to depths of ca. 1 m.

- Solar UV photons which penetrate to depths of ca 1 μm of ice.

- Thermal plasma and pick-up ions dominated by heavy ions deposit energy to depths of a few tens of nm of ice.

As a result of such irradiation, highly reactive unstable molecules and radicals are formed in the ice and these can subsequently react creating new products. For example, the following optically absorbing species reported in the H_2O-dominated surface ice of Europa could all arise (e.g., Johnson, 2001) from such processes: SO_2, SH, CO_2, CH, XCN, H_2O_2, O_2, H_2SO_4, carbonate and sulfate salts. The presence of these species has been inferred from near-infrared (IR) reflectance observations of Europa's surface (Carlson et al., 1999a, b).

The observations of two weak absorption bands in the visible (at 577 and 627 nm) of condensed O_2 absorption bands in the icy regoliths of Ganymede and Europa (Spencer et al., 1995; Spencer and Calvin, 2002) are still not understood. The average surface temperatures of these bodies are ~ 85 - 150 K (Orton et al., 1996). At such temperatures, O_2 should sublime and be lost from the surface to the tenuous atmosphere. The absorption bands observed are characteristic of a dense form of O_2 (see Section 1.4).

Once O_2 is formed in the ice, geological processes such as micrometeorite mixing of the regolith and subduction of icy plates may transport them from the surface into the sub-surface ocean where they could fuel biological activity (Johnson et al., 2003). In competition with this process is the escape of O_2 to Europa's tenuous

atmosphere, as well as loss due to the oxidation of carbon and sulfur species trapped in the ice (Johnson, 2001).

Currently there is no predictive model available which describes the production of O_2 in irradiated cosmic-ice mixtures. In part this is because laboratory investigations are incomplete. Over the past 20 years a number of experiments have been performed to study O_2 formation in ices (e.g., for a review see Johnson et al., 2003). However, these come from a number of groups with different equipment, different methods for forming and measuring the samples, and different types of ionizing radiation. One new insight from recent work by Orlando and co-workers (Sieger et al., 1998; Orlando and Sieger, 2003) suggests that O_2 is formed via a precursor that is stable in the ice over long times. This is also consistent with earlier experiments (e.g., Reimann et al., 1984). Further new theoretical discussions and models for O_2 formation form part of the Results and Discussion section of this thesis and are discussed later in Section 3.3.

1.4 A Review of Oxygen Absorption Spectroscopy Relevant to Cosmic-Ices

In view of the growing interest in oxygen related signals from outer solar system bodies it is important to review the data on oxygen absorption bands available in the literature. Of particular interest is oxygen existing in its solid-state or alternatively as discrete oxygen molecules in a host matrix. The environment provided by the matrices may cause significant spectral shifts or intensity changes and these are given particular attention in this review.

1.4.1 The Absorption Spectroscopy of O_2 in Various Environments

The UV, visible and near-infrared absorption features of the chromophores contained in icy surfaces of outer solar system bodies are useful for interpreting remote spectroscopic studies of such surfaces. Remote studies are usually done using reflectance spectroscopy where the observations show absorption through reduced reflectance at the absorption wavelength. The optical absorption features of pure O_2 and of O_2 contained in ice will now be considered.

A large number of absorption bands have been observed for O_2 molecules in various conditions and states. Regrettably, there is a lack of information about the effect that adjacent H_2O molecules have on O_2 spectroscopy, with only a few cases being reported in the literature. Many of the observations of O_2 absorption bands are from gas-phase measurements and while they will not give a true representation of the behaviour of O_2 embedded in water ice, they do provide a reasonable starting point for such work. A summary of gas-phase O_2 absorption bands is presented in Appendix A.

When there are high concentrations of O_2, such as found in liquid and solid O_2, absorption bands can be altered and additional bands can be induced (Landau et al., 1962). It has been suggested that the well-established O_2 present (Spencer et al., 1995; Calvin and Spencer, 1997) on the icy surface of Ganymede may exist as a solid. Hence the absorption characteristics of solid forms of O_2 are summarised in Appendix B.

This review is primarily concerned with the optical absorption features of O_2 molecules. However there are also a number of emission bands that may be detectable from irradiated icy surfaces. Matich et al. (1993) have observed part of the Herzberg

emission of O_2 from UV-irradiated ices in laboratory studies. It has consequently been proposed by Johnson and Quickenden (1997) that the emission from O_2, trapped within the icy surface of an outer solar system body, might be detectable from a probe in orbit above the surface. Remote sensing by reflectance spectroscopy has of course been used to examine outer solar system surfaces using ground based and orbiting telescopes such as the Hubble Space Telescope and also by the spectrometers on the Galileo space craft. Although emission features may be important in future studies, the present review is concerned with the subject of absorption features and their possible effects on the reflectance spectra of outer solar system bodies.

While there have not been many extensive experimental studies which fully characterise O_2/H_2O ices under the conditions found on outer solar system bodies, I have attempted to present all the reported UV, visible and NIR electronic absorption bands of O_2 under a variety of conditions, but with an emphasis on situations where O_2 interacts with water lattices and/or other molecules that enhance O_2 absorptions. Many of these absorptions might generally be considered too weak to be measured from the surfaces of outer solar system bodies. However the assignment of two bands in the reflectance spectrum of Ganymede to weak O_2 absorption bands (Spencer et al., 1995; Calvin et al., 1996), suggests even such weak bands may be important in telescopic studies. Alternatively, these bands may be enhanced by the H_2O matrix.

1.4.2. The Herzberg Absorption Series

Herzberg observed a series of gas-phase absorption bands in molecular oxygen between the wavelengths of 240 and 270 nm (Herzberg, 1932). Herzberg assigned these absorptions to the symmetry forbidden transitions of the $A\ ^3\Sigma_u^+ \leftarrow X\ ^3\Sigma_g^-$ series. This system is designated as the Herzberg I series. The additional Herzberg

II($c\ ^1\Sigma_u^- \leftarrow X\ ^3\Sigma_g^-$) and Herzberg III ($A'\ ^3\Delta_u \leftarrow X\ ^3\Sigma_g^-$) series were observed by Herzberg (1953) as weak lines amongst the much stronger Herzberg I lines. A detailed discussion of the identificatory history of these lines has been provided by Matich et al. (1993).

The transitions in all of the Herzberg series are electric dipole forbidden and are thus very weak. This is shown by the very small oscillator strengths in Appendix A. However, the Herzberg electronic transitions are important with regards to the photochemistry of O_2. The *A*–*X*, *c*–*X* and *A′*–*X* absorption bands converge at 242 nm at which molecular O_2 dissociates to produce O(^3P) atoms, which in turn can react with other O_2 molecules to produce ozone (O_3). While this is not the dominant photo-dissociation channel for producing O_3, it does contribute to its overall production.

Ozone has recently been tentatively assigned to a band observed in the reflectance spectra of a number of icy satellite surfaces (Noll et al., 1996, 1997). If stable quantities of oxygen on outer solar system bodies are exposed to high-energy radiation, then this pathway will produce O_3.

$$O_2 + h\nu \rightarrow O + O \quad (1)$$

$$O + O_2 \rightarrow O_3 \quad (2)$$

Although many of the O_2 absorption bands are weak, O_3 absorption bands in the UV are relatively strong. Ozone is not a primary radiation product of water ice and cannot be produced without the presence of O_2, thus O_3 may act as a "tracer" molecule to diagnose the presence of O_2 molecules on outer solar system bodies.

Gas phase experiments (Merienne et al., 2000) have shown that the *A*–*X* bands in the Herzberg series are ca. an order of magnitude larger than the *c*–*X* and *A′*–*X* transitions. However, this trend is not seen in perturbed O_2 systems where a single O_2 molecule's electronic orbitals are slightly altered by the interaction of a nearby molecule, as is especially the case where the O_2 is embedded in a host matrix. The breakdown of optical selection rules by a solid-state matrix results in the enhancement of the *A′*–*X* transitions (Goodman and Brus, 1977; Slanger and Cosby, 1988). Thus, the normally dominant gas phase *A*–*X* bands are observed to be very weak in comparison with the *A′*–*X* bands in studies of O_2 in nitrogen, argon and xenon matrices (Goodman and Brus, 1977).

A further example of a dramatic perturbation of weak absorptions is provided by the weakly bound $(O_2)_2$ gas-phase moiety. Shardanand (1969) has reported that the absorption cross-section of the $A'\ ^3\Delta_u + X\ ^3\Sigma_g^- \leftarrow X\ ^3\Sigma_g^- + X\ ^3\Sigma_g^-$ transition of weakly bound $(O_2)_2$ in the gas phase is ~100 times greater than the corresponding $A'\ ^3\Delta_u \leftarrow X\ ^3\Sigma_g^-$ transition of isolated O_2. Thus, it would appear that even a small interaction from a weakly bound molecule (in this present case another O_2 molecule or in the solid-state matrix case from $(N_2)_x$, Ar_x or Xe_x) can significantly perturb an O_2 molecule, and cause some previously highly forbidden transitions to become more probable. These latter absorptions occur in the same region as the ozone-like features observed from Ganymede. However, due to the weak nature of these transitions, it is unlikely that they contribute significantly to the observed absorption band unless they are perturbed in such a way to further enhance their transition probabilities or unless O_2 was present in sufficient quantities to overcome its weak absorption. There is little experimental research on the UV absorption bands of solid oxygen or oxygen/water

matrices to predict if any such enhancements are likely to contribute to the recent Ganymede observations.

The effects of a weakly bound H_2O molecule on the Herzberg series of solid state O_2 are unknown. However, absorption spectra of O_2-saturated liquid water show greater absorption cross-sections than pure liquid water at wave lengths below ca. 250 nm (Heidt and Ekstrom, 1957). Two processes may contribute to this enhancement.

Firstly, a contribution is proposed from the absorption of a weakly bound $H_2O{\cdot}O_2$ complex. Recent theoretical studies of this complex (Byers Brown et al., 1992; Byers Brown, 1995) have shown that it may absorb a photon in the 200–250 nm region of the UV spectrum (the region of the Herzberg continuum) via the formation of the charge transfer complex $H_2O^+{\cdot}O_2^-$. This also overlaps the region identified as the ozone-like feature on Ganymede. Calculations have also shown that although $H_2O{\cdot}O_2$ is weakly bound, with a calculated binding energy of 0.72 kcal mol^{-1} (Kjaergaard et al., 2002), it may be a significant complex in the gas phase (Svishchev and Boyd, 1998; Vaida and Headrick, 2000). However, no literature has appeared on the existence of such complexes in H_2O/O_2 ices. Irradiated ices containing oxygen and water may well contain stable $H_2O{\cdot}O_2$ complexes that could potentially be significant in the chemistry and spectroscopy of such ices.

A second reason may be a relaxation of the selection rules for the Herzberg bands by complexation of O_2 with a partner molecule. The Herzberg bands are forbidden transitions but the selection rules are indeed relaxed by the formation of say $(O_2)_2$ or $H_2O{\cdot}O_2$, as previously described. There is some evidence (Palmer et al., 1996) to suggest that both the charge-transfer absorption and the enhanced forbidden Herzberg

continuum absorption may occur simultaneously in chemical processes in the Earth's atmosphere.

Like the broad continuum assigned to the H_2O_2 observed at Europa (Carlson et al., 1999b), the absorption of oxygen-saturated liquid water, which is tentatively attributed to the absorption of an $H_2O{\cdot}O_2$ complex (Byers Brown, 1995), has a similar trend to increasing absorption in the far-UV. However the absorption in this region by O_2-saturated liquid water is many orders of magnitude less than that of H_2O_2 (Heidt and Ekstrom, 1957; Molina et al., 1977) and therefore may not contribute significantly to the absorption of oxygen-saturated liquid water.

In H_2O/O_2 ices, such as those proposed to exist on the surfaces of some outer solar system bodies, the above Herzberg series absorptions by O_2 may be important, not only in the better identification and characterisation of such ices, but also in the understanding of their photochemistry. It is clearly of particular importance to carry out more laboratory based research on the existence of $H_2O{\cdot}O_2$ complexes in oxygenated and/or irradiated ices.

1.4.3. The Visible Atmospheric Absorption Series

This series, which dates back to the work of Wollaston in 1802 and Fraunhofer in 1817, was first assigned by Mulliken (1928) to the $b\ ^1\Sigma_g^+ \leftarrow X\ ^3\Sigma_g^-$ transitions of O_2 via the bands observed in laboratory absorption and atmospheric absorption measurements. Newnham and Ballard (1998) have recently applied Fourier transform spectrometry to probe the 762.1 nm (0,0) and 688.4 nm (1,0) b–X transitions. Appendix A summarises this data. Unlike many of the other electronic transitions of O_2 in which high densities enhance the absorption cross-sections, there is no such enhancement of

the $b\,^1\Sigma_g^+ \leftarrow X\,^3\Sigma_g^-$ bands (Dianov-Klokov, 1966). In fact, the integrated absorption cross-section of solid O_2 of this series is smaller than that of gas-phase O_2 as shown in Appendix B, making the $b\,^1\Sigma_g^+ \leftarrow X\,^3\Sigma_g^-$ transition one of the weaker solid O_2 absorption series. For this reason, it is unlikely to be of much significance in the spectroscopy of outer solar system bodies.

1.4.4. The Near-Infrared Absorption Series

The $a\,^1\Delta_g \leftarrow X\,^3\Sigma_g^-$ series of O_2 was first predicted by Mulliken (1928) and was first observed by Ellis and Kneser (1933) in the absorption spectrum of liquid oxygen. Recent work by Smith and Newnham (2000) using Fourier transform spectrometry has provided highly resolved spectra of the $a\,^1\Delta_g \leftarrow X\,^3\Sigma_g^-$ (0,0) and (1,0) bands, resulting in the accurate determination of absolute gas-phase absorption cross-sections.

The gas-phase $a\,^1\Delta_g \leftarrow X\,^3\Sigma_g^-$ O_2 spectra consist of rotational fine structure with an underlying absorption continuum. Smith and Newnham (1999) have shown that these continua can be deconvoluted into two components, one component having a linear dependence on the partial pressure of O_2 ($p(O_2)$) and the remaining component having a quadratic dependence. This suggests that the $p(O_2)$-dependent absorption components are related to the absorptions by a single O_2 molecule, while the $p(O_2)^2$-dependent absorption components are absorptions by an $(O_2)_2$ complex. Smith and Newnham (2000) diluted the O_2 with N_2 and observed an increase in the square dependent component with increasing N_2 concentration, probably due to absorption by an O_2–N_2 transient complex. This may be due to the relaxation of the selection rules for O_2 in the presence of N_2.

With increasing density, and thus with greater perturbation from gas-phase conditions, the $a\,^1\Delta_g \leftarrow X\,^3\Sigma_g^-$ absorption bands, like many of the O_2 absorptions, become more intense (Dianov-Klokov, 1966). As shown in Appendices A and B, the (0–0) and (1–0) bands in the solid-state show an increase in intensity of ca. 4 orders of magnitude compared with those observed in the gas-phase. The integrated absorption coefficient of the (0–0) $a\,^1\Delta_g \leftarrow X\,^3\Sigma_g^-$ band is comparable with the $a\,^1\Delta_g + a\,^1\Delta_g \leftarrow X\,^3\Sigma_g^- + X\,^3\Sigma_g^-$ O_2 absorptions that have been assigned to the 627.5 and 577.2 nm features on Ganymede. The (0–0) and (1–0) $a\,^1\Delta_g \leftarrow X\,^3\Sigma_g^-$ bands of O_2 may contribute to the absorption in the regions of ~1050 and ~1250 nm that are observed on a number of the icy satellites. This is a region where water has two weak absorption bands (Calvin et al., 1996). However, the effects of grain size, hydrated minerals (McCord et al., 1999a, b) and temperature (Grundy et al., 1999) complicate the interpretations of these absorption bands. The possible contribution of O_2 absorption has not been thoroughly explored although Calvin et al. (1996) proposed that O_2 absorption in this region might be significant.

Grundy et al. (1999) have reported reflectance spectra for a number of Jovian, Saturnian and Uranian satellites. All of these spectra show relatively strong absorptions at 1.5 and 2.0 μm that are characteristic of water. However, we note that the spectra of Europa and Ganymede show considerably greater band depths for the 1.25 μm band than those of all the other icy satellites examined. Due to the large number of variables that affect absorption bands in this region, it is difficult to know the reason for these differences. However, the possibility that the differences in the 1.25 μm region of the

spectra are due to O_2 absorption must be considered, along with the possibility they may be due to grain size, the presence of hydrated minerals and temperature differences.

1.4.5. The Schumann-Runge Absorption Series

The Schumann–Runge bands of oxygen are the most extensively studied bands of molecular oxygen, and arise from the most intense transitions. These bands occur in the UV region between 175 and 200 nm as 20 absorption features representing transitions from the $X\ ^3\Sigma_g^-$ ground vibrational state to the excited $B\ ^3\Sigma_u^-$ state, as shown in Appendix A. Electronic transitions to the $B\ ^3\Sigma_u^-$ excited state from vibrationally excited $X\ ^3\Sigma_g^-$ states of O_2 have also been observed but only at high temperatures (Hudson and Carter, 1968) and thus can be disregarded in the present discussion.

The Schumann–Runge system plays an important part in O_2 photochemistry. Not only does the Schumann–Runge absorption continuum result in photodissociation of O_2 in the 135–175 nm region to O(^1D) and O(^3P) atoms, but the $B\ ^3\Sigma_u^-$ state is intersected by the repulsive $^3\Pi_u$ state, providing an additional source of O(^3P) atoms via predissociation from a majority of the $B\ ^3\Sigma_u^-$ upper states (Krupenie, 1972). Therefore atomic oxygen produced by photolysis must be accounted for not only by absorption in the Herzberg (O(^3P) + O(^3P)) and Schumann–Runge (O(^3P) + O(^1D)) continua, but also by predissociation from the Schumann Runge absorption bands that provide an extra source of O(^3P) atoms from absorption in the 175–195 nm region.

The spectrum of the Schumann–Runge region of solid oxygen (Romand and Granier-Mayence, 1954) shows an absorption continuum in the 150–200 nm region. No

vibronic bands were observed in that work. These workers suggested that the absorption bands may have been too weak to be observed with the sample thickness used and the resolution of their equipment may have not been adequate. Observations using thicker samples were not possible due to diffusion of the incident radiation.

1.4.6. Condensed O_2 Dimer Absorption Series

These absorption features are currently attracting considerable attention. The so-called O_2 dimer absorptions $a\ ^1\Delta_g + a\ ^1\Delta_g \leftarrow X\ ^3\Sigma_g^- + X\ ^3\Sigma_g^-$ at 627 and 577 nm have been assigned to spectral features observed from the surface of Ganymede (Spencer et al., 1995; Calvin and Spencer, 1997), Europa and Callisto (Spencer and Calvin, 2002). High-pressure gas phase, liquid and solid phase O_2 is interesting because at these high densities, double electronic transitions can occur between a pair of interacting O_2 molecules. When these occur, the wavelength of the absorption of an interacting O_2 pair is approximately halved compared with the corresponding single electronic transition of an isolated O_2 molecule. Thus, the energy of one photon appears to be split between two electronic excitations of two interacting O_2 molecules.

The phrase *"a pair of interacting O_2 molecules"* has been used here rather than the phrase *"an $(O_2)_2$ oxygen dimer"* because of the implication from the latter designation that high density forms of O_2 exist exclusively as stable discrete dimers. Low temperature, gas-phase studies (Long and Ewing, 1971) have provided some evidence for the formation of stable $(O_2)_2$, but clearly the interaction is not sufficient to induce any significant structural changes in the solid phase, as the analyses of α, β and γ phases of solid O_2 (Jordan et al., 1964; Cairns and Pimentel, 1965) show no evidence for any discrete dimer molecules.

If the intensities of the dimer absorption bands were proportional to the number of dimers present in a sample, then one would expect greater band intensities at lower temperatures where the dimers would be more stable. Dianov-Klokov (1966) however has shown that at a constant density (1.17 g cm^{-3}) the dimer absorption bands increase in intensity by a factor of between 1.41 and 3.14 times over the temperature range 80–250 K. This supports the notion that under these conditions, a collision pair of O_2 molecules is predominantly the main absorbing species. A similar trend is observed for the three solid phases of O_2, but this kinetic model is not applicable to the rigid structures in O_2 crystal lattices. The densities of α-, β- and γ-O_2 (Roder, 1978) are similar enough to not account for the differences in absorption cross-section, so it is likely that the differences in the crystal structure for the phases of solid O_2 affect the degree of activation of these forbidden transitions.

Each phase has a particular band shape. The analysis of the 577 and 627 nm bands observed from Ganymede by Spencer et al. (1995) showed that the features were most like that of β-O_2. While it is clear that β-O_2 cannot exist at the temperatures on the surface of Ganymede (Orton et al., 1996), if other bands in this dimer series could be detected it might be possible to determine the state in which O_2 is present within Ganymede's surface. A recent measurement of the reflectance spectra from O_2 co-deposited on a cold substrate with H_2O shows slight shifts in the $(O_2)_2$ band positions and changes in the band shapes (Vidal et al., 1997; Baragiola and Bahr, 1998). These have been used to suggest that the observed oxygen is not trapped in ice, but this position has been questioned (Johnson, 1999). Very recent work (Calvin et al., 2002) has shown that the band strengths of the absorptions of liquid O_2 are strongly dependent on temperature and density. While previous work (Landau et al., 1962; Vidal et al., 1997; Baragiola and Bahr, 1998) does not provide a precise spectral match in terms of

band position, depth and shape, the systematic approach of making laboratory measurements on O_2 under various conditions (e.g. at different temperatures and densities, as a solid or liquid, and with impurities such as H_2O and/or O_3) provides the best approach for understanding the high-density O_2 spectral features of Ganymede, Europa and Callisto.

1.4.7 Infrared O_2 Absorption

The homonuclear diatomic molecule O_2, is normally infrared inactive under most circumstances. However, the O_2 vibration can become active under special conditions. In solid α– and β-phase pure O_2, factor-group analysis predicts that the O_2 fundamental is forbidden, yet traces of the vibration at 1550 cm^{-1} in the spectra of solid α– and β-phase O_2 have been observed (Cairns and Pimentel 1965). The intensity of this absorption was found to depend on sample preparation and annealing, and so was attributed to defects in the sample that lowered the symmetry. The O_2 fundamental has also been observed in glassy Ar:O_2 mixed crystals (Xie et al., 1997)

Importantly, the above infrared O_2 vibration has been observed in ice. In work, simulating the "dirty" ice that might be found on interstellar grains, the O_2 fundamental was observed in H_2O:CO:CO_2:O_2 (2:2:0.5:1) mixtures at 10 K. Calculations (Kjaergaard et al., 2002) predict that bonding to a single water molecule is enough to induce the O_2 vibration, but the $H_2O{\cdot}O_2$ complex has not previously been identified experimentally to confirm this. Spectroscopically, $H_2O{\cdot}O_2$ is hard to find as the O_2 vibration is calculated to be weak (Kjaergaard et al., 2002), and the H_2O modes are calculated to shift by only a few wavenumbers compared with isolated H_2O (Kjaergaard et al., 2002).

1.4.8. Theoretical Work on $H_2O \cdot O_2$

Byers Brown et al (1992) carried out the first theoretical research into the $H_2O \cdot O_2$ complex but restricted the geometry of their structures to C_{2v}. They investigated 6 such structures and found that structures **1** and **2** in Figure 1.4 were the lowest energy configurations for the distributed multipole analysis (DMA) and complete-active-space self-consistent field (CAS SCF) levels of theory employed. No vibrational data were reported. This may be because of difficulties in converging a configuration to a global minimum.

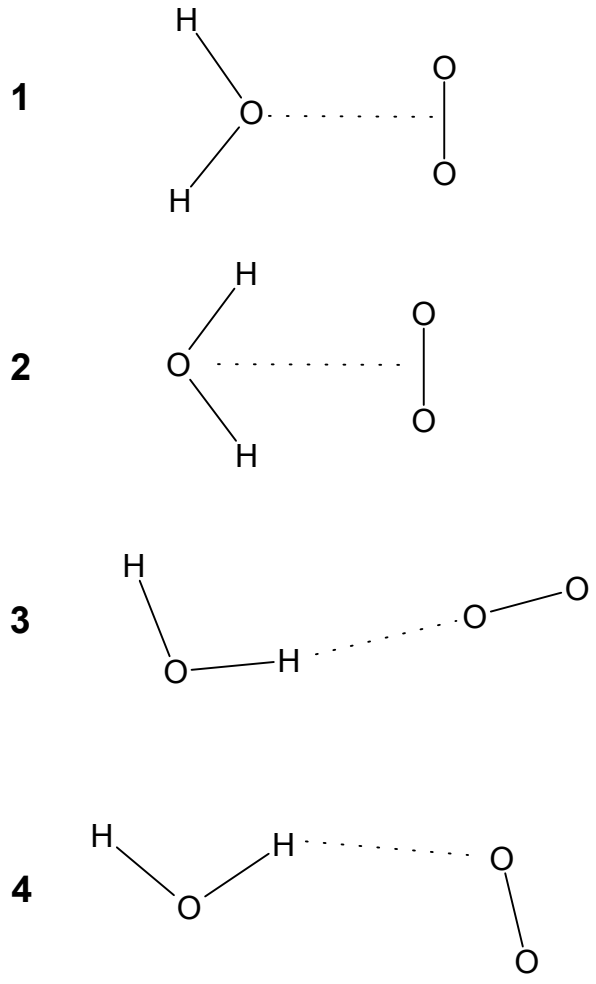

Figure 1.4: *Calculated structures for the O_2 molecule bonded to an H_2O. Structure **4** is the global minimum at the highest level of theory.*

Svishchev and Boyd (1998) later found that using MP2(full), MP4(full) and B3LYP levels of theory, with 6-311++G(2d,2p) basis sets, that the global minimum is a linear "hydrogen bonded" C_s geometry (structure **3** in Figure 1.4). They also calculated vibrational frequencies and intensities. However, Kjaergaard et al. (2002) have recently found that a different structure (**4** in Figure 1.4) is the global minimum using QCISD/6-311+G(d,p) and QCISD/6-311++G(2d,2p) methods. This method has worked effectively on other hydrogen bonding calculations (Kjaergaard et al., 1994). The potential energy surface of the complex is flat enough so that the optimized configuration may be dependent upon the basis set and level of theory used. However, Kjaergaard et al. (2002) found that structure **4** was also the global minimum using the same MP2(full)/6-311++G(2d,2p) method that Svishchev and Boyd (1998) used. The binding energy for this structure is only 0.72 kcal mol^{-1}.

Kjaergaard et al. (2002) also calculated vibrational frequencies for the fundamental and overtone vibrations. However, prior to the present work, as there had been no experimental identification of $H_2O{\cdot}O_2$, no comparison between theory and experiment could be made.

1.5 A Review of OH Absorption Spectroscopy Relevant to Cosmic-Ices

1.5.1 OH Radical in Ice

Absorption of the OH radical has been observed in ice with pulse radiolysis by Taub and Eiben (1968) and with flash photolysis by Ghormley and Hochanadel (1971).

The $A\,^2\Sigma^+ \leftarrow X\,^2\Pi$ absorption of the OH radical in ice at liquid nitrogen temperatures has a maximum at ~280 nm, shifted from ~306 nm in the gas phase (Taub and Eiben, 1968). This perturbation of the upper state will be discussed in later sections. Curiously, OH has not been observed in the surfaces of outer planet icy satellites, but it has been observed in the tails of comets (Feldman 1996) as fluorescence. Emission from highly excited rotational levels between 280 and 330 nm has been observed from cometary bodies (Budzien and Feldman 1991) indicating OH emission is not occurring from the icy core, but from the tail. It is probably being produced from H_2O which is lost from the icy core and dissociated by the solar wind. As will be discussed in Section 1.6.1, $A\,^2\Sigma^+ \rightarrow X\,^2\Pi$ emission from solid ice is not observed (Selby et al., 2004)

1.5.2 The OH Radical in Rare Gas Matrices

A number of workers have investigated the dominant $A\,^2\Sigma^+$-$X\,^2\Pi$ system of OH isolated in rare gas matrices. Robinson and McCarty (1958a, 1958b) first observed matrix-isolated OH in Ar, formed when moist hydrazine was subjected to a discharge and deposited on to a sample window at 4 K. Three bands at 32090, 32155 and 32225 cm^{-1} were observed. The band positions showed a poor correspondence with the rotational structure of gas-phase OH, and were red-shifted by ca. 300 cm^{-1} relative to the gas-phase.

Ten years later Tinti (1968) published absorption and emission spectra of OH and OD in Ne produced in X-irradiated H_2O/Ne matrices at 4 K. The absorption and emission spectra showed well-resolved rotational fine structure for a number of vibronic transitions, bearing no resemblance to the structure found in H_2O/Ar matrices. The structure was interpreted in terms of slightly perturbed rotational motion. Furthermore, the emission spectra showed that the first vibrational level of $X\,^2\Pi$ OH lies 3573 cm^{-1}

above the ground level, which is only slightly blue-shifted from the gas-phase fundamental at 3568 cm^{-1} (Huber and Herzberg 1979).

Brus and Bondybey (1975) further investigated OH/Ne using laser-induced fluorescence spectroscopy. Photolysing H_2O/Ne mixtures, they concluded from their spectra that OH undergoes slightly perturbed free rotation in Ne matrices. This was in agreement with the observations of Tinti (1968). Goodman and Brus (1977) then extended the work by studying OH in Ar, Kr, and Xe matrices. The emission spectra obtained were broad and were increasingly red-shifted along the series Ar, Kr and Xe. The emission lifetimes also decreased along this series. These trends, together with the low frequency anharmonic progressions observed in each of the (0,0), (1,0) and (2,0) vibronic transitions in the excitation spectra, indicated that the OH radical weakly hydrogen bonded to rare-gas atoms.

Work from the present research group (Langford, 1999), also tested whether the $A\,^2\Sigma^+ \longleftarrow X\,^2\Pi$ absorption of OH in an $H_2O{\cdot}HO$ complex occurs at 280 nm, like the well known absorption of OH in ice (Taub and Eiben 1968). However, no absorption at 280 nm was observed. This is in line with recent calculations (Schofield and Kjaergaard 2004) that suggest that a single water molecule, in the form of the $H_2O{\cdot}HO$, does not significantly shift the $A\,^2\Sigma^+ \longleftarrow X\,^2\Pi$ absorption.

1.5.3 Infrared Studies of Matrix-Isolated OH

Acquista et al. (1968) observed two bands at 3452.3 and 3429.2 cm^{-1} in infrared spectra of their photolysed water/Ar matrices. The intensities of these absorptions were greater when the water was photolysed during deposition rather than *in situ*. The bands

were insensitive to the initial water concentration used and to temperature changes between 4.2 and 20.4 K. The frequency shifts measured when O and H isotopes were varied matched those for OH in the gas phase and so the two absorption bands were assigned to OH in two different sites within the matrix. The lack of any temperature dependence ruled out rotation of the radical as the cause of two bands. Acquista et al, (1968) observed that significant amounts of H_2O were present in their matrices and reasoned that one band may possibly be from an OH with all Ar nearest-neighbours, and the other may possibly be from an OH with a nearest-neighbour water molecule. This was not investigated any further.

Later work by Suzer and Andrews (1988) resulted in a slightly different interpretation. While investigating OH^- produced via electron impact, in Ar matrices, significant quantities of OH radical were produced as a by-product of this process. However, Suzer and Andrews (1988) reasoned that neither site arose from an OH with a nearest-neighbour water molecule ie. $H_2O{\cdot}HO$. The hydrogen bond between OH and H_2O should be much greater than the bond between OH and Ar. This would cause a red-shift in the OH stretch of the radical in the water complex compared with the case of OH loosely bound to an Ar atom. If this was the case then the lower energy 3428.1 cm^{-1} band observed would be assigned to $H_2O{\cdot}HO$. However, Suzer and Andrews (1988) also observed that the 3428.1 cm^{-1} band completely converted to the higher energy, 3452.7 cm^{-1} band upon annealing. Water diffuses more readily through the matrix than OH and so one would expect that if the 3428.1 cm^{-1} band originated from the $H_2O{\cdot}HO$, then the band intensity would in fact *increase* upon annealing, not decrease as they observed. Therefore the bands could only be assigned to OH radicals in different sites in the Ar lattice and entirely surrounded by Ar atoms.

In the same year Cheng et al (1988) took an entirely different approach to the problem. Their novel idea was to deposit OH radicals in a matrix without using a water precursor, thus eliminating the problems that interactions with water in the matrix might cause. They achieved this with the use of the following three parallel chemical reactions for the formation of OH:

$$H + NO_2 \rightarrow OH + NO \quad (3)$$

$$H + O_3 \rightarrow OH + O_2 \quad (4)$$

$$H + O \rightarrow OH \quad (5)$$

In each case H atoms were produced from H_2 either in a microwave discharge or by pyrolysis on a tungsten filament.

Remarkably, no absorptions at ~3452 or ~3428 cm^{-1} were observed by Cheng et al. (1988) Instead, a band at 3548.2 cm^{-1} was found and assigned to OH. This value represented a much more sensible 21 cm^{-1} red-shift from the gas phase that is typical of diatomic molecules (Goodman and Brus 1977) as opposed to the 117 and 141 cm^{-1} shifts obtained by earlier studies (Acquista et al, 1968; Suzer and Andrews, 1988). The isotopic shifts for ^{18}OH, ^{16}OD and ^{18}OD were identical to those of gas-phase OH. The absence of ionizing radiation in the sample preparation meant that assignments to OH^- and OH^+ could be ignored.

The assignment of the 3548.2 cm^{-1} band to OH was also in agreement with the electronic studies discussed previously in Section 1.4.2. Goodman and Brus (1977) found that while there was significant bonding between Ar and the $A\ ^2\Sigma^+$ state of OH, the bonding to the ground state was much weaker. The binding energies to Ar for the first excited and ground states of OH were ~750 cm^{-1} and 100 cm^{-1}. The small reduction

in vibrational energy of 21 cm^{-1} observed by Cheng et al (1988) in going from the gas phase to the Ar lattice is also consistent with the weak bond between ground state OH and Ar.

Cheng et al also found that the bands assigned by Acquista et al (1968) to OH were very weak or absent in their experiments. Furthermore, the relative intensities of these bands were inconsistent with the previous work in the field (Acquista et al. 1968; Suzer and Andrews, 1988). Moreover, Cheng et al found that the band at 3548.2 cm^{-1} assigned to OH was irreversibly lost as the temperature was increased to 25 K, while the 3452.3 cm^{-1} band increased correspondingly.

While it now appeared that the assignment of OH in Ar had been resolved, the question of assigning the 3452 and 3428 cm^{-1} bands still remained. Cheng at al (1988) once again raised the possibility of an OH being bonded to a water molecule, but did not investigate this further. Langford et al (2000a) however did decide to pursue this matter and it is discussed in Section 1.5.5.

1.5.4 Theoretical Studies of Matrix-Isolated H_2O·HO

The first theoretical work on H_2O·HO was performed by Hobza and Zahradník (1977). Using the INDO semi-empirical method, they found that H_2O·HO was a stable species with a higher electron affinity than O_2*($b^1\Sigma_g^+$) and OH($X^2\Pi$). While no information regarding vibrational or electronic transitions was calculated, the high electron affinity suggests that H_2O·HO is a stronger oxidant than the free OH radical. In aqueous environments, such as biological systems, the oxidising ability of H_2O·HO may be important and should be further researched.

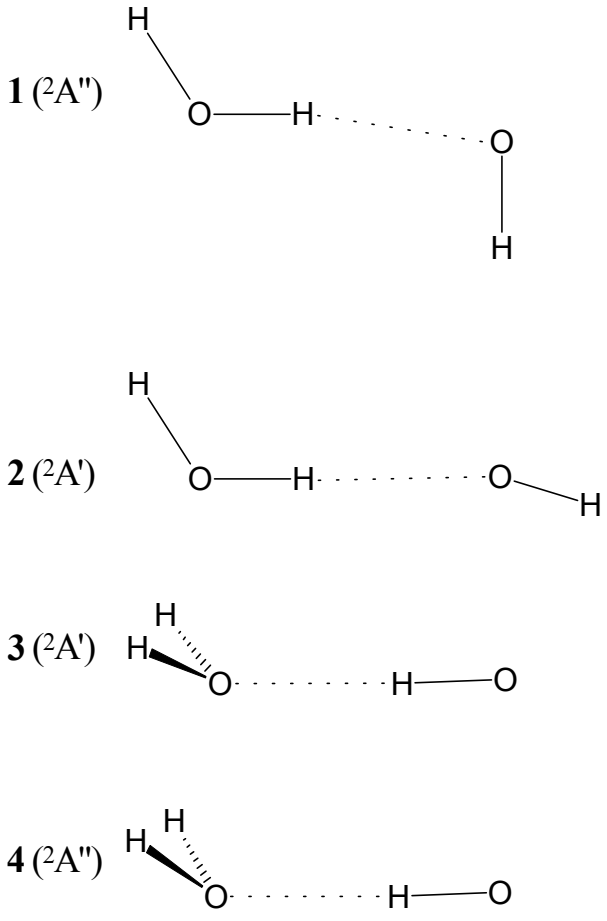

***Figure 1.5**: Calculated structures for the OH radical hydrogen bonded via its O atom to H_2O (**1** and **2**) and hydrogen bonded via its H atom to H_2O (**3** and **4**)*

Bonding to the water molecule may occur through either the OH radical's O atom or its H atom. Early calculations by Kim et al. (1991) treated structures **1** and **2** shown in Figure 1.5. Using ab initio methods, it was found that the bonding of the O atom of OH to an H atom of water was weak. Consequently, the vibrational frequencies for H_2O and OH when bonded together were not significantly different from the free species. It was shown later by Wang et al. (1999) that structure **2** is in fact a turning point and not a true minimum.

Later studies by Xie and Schaefer (1993), using ab initio methods, and work by Wang et al. (1999) using density functional theory (DFT), have shown that the minima presented by Kim et al. (1991) are in fact local minima. The global minimum was achieved when bonding through the water molecule's O atom occurred. Structures **3** and **4** were similar, only differing in the partially occupied π bond on the OH. Structure **3** was the most stable with a binding energy 0.3 kcal/mol greater than for **4**, at 5.6 kcal/mol Xie and Schaefer (1993). The stronger binding energies for **3** and **4** resulted in significant shifts (99 and 81 cm^{-1} respectively) of the O-H stretch of the radical. A ~10-fold increase in intensity of this vibration was also predicted.

Wang et al. (1999) calculated equilibrium geometries and vibrational frequencies for $H_2O{\cdot}HO$ using the DFT method. Their results mostly agree with the *ab initio* results reported earlier by Kim et al. (1991) and Xie and Schaefer (1993) but with slightly large binding energies and with greater red-shifts and intensity enhancements of the OH vibration. Table 1.1 summarises the calculated values obtained from these studies.

1.5.5. The Identification of Matrix-Isolated $H_2O{\cdot}HO$ by Langford et al.

The work on $H_2O{\cdot}HO$ in this thesis carries on from the investigation carried out by Langford et al. (2000a) from this laboratory a few years earlier. In this regard, comparisons between the data obtained presently and the data obtained by Langford et al. (2000a) can be made knowing that the experimental apparatus and experimental conditions have essentially remained unchanged. A discussion of the findings of Langford et al. (2000a) is of course very important to the present work and thus follows.

Langford et al. (2000a) prepared H_2O/OH/Ar matrices by passing a radio frequency discharge from a Tesla coil through mixtures of H_2O/Ar, typically in ratios of 1:70-1:1000 H_2O:Ar. The spectra showed significant quantities of water indicating the discharge was not very efficient in producing radicals. However, much like the earlier work (Acquista et al., 1968; Suzer and Andrews, 1988; Cheng et al., 1988), absorptions at 3548, 3452 and 3428 cm^{-1} were observed indicating that OH was indeed produced. Small signals from HO_2 were also measured. As described in Section 1.5.3, Cheng et al. (1988) had shown that the vibrational energy of the free OH radical in Ar was 3548 cm^{-1}.

Since the last experimental reports of OH in Ar in 1988, the theoretical work described in Section 1.5.4., had predicted red-shifts of the free OH vibration in the order of ~100 cm^{-1} after bonding to water. These matched reasonably well with the experimentally observed shifts of ~96 and 120 cm^{-1} between the true free OH vibrational energy (Cheng et al., 1988) and the earlier mis-assigned energies (Acquista et al., 1968; Suzer and Andrews, 1988).

Langford et al. (2000a) reasoned that if the red-shifted absorptions were indeed from H_2O·HO, then at a fixed OH concentration, they should show a dependence on the water concentration in the matrix. The experiment was complicated by the fact that H_2O was also the source of OH and thus the concentration of OH varied as the H_2O concentration varied. However this was overcome by scaling by the free OH intensity. Langford et al. (2000a) found that while the 3452 cm^{-1} did indeed show a concentration

Table 1.1: *Calculated dissociation energies, rovibrational frequencies (cm^{-1}) and intensities ($km\ mol^{-1}$) for predicted structures of $H_2O \cdot HO$*[a]

Structure	**1**[a]		**3**		**4**	
Reference	1	3	2	3	2	3
Method	RHF[b]	B3LYP[c]	RCISD[b]	B3LYP[c]	RCISD[d]	B3LYP[c]
D_e / kcal mol^{-1}	3.5[e]	3.6	5.7[f]	5.9	5.4[f]	5.5
Complex:						
H_2O a" asym.	4230 (154)	3898 (106)	4075 (104)	3915 (92)	4114 (76)	3912 (88)
H_2O a' sym.	4119 (87)	3749 (139)	3975 (25)	3815 (16)	3996 (20)	3814 (16)
OH stretch (a')	4057 (53)	3703 (35)	3790 (273)	3558 (346)	3813 (214)	3556 (331)
H_2O bend (a')	1773 (84)	1648 (54)	1709 (77)	1639 (74)	1703 (87)	1643 (74)
$OH\cdots OH_2$ torsion (a")			618 (146)	650 (142)	560 (212)	549 (163)
H···OH bend			429 (173)	435 (201)	525 (239)	547 (163)
O···H stretch			184 (16)	197 (97)	190 (58)	213 (213)
H_2O rock			165 (7)	186 (2)	197 (1)	203 (1)
H_2O wag			132 (190)	175 (84)	160 (186)	177 (15)
Isolated species:						
H_2O a" asym.	4245	3927 (62)	4082 (77)	3927 (62)	4123 (43)	3927 (62)
H_2O a' sym.	4142	3825 (8)	3980 (13)	3825 (8)	3999 (9)	3825 (8)
OH stretch (a')	4066	3715 (15)	3889 (23)	3715 (15)	3894 (8)	3715 (15)
H_2O bend (a')	1762	1639 (71)	1708 (78)	1639 (71)	1698 (86)	1639 (71)

Ref. 1 – Kim et al., 1991; Ref. 2 – Xie and Schaefer, 1993; Ref. 3 – Wang et al., 1999.

a) *Intermolecular vibrational modes of structure **1** differ from structures **3** and **4**, so only the water and hydroxyl stretches are shown.*

b) *Triple zeta basis set with two sets of polarization functions (TZ2P).*

c) *Triple zeta basis set with multiple sets of diffuse and polarization functions (6-311++G(2d,2p)).*

d) *Double zeta plus polarization (DZP) basis set.*

e) *Estimated actual D_e from a number of calculations in Kim et al., 1991.*

f) *Computed using the RCISD(Q) method, including Davidson correction.*

---

dependence, the 3428 cm^{-1} band appeared to be independent of water concentration relative to the free OH intensity.

The two absorption bands could originate from the two most stable structures (**3** and **4** in Fig 1.5). The annealing behaviour described in Section 1.5.3 could be interpreted as the conversion of structure **4** (3428 cm^{-1}) into the more stable structure **3** (3452 cm^{-1}). However, this is not likely to be the case. The calculated vibrational frequencies for structures **3** and **4** are very similar and do not account for the 24 cm^{-1} energy difference between the two structures. In addition, structure **3** is the most stable and would be expected to have the most red-shifted band. Experiments (Suzer and Andrews, 1988) show that this band has lower thermal stability. Assigning the less stable structure **1** to this band also does not agree with calculations (Kim et al., 1991; Xie and Schaefer, 1993; Wang et al., 1999) as the OH stretch for this structure is only red-shifted by ca. 10 cm^{-1} (Table 1.1).

Langford et al. (2000a) thus assigned the two bands to $H_2O{\cdot}HO$ occupying two sites in the argon matrix. The 3428 cm^{-1} band was assigned to a thermally unstable site that converted to a more stable site (3452 cm^{-1}) upon annealing (Suzer and Andrews, 1988). The frequency of the former is also independent of water concentration and so that site must be unfavourable at high water concentrations.

In addition to these two bands, Langford et al. (2000a) also observed a third band at ~3442 cm^{-1} that was not observed in the earlier studies (Acquista et al., 1968; Suzer and Andrews, 1988; Cheng et al., 1988). Curiously, the band appeared to show a dependence upon water concentration. However, the band was not assigned because the assignments by Langford et al. (2000a) were based upon a simple concentration dependence study and a re-interpretation this earlier work. As this new absorption had not been observed before, a dependence upon concentration alone, without observing isotopic shifts, was not enough to assign it to $H_2O{\cdot}HO$.

1.6 The Relevance of the Present Study

1.6.1 The Effects of Radiation upon Water Ice

The motivation for much of the present work was a search to understand the effect of radiation on water ice. There have been very many studies over the years investigating ices irradiated with ions, electrons or ultraviolet light and there is still much to learn about the subsequent processes. In recent years, this area has become the focus of workers interested in icy solar system bodies, as described in earlier sections. However, the focus of the Quickenden Group over the last 20+ years has been on the electron- and UV-excited luminescence of ice.

Emissions from both O_2 (Matich et al., 1993) and OH (Selby et al.,2004) have been used to explain the luminescence emitted by UV-irradiated ice. The experimental and theoretical research to be discussed in the following sections is a natural extension of these attempts to understand the chemistry and spectroscopy of such radiation products in ice. These are affected by their interaction with the water lattice, and this thesis is a first step in understanding these interactions. Obtaining such understanding is

not a simple matter so the logical first step is an attempt to understand interactions between a single water molecule and either O_2 or OH.

Emissions from the Herzberg series of O_2 have been observed from UV-irradiated ice and are thought to originate from O_2* excited chemically by the reaction of a trapped O atom with a mobile O atom - both of which are formed from the photolytic destruction of water. As described in Section 1.3, oxygen production in irradiated ice is very important and has been dealt with in sufficient detail in those sections to save repetition here. New developments in understanding the mechanism of O_2 production in irradiated ice will be discussed in Section 3.3.

A fundamental motivation for investigating the interaction between H_2O and OH arises from the UV-irradiated 420 nm luminescence assignment to the $^4\Sigma^- \rightarrow X^2\Pi$ emission of OH. This assignment is interesting because the $^4\Sigma^-$ state of OH is dissociative in the gas-phase. It is also interesting because the $A^2\Sigma^+ \rightarrow X^2\Pi$ emission, which is dominant in the gas-phase, is absent. For a review of the literature see Langford et al (2000b). In that review it is noted there was a correlation between the quenching of the orbital angular momentum of OH and the quenching of luminescence, due to strong hydrogen bonding to the water lattice. This strong interaction between H_2O and OH in ice is proposed in order to make the dissociative $^4\Sigma^-$ excited state associative – which is necessary if it is to emit luminescence. The $^4\Sigma^-$ state in the gas phase predissociates the $A^2\Sigma^+$ excited state. This predissociative crossing in ice however does not evidently result in the dissociation of OH. Instead, the OH in the ice lattice is evidently bound and a long life-time elapses before a photon of the 420 nm luminescence is emitted, returning to the $X^2\Pi$ ground state (Selby et al., 2004)

1.6.2 Relevance to Atmospheric Chemistry

The existence of an $H_2O \cdot O_2$ complex was first proposed nearly 50 years ago. Heidt and Ekstrom (1957) observed an increase in the UV absorption of liquid water when oxygen gas was dissolved in solution. No physical explanation for this phenomenon was available at the time, but it was proposed that complexes of $H_2O \cdot (O_2)_x$ were responsible for this increase of absorption. There has been a renewed interest in the $H_2O \cdot O_2$ complex since it has been suggested (Byers Brown et al, 1992; Byers Brown, 1995) that it is involved in the photonucleation of pure water vapour via the UV absorption of $H_2O \cdot O_2$ to form an $H_2O^+ \cdot O_2^-$ charge-transfer (CT) complex. The large dipole moment of the CT complex subsequently attracts other water molecules and clusters are formed. Cacace et al (2000) have provided experimental evidence for the CT complex. It was found that the complex is metastable with a lifetime exceeding 0.5 μs giving weight to the photonucleation theory and is not only important for the chemistry of water clusters, but for aerosol formation in the atmosphere.

While the $H_2O \cdot O_2$ complex is weakly bound, this does not reflect its possible importance in the atmosphere. It is known that condensed phase reactions occurring in the Earth's atmosphere play a role in atmospheric phenomena such as the formation of the Antarctic ozone hole (Wayne, 1991). Weakly bound complexes, considered as precursors to the condensed phase, are important because perturbations and interactions between the monomer units can alter the spectroscopy and reactivity compared with those of the isolated constituent molecules (Vaida and Headrick, 2000; Hansen and Francisco, 2002) Water is also a major component in the absorption of radiation in the atmosphere and is a key component in the Earth's radiative balance. The high abundances of H_2O and O_2 in the atmosphere may result in sufficiently high levels of

$H_2O{\cdot}O_2$ that can affect the Earth's climate (Vaida and Headrick, 2000; Kjaergaard et al., 2003; Daniel et al., 2004)

The $H_2O{\cdot}HO$ complex may also be important to atmospheric chemistry. The OH radical is one of the main oxidants in the atmosphere (Wayne 1991). Above Antarctica in winter, polar stratospheric clouds (PSC's) form at temperatures of ca. -80ºC. These clouds make up what is termed the 'Antarctic vortex' and are regions of cold, stable air. The nature of the vortex results in cold air essentially being confined within the stratosphere, with very little mixing with air from lower latitudes. Within these clouds, the importance of the $H_2O{\cdot}HO$ complex is unknown. OH is known to destroy O_3, and prevent the formation of O_3 by reacting with O atoms in these regions. Thus the formation of complexes of $H_2O{\cdot}HO$ may have some significance on the O_3 chemistry that occurs within these clouds.

Below 30 km, where [O] is low;

$$OH + O_3 \rightarrow HO_2 + O_2 \qquad (6)$$

whereas above 40 km, where [O] is high;

$$OH + O \rightarrow H + O_2 \qquad (7)$$

It is surprising, to say the least, that there has been little in the way of research to ascertain the roles of $H_2O{\cdot}HO$ in the atmosphere, especially considering quantum mechanical calculations on the $H_2O{\cdot}HO$ complex have predicted it to be a stronger oxidising agent than the free OH radical itself (Hobza and Zahradník, 1977). Considering that OH radicals are critical in the stratospheric destruction of ozone and

are primarily the dominant species involved in daytime oxidation processes within the troposphere (Wayne, 1991), it is important that evidence be sought for the presence of $H_2O{\cdot}HO$ in the atmosphere. It is also important that the spectroscopic properties of this complex, and other water complexes, such as $H_2O{\cdot}O_2$, be fully examined. This is one of the aims of the present study.

Chapter 2 – Experimental Section

2.1 Vacuum Equipment

Matrix isolation spectroscopy requires the use of high vacuum, low temperature equipment. The equipment used in the present work was designed and constructed by Dr. Vaughan Langford (presently at the University of Canterbury) and Nigel Hamilton in the Workshop of the School of Biomedical and Chemical Sciences. Where necessary, modifications to the equipment were made and these are described below. Figure 2.1 shows a schematic diagram of the equipment.

A nominal vacuum of ca. 2 x 10^{-7} Torr (without cooling, < 1 x 10^{-7} Torr when cold) in the matrix-isolation system was achieved by pumping from a single turbomolecular pump (Pfeiffer TPU/H 270). Two such pumps were used as part of the system during the course of this work. One pump with its original bearings was used on the system in the first half of the present work but was removed from use when the bearings became noisy. The spare pump had been rebuilt with new bearings before the commencement of this work. It was fitted into the system and was used for approximately nine months before it suffered a major malfunction which resulted in the destruction of the pump.

Consequently the former pump was rebuilt with new bearings and reinstalled into the system. Shortly before the completion of the experimental work the bearings had once again become noisy and were replaced.

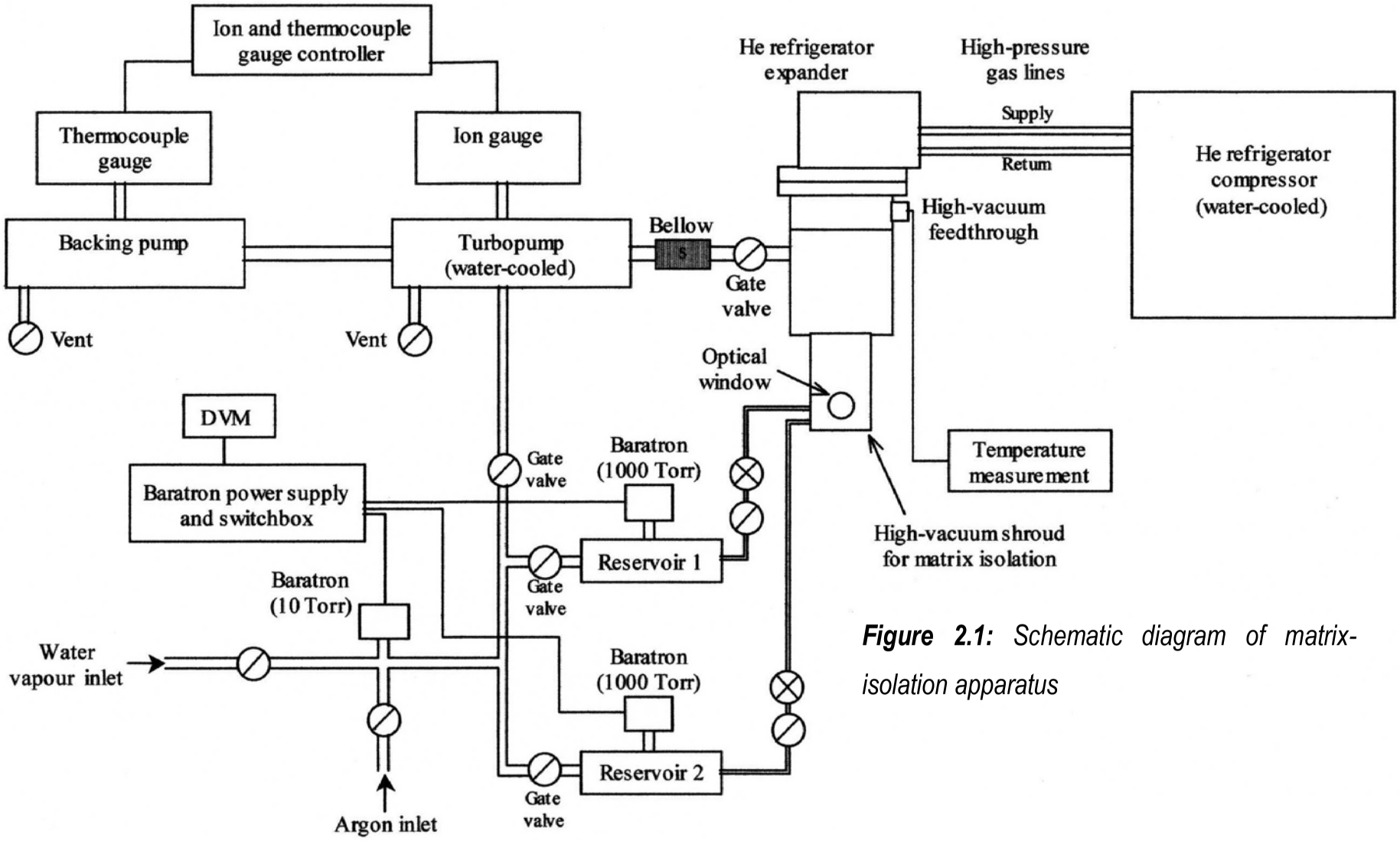

Figure 2.1: *Schematic diagram of matrix-isolation apparatus*

A mechanical pump was used to maintain a backing pressure of ca. 50 mTorr. The vacuum line pressure was measured using a vacuum ionisation gauge (Duniway Model I-075-K) and a vacuum ionisation gauge controller (Varian 843). The backing pressure was measured using a thermocouple gauge.

2.1 Temperature

The cryogenic temperatures required for this work were attained via the use of a closed cycle helium refrigerator (CTI-Cryogenics 8300 compressor and a 350CD displacer). This cooled the sample window (Figure 2.2) down to a base temperature of 11.0 ± 0.5 K. A silicon diode sensor (Lakeshore DT-470) was positioned on the copper sample mount and was used to measure the sample temperature. Indium wire was inserted between the sample window and the copper sample mount to ensure good thermal contact.

Figure 2.2: *Radiation shield, cold finger and sample window*

A temperature controller (Omega CYC3200) attached to a heater was used to control the temperature. The heater originally installed in the matrix isolation system was a kevlar-coated printed circuit heater (Minco HK5160) but was damaged, probably through running the heater too "hot" on the high heater setting of the controller in an attempt to heat the matrix up to 30 K. Consequently a heater (Minco HK5950) which provided a greater heat output was installed in the system.

The old heater was in contact with the cold head via a heat sink comprising of a thin sheet of copper fixed in place around the heater. At ~11 K the stainless steel cold head would contract and may have resulted in poor thermal contact between the cold head and the heater. This may have caused the heater to burn out through excessive heat build up. On inspection, the heater filament appeared to have melted its polymer casing and shorted out, consistent with the above reasoning. As a result, when the new heater was installed a mechanical clamping device was placed around the flexible heater to

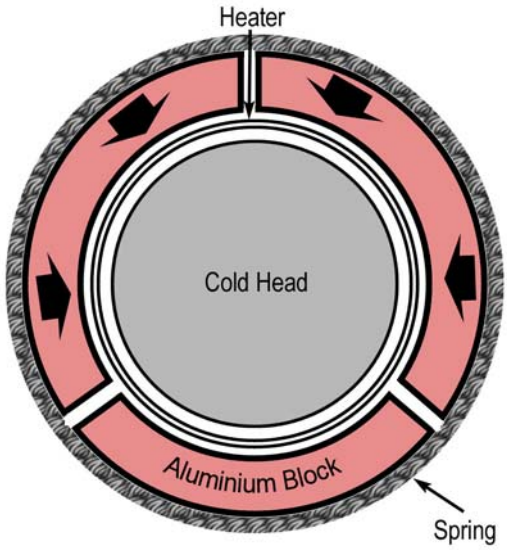

Figure 2.3: *Schematic diagram of the heater assembly.*

ensure good thermal contact at all temperatures. This consisted of 3 aluminium pieces that wrapped around the heater on the cold head. The assembly was held in place via a spring that allowed the three-piece assembly to expand and contract with the cold head (see Figure 2.3)

2.3 Deposition line, mixtures and method

Argon matrices were prepared from gaseous mixtures of argon gas (Air Liquide High Purity Grade) and distilled deionised water vapour using standard manometric techniques. Argon entered the system through a copper pipe from an argon gas cylinder. The pipe was purged with a high flow of argon for 30 seconds to ensure removal of atmospheric gases from the pipe before securing it to the system. Upon entering the system the argon was passed through a trap containing molecular sieves to remove any trace impurity gases in the argon. The argon was then mixed with a chosen vapour pressure of water typically in ratios of 1:70 to 1:1000. Reservoir pressures of 600-800 Torr were typically used. Once prepared the argon/water mixtures were passed through a borosilicate discharge tube, and in the case where $H_2O{\cdot}HO$ was formed, were subjected to a radio-frequency discharge produced from a Tesla coil. When matrix isolation of water alone was required, the discharge was not turned on. Matrices of oxygen (Air Liquide, 99.993% purity), water, and argon mixtures were prepared in a similar manner without any discharge.

For experiments where D_2O was used, the entire vacuum line was pumped down with the turbomolecular pump and the stainless steel reservoirs warmed to remove any adsorbed H_2O on the inner surfaces, before repeating the above applicable method with

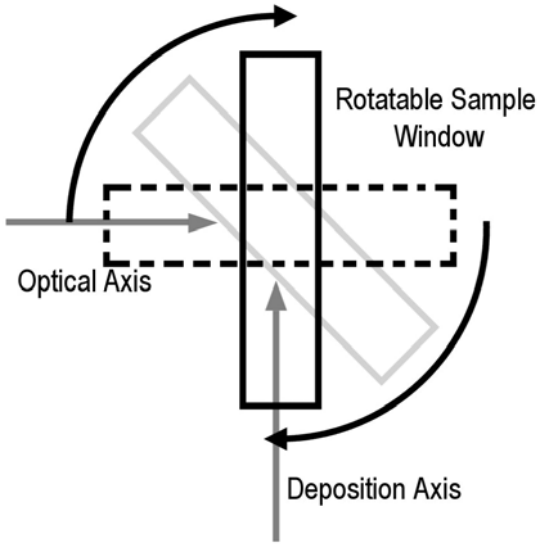

Figure 2.4: *Schematic diagram of rotating cold head showing the sample window position*

distilled D_2O. A similar procedure was then used to remove D_2O after these experiments had been performed.

A rotatable cold head enabled the sample window to be rotated to allow the deposition of the matrix perpendicular to the optical axis of the spectrometer (Figure 2.4). For the present work the gas stream was deposited on to a 2 mm thick, polished potassium bromide (KBr) optical window. Deposition rates of ca. 5-8 mmol h^{-1} were used for all experiments. After the deposition was complete, the cold head was then rotated to align the KBr window so that it was perpendicular to the optical axis of the spectrometer for the collection of a spectrum.

2.4 Spectrometer

A Mattson Sirius 100 FTIR spectrometer with a liquid nitrogen cooled MCT (mercury-cadmium-telluride) detector was used for the present work. Particular care was needed in designing spectroscopic experiments and in executing measurements

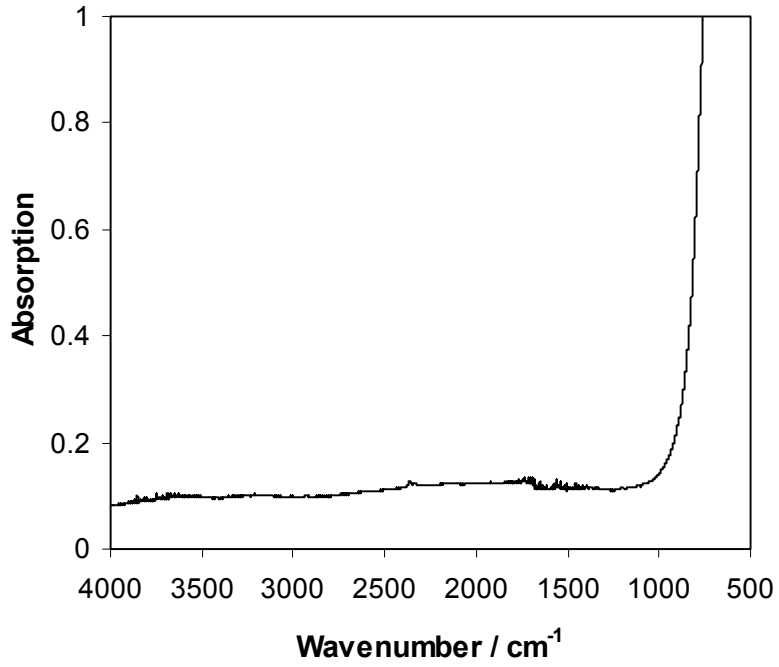

Figure 2.5: *Absorption spectrum of barium fluoride optical windows. A total thickness of 8 mm of window material is shown (1×2 mm and 2×3mm).*

because relatively small absorptions were being measured. Spectra for each sample were recorded at 0.5 cm^{-1} resolution and were collated from 500 replicate scans. Prior to deposition a background scan comprising the mean of 500 replicate scans was also performed with the deposition window in place and was automatically subtracted to remove any absorption from gaseous absorbers (eg H_2O, CO_2 etc) present in the laboratory.

Originally the matrix-isolation equipment was designed and built for use with sapphire windows that were available to the group. This provided the flexibility for use above ca 2000 cm^{-1} in the IR through to the UV. As the primary focus of this thesis was the infrared identification of species, barium fluoride (BaF_2) and potassium bromide (KBr) windows were instead used as outer windows and as the substrate for deposition. The KBr windows were used mainly because of their excellent transmission down to

500 cm^{-1}. The experimental lower limit of 580 cm^{-1} for the equipment, was determined by the sensitivity limit of the MCT detector in the spectrometer.

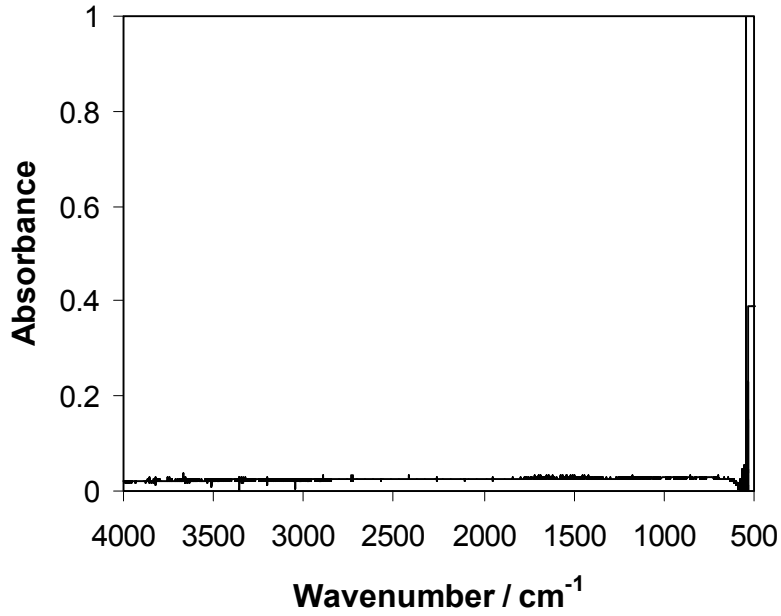

Figure 2.6: *Absorption spectrum of potassium bromide optical windows. A total thickness of 12 mm of window material is shown (1×2 mm and 2×5mm).*

The BaF_2 and KBr outer windows of the matrix-isolation equipment were of different sizes. The BaF_2 outer windows were of the same size as the sapphire windows (ie 3x30 mm), whereas the available KBr windows were (5x50 mm). As a result an adaptor was constructed to allow the use of the different size KBr windows in the system, without major modification to the existing hardware. This is shown in Figure 2.7.

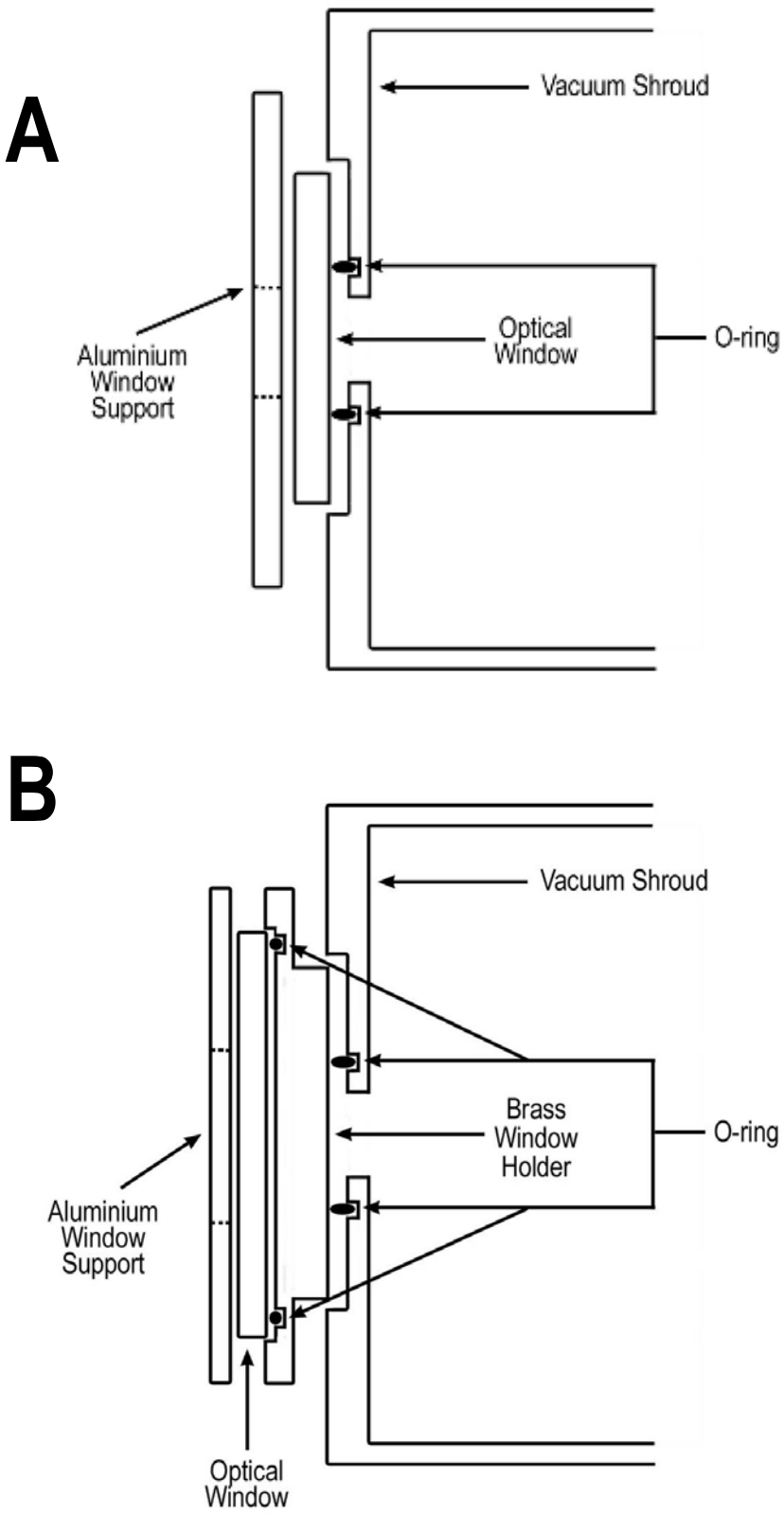

Figure 2.7: *Matrix isolation shroud with 3×30 mm sapphire windows (A) and with 5×50 mm potassium bromide windows (B).*

The spectrometer was under a continuous flow of dry nitrogen in order to purge absorbing species from the optical pathway, but inevitably traces of unwanted atmospheric gases were present in the spectrometer and would occasionally show up as small absorption bands in the spectrum. This was thought to be caused by the fact that the lid of the spectrometer had to be modified considerably for these experiments.

Initially, a new lid was made by the Chemistry Workshop to incorporate the matrix-isolation equipment into the body of the spectrometer. Initially the gaps around the edge of the lid were sealed with a foam strip and adhesive tape was applied to the edge of the lid to secure it in position. Over time this seal gradually became ineffective due to the foam becoming in-elastically compressed and a longer term solution was sought. All-weather rubber door and window lining was adhered to the inside edge of the lid and proved to be a much better barrier against atmospheric leakage into the spectrometer cavity, however background H_2O absorption was still noticeably higher and more variable on days of high humidity.

The mirror velocity of the infrared interferometer was 12.5 KHz for all spectra. At first the spectrometer had intermittent problems that progressively became worse with time. The spectrometer could not find the centre burst – 'the zero pathlength difference (ZPD) point' where the distance between the stationary mirror and the half mirror of the interferometer and the moving mirror and the half mirror of the interferometer were the same. The interferometer would continuously search for the centre burst but was unable to find it on start up which prevented the spectrometer from functioning. After lengthy electronic testing of the spectrometer by Chemistry Workshop staff without any improvement, the bearings on the mirror were replaced as a

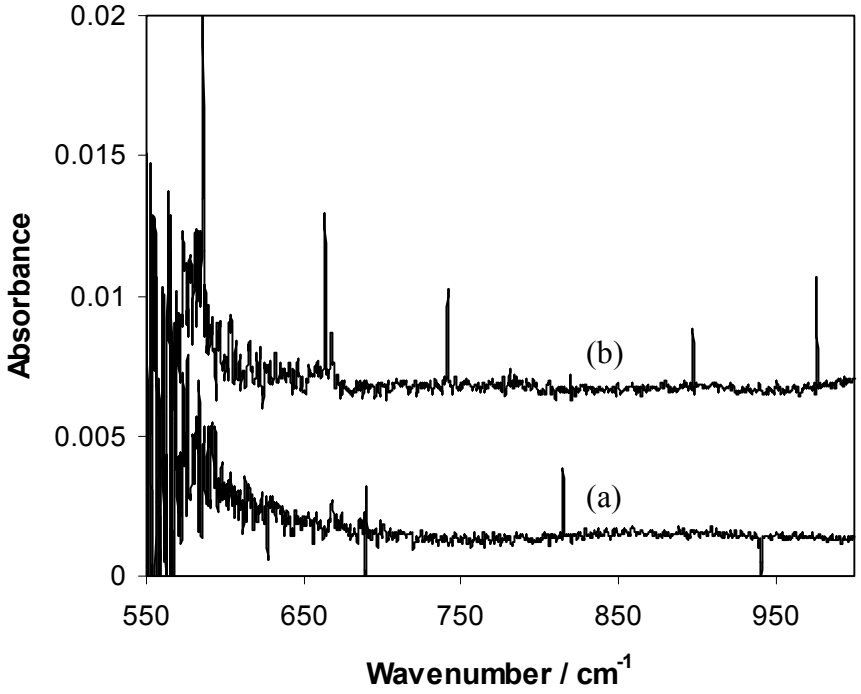

Figure 2.8: *The spectrometer aberrations at 12.5 kHz (a) and 20 kHz (b) mirror velocity. Note that the periodicity of the aberrations increases with decreasing mirror velocity.*

last resort. This corrected the problem, but resulted in small periodic aberrations in the spectra recorded. The periodicity and position of these aberrations were dependent upon the mirror velocity of the interferometer (Figure 2.8). The aberrations varied in intensity from run to run, but they were always quite small in size and more importantly never varied in their position. While not ideal, this was thought to be acceptable, as this did not affect the accuracy or calibration of the spectrometer. Once spectra were recorded, the data was transferred to a computer for analysis.

2.5 Baselining

The spectra obtained during the course of this research all, to varying degrees, showed anomalies in the baseline. Ripples, in what should have been a flat baseline,

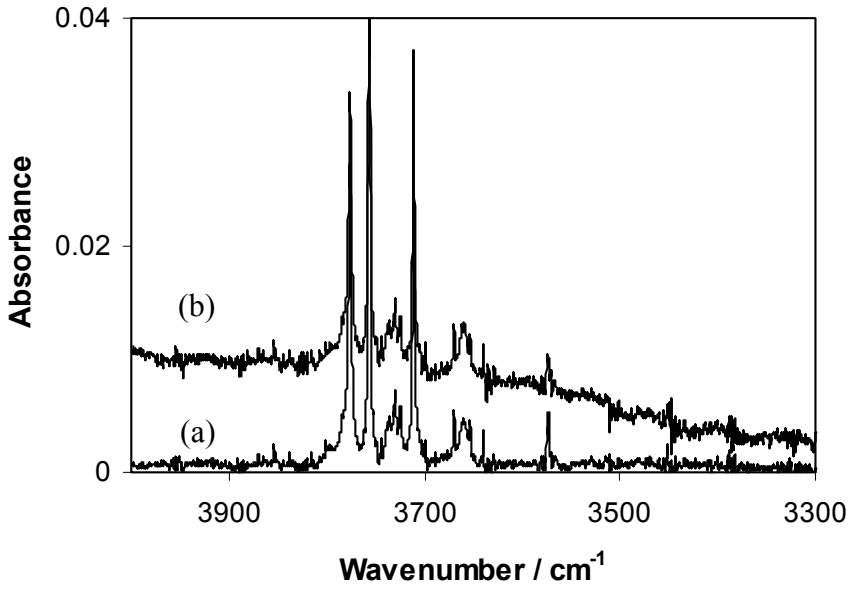

Figure 2.9: *(a) Spectrum of 1:1000 H_2O/Ar after baseline correction; (b) raw spectral data of the same 1:1000 H_2O/Ar matrix.*

were found. This was thought to be a result of slight variations in the position of the sample window relative to the optical beam. The procedure, as outlined above, required a background spectrum to be measured followed by rotating the sample window for deposition, before rotating the window back to its original position, perpendicular to the optical axis. While all effort was made to ensure the starting and finishing positions of the sample window in this process were the same, slight variations (< 1 mm in magnitude) were inevitable.

These ripples are broad and periodic in nature (and are different to the aberrations described above) and so it was determined that the simplest way to deal with this problem was to apply a baseline correction. An example of this process is shown in Fig. 2.9.

2.6 Replicates

While each spectrum obtained was a result of 500 scans of the spectrometer on the same low temperature matrix, more searching replication strategies were also carried

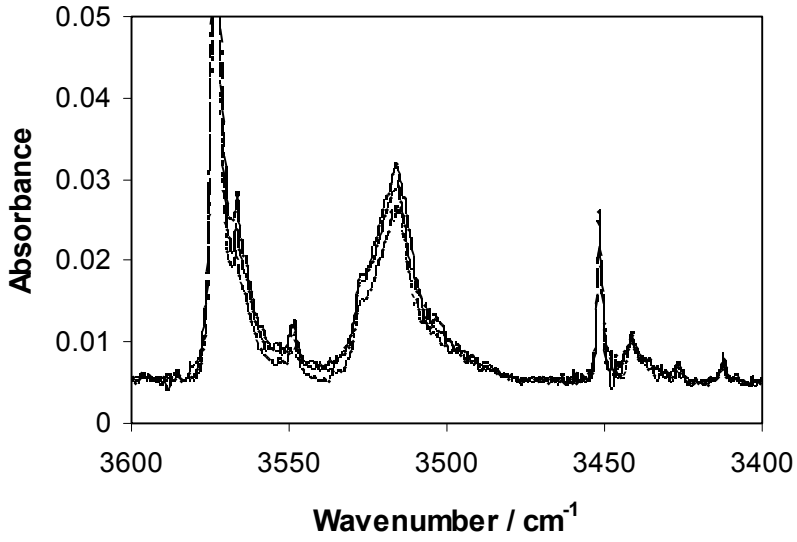

Figure 2.10: *Spectral data from three replicate experiments of discharged 1:100 H_2O/Ar matrices.*

out. This involved running a new, but identical experiment, usually the next day. Each new matrix was slightly different because of slightly different flow rates that were metered manually. Vacuum quality, temperature fluctuations (±0.5 K) and spectrometer performance also affected the data. Such effects were noticeable when spectra were replicated with different matrices as small changes in intensity of some absorption bands, changes in the flatness of the baseline, and also in the signal-to-noise ratio. Nevertheless agreement between experiments on replicate matrices was generally good (see Figure 2.10).

A minimum of three replicate spectra were performed at each matrix concentration for all samples. In cases where large variations were observed between

replicate spectra, further replicates were run, but this was rare. The data from each run were then baseline corrected, as described in Section 2.5, and the three replicates averaged together to produce a 'master' spectrum.

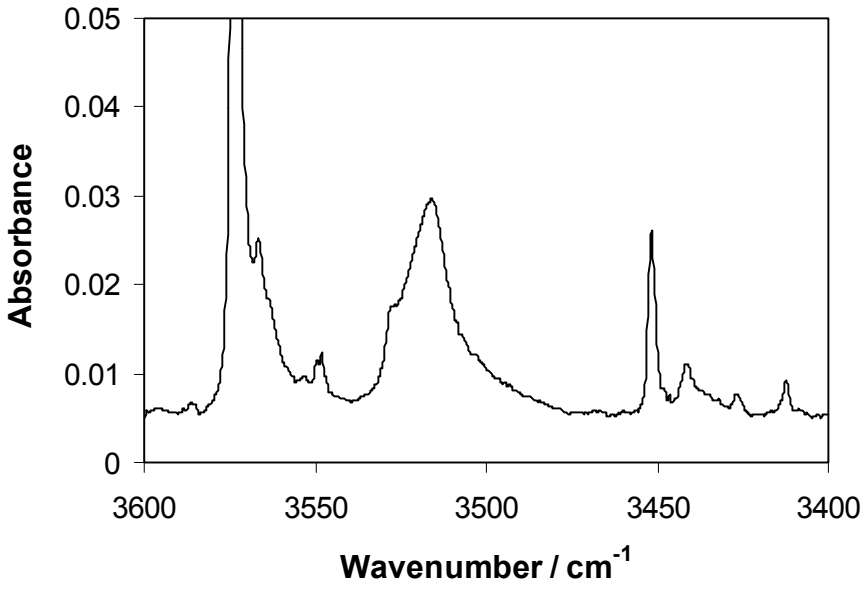

Figure 2.11: *Averaged spectrum of the three replicate spectra shown in Figure 2.10.*

Where replicate measurements could be made upon numerical data, statistical analysis was performed to ascertain the uncertainty in the mean values. This was done by calculating errors at the 95% confidence interval level.

Chapter 3 – Results and Discussion

3.1 The $H_2O \cdot O_2$ complex

3.1.1 Summary of Calculations by Kjaergaard, Schofield and Robinson

The research group of Henrik Kjaergaard at the University of Otago collaborates with the research group of Dr. Quickenden and performed all the calculations discussed in the following chapter. While these calculations to *do not* constitute work carried out by the author of this thesis, a brief summary of their work follows as the results of their calculations are very important to this thesis.

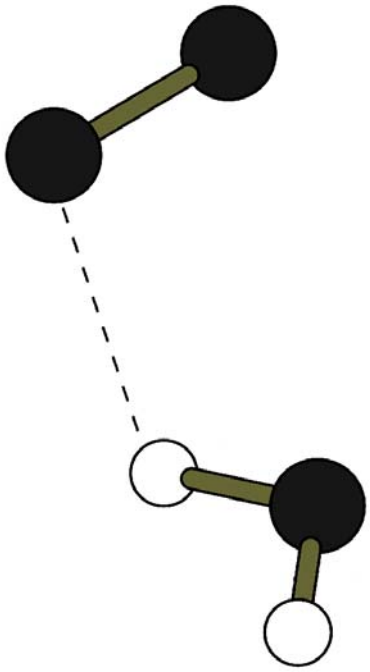

Figure 3.1: *QCISD/6-311++G(2d,2p) optimized structure of the $H_2O \cdot O_2$ complex.*

The structure shown in Figure 3.1 was found to be the global minimum structure given by a quadratic configuration interaction including single and double excitations (QCISD) calculation using a 6-311++G(2d,2p) basis set. A harmonically coupled anharmonic oscillator (HCAO) local mode model was used with Morse oscillators describing the OH-stretching and HOH-bending modes. The frequency of the OO-stretching transition in the complex $\nu_4(H_2O\cdot O_2)$ was predicted by:

$$\nu_4\left(H_2O\cdot O_2\right)=\nu_4\left(O_2\right)+\Delta\nu_4\left(DH\right) \tag{8}$$

where $\nu_4\,(O_2)$ is the observed OO-stretching frequency in molecular oxygen (Krupenie, 1972), and $\Delta\nu_4(DH)$ is the difference in calculated harmonic frequency between the complex and molecular oxygen using the double harmonic approximation as implemented in Gaussian94. Table 3.1 shows the calculated frequencies and oscillator strengths for the vibrations of $H_2O\cdot O_2$

Table 3.1: *Calculated OH-stretching, HOH-bending and OO-stretching frequencies, $\tilde{\nu}$, and oscillator strengths, f, in the $H_2O\cdot O_2$ complex.*

	H_2O		$H_2O\cdot O_2$	
Mode	$\tilde{\nu}$	f	$\tilde{\nu}$	f
ν_4			1551	2×10^{-7}
ν_2	1596	1.29×10^{-5}	1593	1.56×10^{-5}
$2\nu_2$	3148	1.99×10^{-8}	3142	1.82×10^{-9}
ν_1	3658	1.03×10^{-6}	3661	6.55×10^{-7}
ν_3	3755	8.96×10^{-6}	3753	1.08×10^{-5}

3.1.2 Statistical Calculations on the Distribution of Species in an Ar Matrix

Understanding the spectrum of H_2O/Ar matrices is a very important pre-requisite to assigning any possible absorption bands to vibrations of $H_2O{\cdot}O_2$. The method used to co-deposit H_2O and O_2 to form $H_2O{\cdot}O_2$ does not result in high yields of the complex. A random distribution of H_2O and O_2 molecules in the Ar matrix would dictate this. The following is an analysis of the probabilities of occurrence of the various chemical species in the co-deposited matrix.

Argon at 11 K has a hexagonally close-packed (hcp) crystal structure. That is, one Ar atom is surrounded by 12 nearest neighbour Ar atoms. When H_2O and O_2 are co-deposited with Ar I have assumed that the H_2O, O_2 and Ar are the same size and that H_2O and O_2 each replace an Ar atom in the hcp crystal structure. It is also assumed that the interactions between all species are equal as to ensure a pure random distribution. With these assumptions in place, the distribution of H_2O and O_2 molecules is dependent upon the initial H_2O and O_2 concentrations in the gaseous mixture. More simply, and in terms of only H_2O, if the concentration of H_2O is large then there is a greater chance that a single H_2O molecule will have another H_2O as a nearest neighbour and vice versa. Of course, not only is there a probability that the single H_2O will have one nearest neighbour, but two, three, four, and all the way to twelve H_2O nearest neighbours may also occur at differing probabilities. Similar probabilities apply for the number of H_2O nearest neighbours to an O_2 molecule, the number of O_2 nearest neighbours to H_2O molecules, and the number of O_2 nearest neighbours to other O_2 molecules.

The initial expansion of gas from the 600-1000 Torr reservoir to the ~10^{-7} Torr vacuum chamber may have cooled the gas enough to initially form some of the complex. However, the distance between the reservoir and the deposition window (including a right angle turn), and the low binding energy of the complex, most likely resulted in the destruction of any complex formed in the initial expansion. Thus the formation of $H_2O{\cdot}O_2$ should be dependent only on an H_2O and O_2 molecule being deposited as nearest neighbours in the Ar matrix as modelled herein.

Using the above principles and assumptions, the probability, P, that an H_2O has nO_2 as nearest neighbours is thus determined by the following equation:

$$P = {}^{12}\mathrm{C}_n \left(P_{Oxy}\right)^n \left(P_{Ar}\right)^{12-n} \tag{9}$$

where n is the number of nearest neighbour O_2 molecules, P_{Oxy} is the fractional amount of O_2 in the matrix, P_{Ar} is the fractional amount of Ar in the matrix, and ${}^{12}\mathrm{C}_n = 12!/n!(12-n)!$ and is the number of combinations in which n O_2 atoms can be arranged around a single water molecule in an argon lattice. P_{Oxy} and P_{Ar} are simply calculated from the ratios of the gaseous mixtures from which the matrices are deposited.

For a 1:X:1000 H_2O/O_2/Ar mixture (X = 0 - 150) the calculated probability of an H_2O molecule having zero O_2, one O_2 and two O_2 nearest neighbours is shown in Figure 3.2.

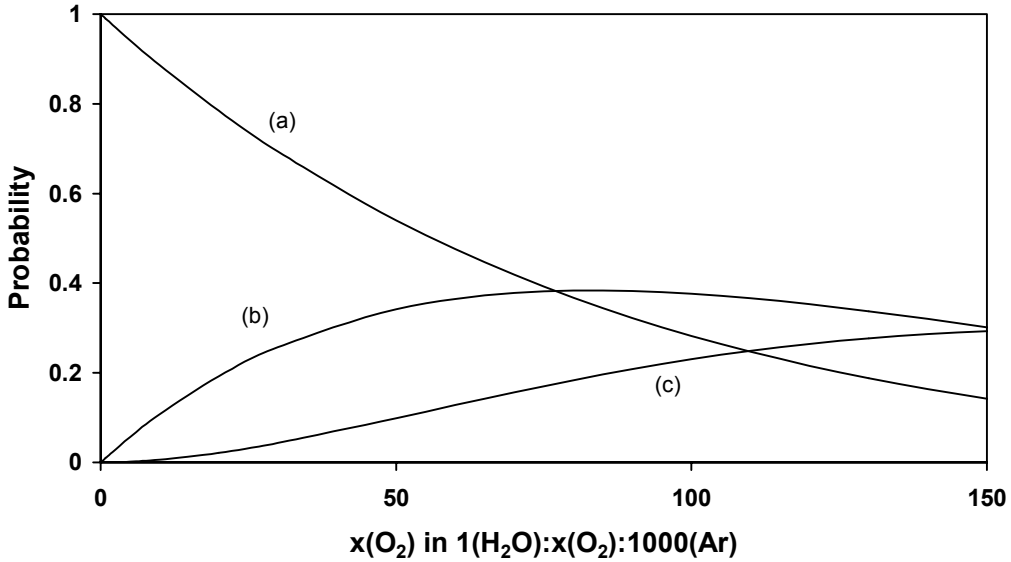

Figure 3.2: *Probability distribution of a single H_2O having (a) no O_2, (b) 1 O_2, and (c) 2 O_2 nearest-neighbors in a hexagonally close-packed argon lattice.*

As is shown in Figure 3.2, the amount of complex in the matrix is small compared with that of water monomer at low O_2 concentrations. Therefore, infrared absorptions from the complex are also likely to be small in comparison with the dominating water vibrations, making observations of these vibrations more difficult. However, it can also be seen that as the O_2 concentration is increased, the amount of complex will increase. So by varying the O_2 concentration, while keeping the much lower H_2O concentration constant, it may be possible to assign absorptions to vibrations of the $H_2O{\cdot}O_2$ complex. Absorption bands that increase in intensity with increasing O_2 concentration should originate from $H_2O{\cdot}O_2$.

3.1.3 H_2O Monomer and Dimer in Ar Matrices

Unfortunately however, spectral assignment is made more difficult by the presence of uncomplexed H_2O monomer and dimer absorption bands, but fortunately,

these bands have been assigned in the literature (Perchard, 2001; Bentwood et al., 1980, Ayres and Pullin, 1976). The next problem which makes assignment more difficult, arises from the behaviour of water in Ar matrices. While rovibrational bands dominate the spectra, earlier workers (Perchard, 2001; Bentwood et al., 1980, Ayres and Pullin, 1976) have found that absorption bands can also be attributed to a non-rotating monomer (nrm) of water. These absorptions lie close to the rovibrational band centres and increase in intensity with increasing water concentration, indicating they are from water. However, they also decrease in intensity with increasing temperature. This is interpreted as the nrm gaining enough thermal energy to overcome the potential barrier needed to rotate freely. It is suggested that the rotation is hindered by inhomogeneity in the matrix, such as lattice defects, or weak interactions with non-nearest neighbour impurities (Engdahl and Nelander, 1989)

It was important to discern the difference between absorptions due to vibrations from nrm and $H_2O{\cdot}O_2$. The disruption of the Ar lattice by O_2 may have caused an increase in the nrm population. This means that a nrm absorption band would also increase with increasing O_2 concentration, making the assignment more complicated. In order to discriminate between the absorptions of nrm and $H_2O{\cdot}O_2$, the spectra of Ar matrices containing *only* H_2O have also been measured. Perchard (2001) has identified bands at 1589.2, 3638.3, and 3736.0 cm^{-1} that exhibit intensity increases with increasing concentration and intensity decreases with increasing temperature. These bands are close to the rovibrational band centres and were assigned to nrm. Figures 3.2-3.4 show the three regions of interest in the infrared. Figure 3.2 shows the region of the spectrum around the asymmetric OH stretch of water. Figure 3.3 shows the region of the spectrum around the symmetric OH stretch of water, while Figure 3.4 shows the

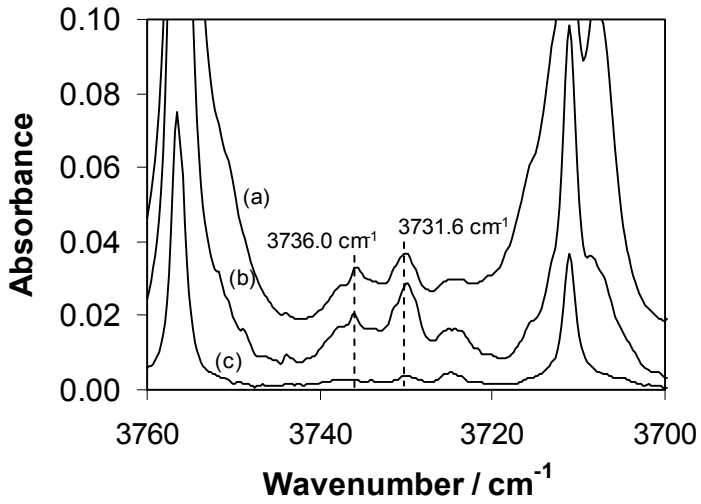

Figure 3.3: *Infrared spectra in the asymmetric OH stretching region of; (a) 1:100 H_2O/Ar; (b) 1:250 H_2O/Ar; and (c) 1:1000 H_2O/Ar matrices at 11.0 K.*

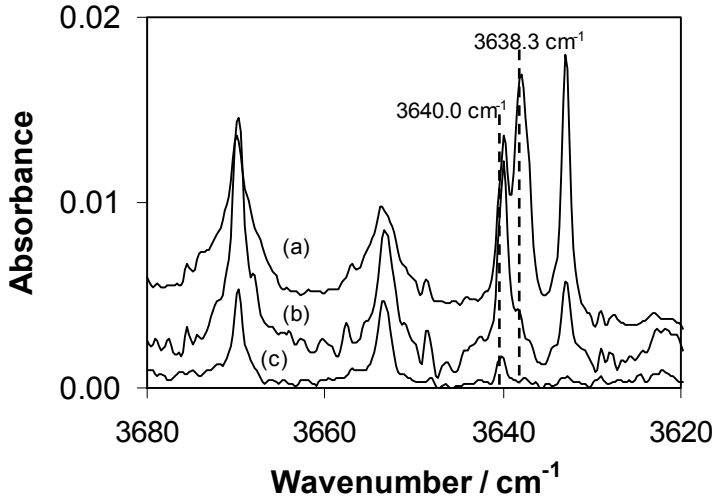

Figure 3.4: *Infrared spectra in the symmetric OH stretching region of; (a) 1:100 H_2O/Ar; (b) 1:250 H_2O/Ar; and (c) 1:1000 H_2O/Ar matrices at 11.0 K.*

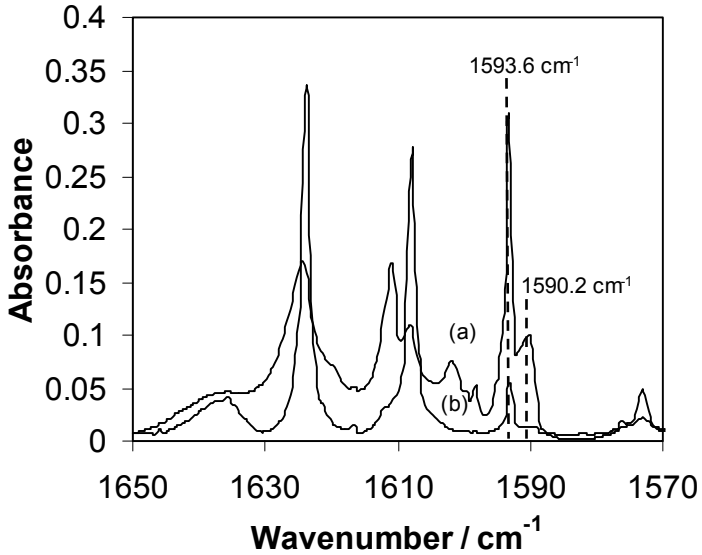

Figure 3.5: *Infrared spectra in the asymmetric HOH bending region of; (a) 1:100 H_2O/Ar and (b) 1:1000 H_2O/Ar matrices at 11.0 K (x5).*

region of the spectrum around the HOH bend of water. The bands observed by Perchard (2001) can clearly be seen to increase with increasing H_2O concentration at 1590.2, 3638.3 and 3736.2 cm^{-1} in the present work. The other bands in the spectra are monomer and dimer bands of water. A summary of these bands in comparison with the work of Perchard (2001) is presented in Table 1.2.

Table 3.2: *A comparison of the absorption bands of H_2O monomer and dimer in Ar matrices as measured by Perchard (2001) and in the present work.*

	Perchard	Present	Perchard	Present	Perchard	Present
H_2O Monomer	ν_3 / cm^{-1}		ν_1 / cm^{-1}		ν_2 / cm^{-1}	
Rovibrational Bands[a]	3711.3	3711.3	3606.8	-	1573.1	1573.2
	3724.9	3725.0	3622.7	-	1607.9	1608.0
	3739.0	-	3653.5	3653.4	1623.9	1623.9
	3756.6	3756.5	3669.7	3669.8	1636.5	1636.7
nrm	3736.0	3736.2	3638.3	3638.3	1589.2	1590.2
H_2O Dimer						
Proton acceptor	3715.7	3715.6	3633.1	3633.2	1593.1	1593.2
	3737.8	3738.0				
Proton donor	3708.0	3707.9	3574.0	3573.5	1610.6	1611.1

[a] *For assignments to rovibrational states, refer to Perchard (2001).*

3.1.4 Assignment of the ν_3 Vibration of $H_2O{\cdot}O_2$

As is shown in Figure 3.6, a reasonably broad absorption at 3731.6 cm^{-1} increased in intensity with increasing O_2 concentration in 1:X:1000 $H_2O/O_2/Ar$ matrices. Fortunately, this absorption occurred in a 'window' between the strong water monomer rovibrational absorption bands. However, the increase of O_2 concentration

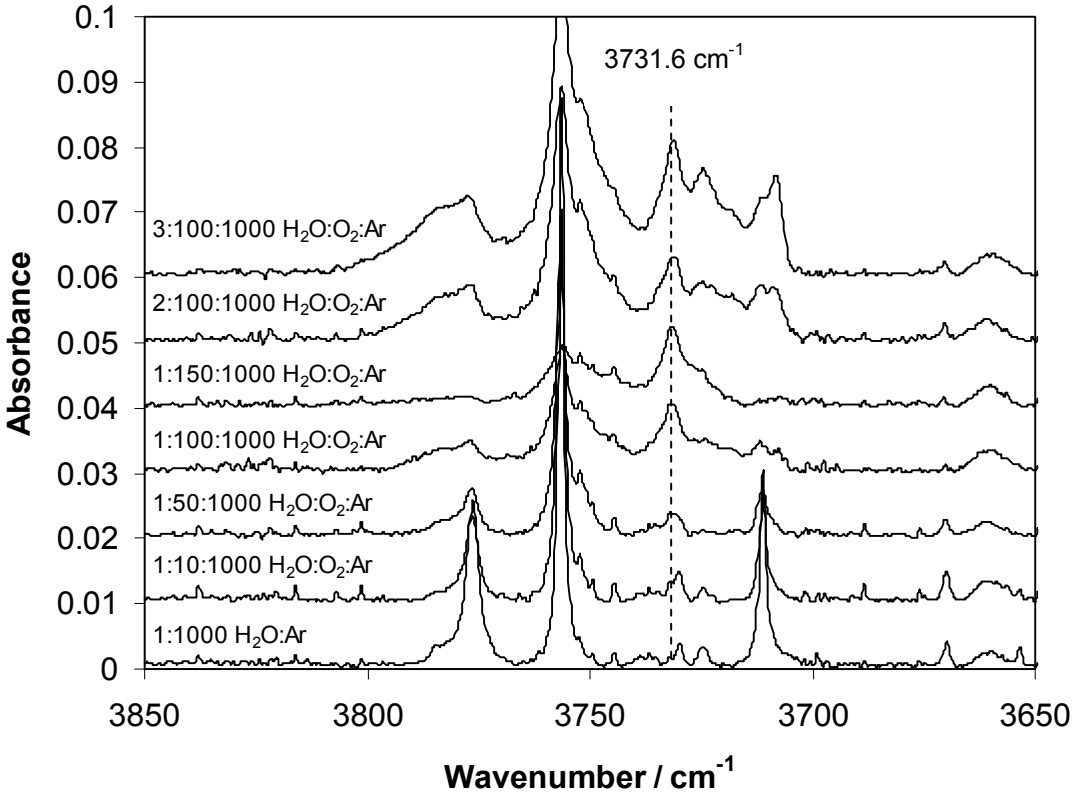

Figure 3.6: *Infrared spectra of H_2O/O_2/Ar matrices at 11 K in the asymmetric O-H stretching region of the IR.*

caused the rovibrational absorptions to broaden and decrease in intensity until they were almost fully quenched at a ratio of 1:150:1000 H_2O/O_2/Ar. From Figure 3.2 it was unlikely that all the water molecules were complexed to an oxygen molecule, but it was more likely that oxygen doped into the argon lattice was sufficient to hinder the rotation of water. This was in agreement with previous studies (Bentwood et al. 1980; Engdahl and Nelander, 1989)

The calculations predicted a 2 cm^{-1} red-shift of the ν_3 vibration of H_2O upon complexation with O_2. Considering the small magnitude of the shifts involved, this was in good agreement with the difference between the ν_3 vibrational frequency of nrm at

3736.2 cm^{-1}, observed in the straight H_2O/Ar matrices, and the 3731.6 cm^{-1} absorption. Importantly, the direction of the shift was in agreement with the calculations.

The intensity of the ν_3 vibration of nrm at a 1:1000 H_2O/Ar ratio was very weak (Figure 3.3) and so a small absorption from nrm was to be expected. At more dilute concentrations of 1:X:3000 H_2O:O_2:Ar (Figure 3.7) absorption from nrm was not expected. This was confirmed with only the 3731.6 cm^{-1} band present at this low water concentration, indicating that the water concentration was too low to detect nrm, even with O_2 in the matrix. The 3731.6 cm^{-1} band was thus assigned to the ν_3 vibration of the $H_2O \cdot O_2$ complex.

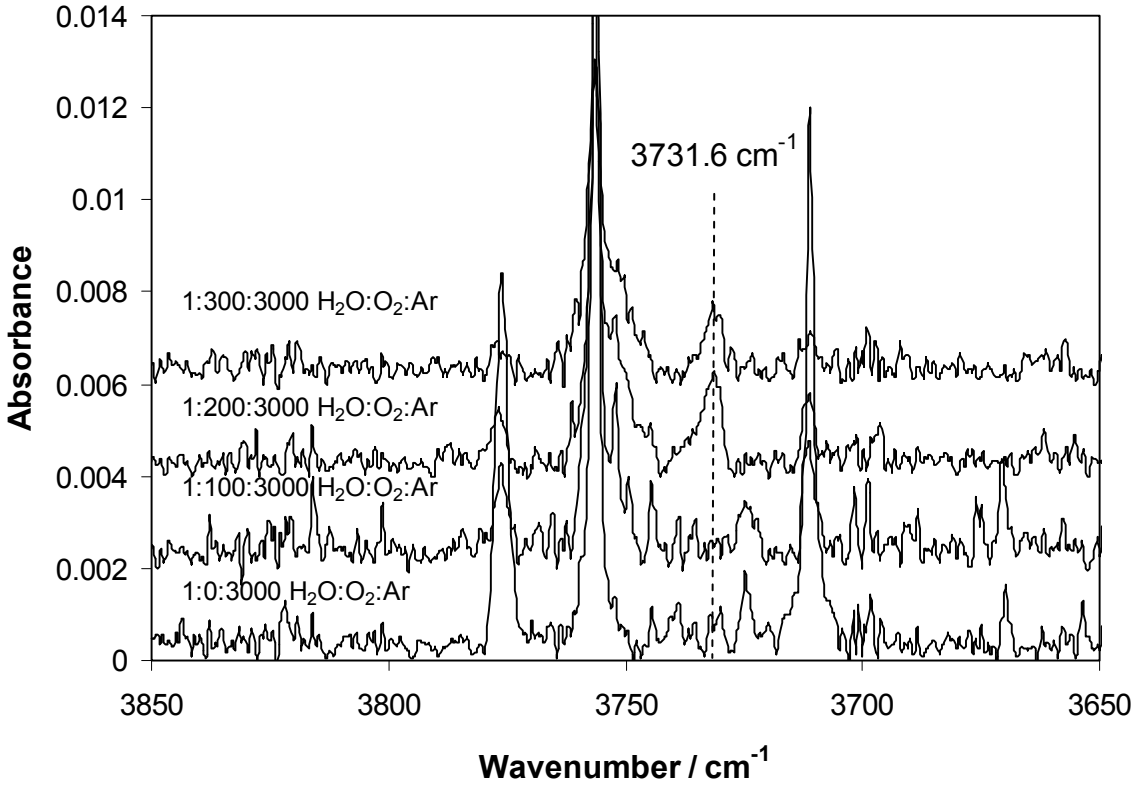

Figure 3.7: *Infrared spectra of 1:X:3000 H_2O/O_2/Ar matrices at 11 K in the asymmetric O-H stretching region of the IR.*

At 2:100:1000 and 3:100:1000 $H_2O/O_2/Ar$ ratios, shown in Figure 3.6, another absorption band was observed at 3725.1 cm^{-1} and was found to increase in intensity as the water concentration increased. The band was seen to grow as a shoulder to the 3731.6 cm^{-1} band in the 1:X:1000 $H_2O/O_2/Ar$ spectra. A rovibrational monomer band was present at 3724.9 cm^{-1}. However, the rovibrational band, clearly observed in the low O_2 concentration spectra, first decreased and was not observed in the 1:50:1000 $H_2O/O_2/Ar$ spectrum. As the fraction of O_2 increased the band emerged at 3725.1 cm^{-1}. The band was not observed in the 1:X:3000 $H_2O/O_2/Ar$.

A vibration of a water dimer was consistent with this behaviour and in fact water dimer was seen in the 2:100:1000 and 3:100:1000 $H_2O/O_2/Ar$ runs through the observation of the 3708.0 cm^{-1} dimer absorption band. The intensity of this band correlated with the intensity dependence upon water concentration of the 3725.1 cm^{-1} band, providing further support for the view that this absorption band was from a species containing a water dimer. While also showing a dependence upon O_2 concentration, this band may possibly be a vibration of $(H_2O)_2 \cdot O_2$. Calculations have not been performed on this species, so the assignment is only tentative at present.

3.1.4 Assignment of the ν_1 Vibration of $H_2O \cdot O_2$

The ν_1 vibration of water monomer was considerably less intense than that of the ν_3 mode. However, the spectra in Figure 3.8 do, as before, exhibit rovibrational absorptions that were quenched as the water molecule's rotation was hindered by the increasing inhomogeneity of the argon matrix. An absorption at 3640.0 cm^{-1} was observed to increase with increasing oxygen concentration in 1:X:1000 $H_2O/O_2/Ar$

matrices. This lies very close to the nrm vibrational frequency of 3638.3 cm^{-1} (Figure 3.4).

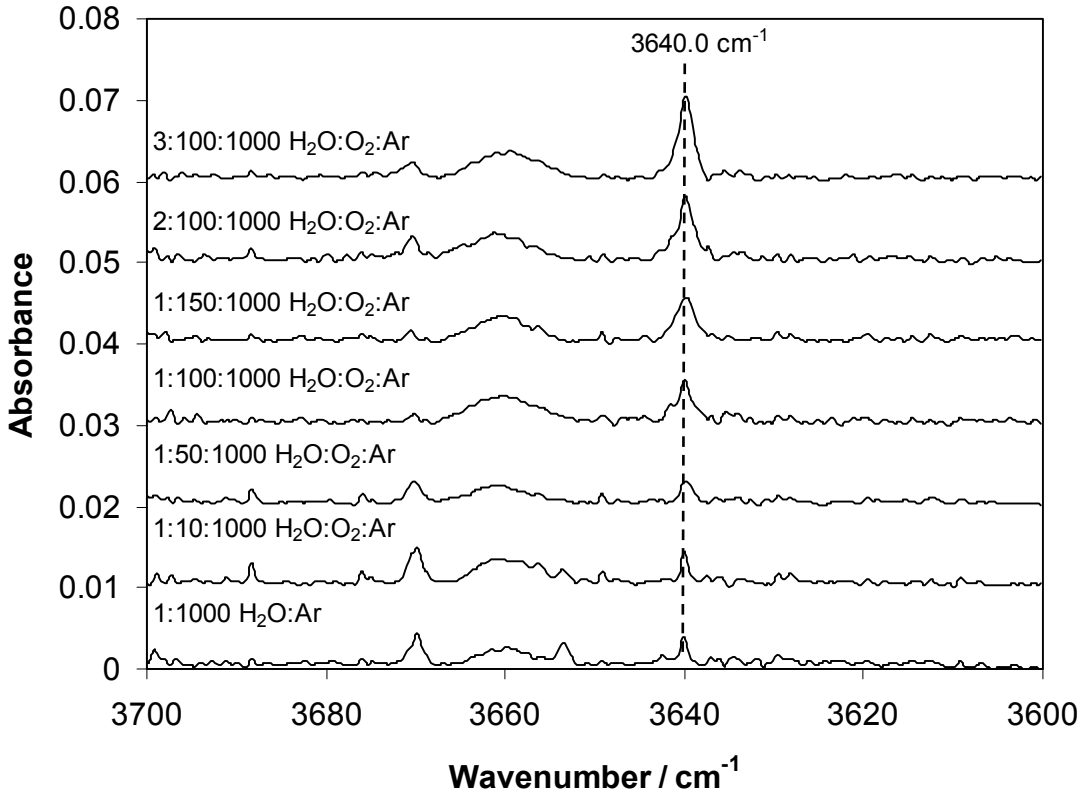

Figure 3.8: *Infrared spectra of H_2O/O_2/Ar matrices at 11 K in the symmetric O-H stretching region of the IR.*

The calculations predicted a blue-shift of 3 cm^{-1} for the symmetric OH stretch in $H_2O{\cdot}O_2$ compared with that in monomeric H_2O. Once again, the size of this shift was in good agreement with the difference between the nrm vibrational frequency and the 3840 cm^{-1} absorption band measured here. Note that the direction of the shift is the opposite of what was calculated for the asymmetric OH stretch, yet the experiment and calculations correlate.

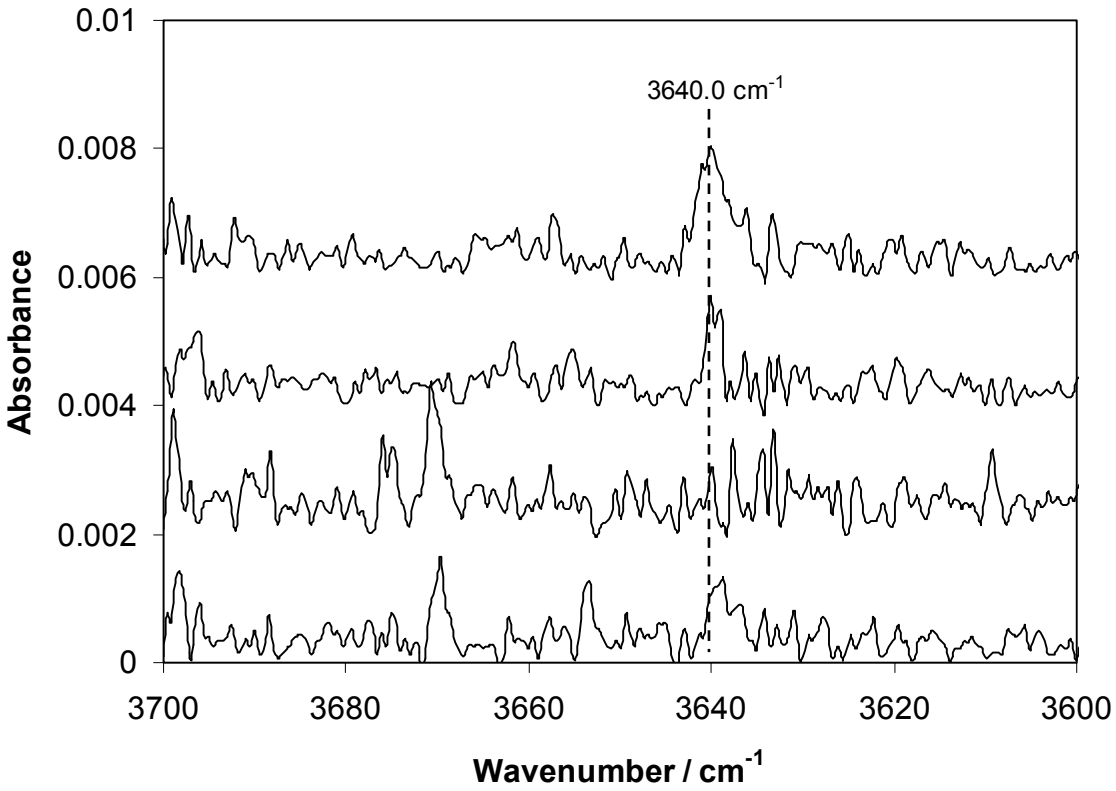

Figure 3.9: *Infrared spectra of 1:X:3000 H_2O/O_2/Ar matrices at 11 K in the symmetric O-H stretching region of the IR.*

Figure 3.9 also shows, however, that an absorption band was observed at 3640 cm^{-1}, even without the presence of O_2 in the matrix. This absorption had not been assigned in previous investigations of matrix-isolated water (Perchard, 2001; Bentwood et al., 1980, Ayres and Pullin, 1976). although it does appear to have originated from water as its intensity was dependent upon water concentration (Figure 3.4). However, in my investigations I kept the H_2O concentration fixed, but still found a dependence upon O_2 concentration, indicating that at least a portion of the absorbance may be attributed to an O_2-containing species. Figure 3.8 also shows that the 3640.0 cm^{-1} band appeared at first to be quenched by the addition of O_2 to the matrix, and then gained in

intensity with larger amounts of O_2. This supports the notion that at least a portion of the absorption band was due to a new species.

The calculations predict that the intensity of the ν_1 vibration of $H_2O{\cdot}O_2$ should be ~15 times less intense than the ν_3 vibration. Experimentally, this ratio is hard to determine accurately because of the overlapping broad bands of the ν_3 vibration, but is estimated to be only ~4-5 times less intense. Nevertheless, with the intensity dependence upon O_2 concentration, and the excellent agreement with the frequency shift of our calculations, the 3640.0 cm^{-1} band is tentatively assigned to the ν_1 vibration of the $H_2O{\cdot}O_2$ complex. There may however be some additional contribution to the absorption at the same frequency from a species other than $H_2O{\cdot}O_2$.

3.1.6 Assignment of the ν_2 Vibration of $H_2O{\cdot}O_2$

The water monomer's ν_2 mode of vibration in an argon matrix was also split into a number of rovibrational lines. Upon increasing the O_2 concentration in the matrix the rovibrational lines are quenched by hindering as described above. Two absorption lines were observed to increase with increasing O_2 concentration (Figure 3.10). The absorption at 1590.2 cm^{-1} showed the strongest concentration dependence, and agrees well with the nrm ν_2 mode of vibration. The intensity of this absorption however was significantly greater than what was expected in comparison to the ν_1 and ν_3 intensities of nrm.

An O_2 dependent absorption band at 1593 cm^{-1} agreed well with the ν_2 proton acceptor (PA) mode of the water dimer (Perchard, 2001). However, the water dimer was not expected to show any dependence upon O_2 concentration in the matrix. The

lack of water dimer in other regions of the spectrum also did not support this assignment. Like the ν_1 vibration, the 1593.6 cm^{-1} band was present in matrices containing only H_2O. One could perhaps argue that the 1593.6 cm^{-1} band was in fact nrm and the 1590.2 cm^{-1} band was $H_2O{\cdot}O_2$. This would agree well with the predicted 3 cm^{-1} red-shift upon complexation but this can not be the case. Nrm is observed in water-only matrices at 1590.2 cm^{-1} (Perchard, 2001), and not at 1593.6 cm^{-1}.

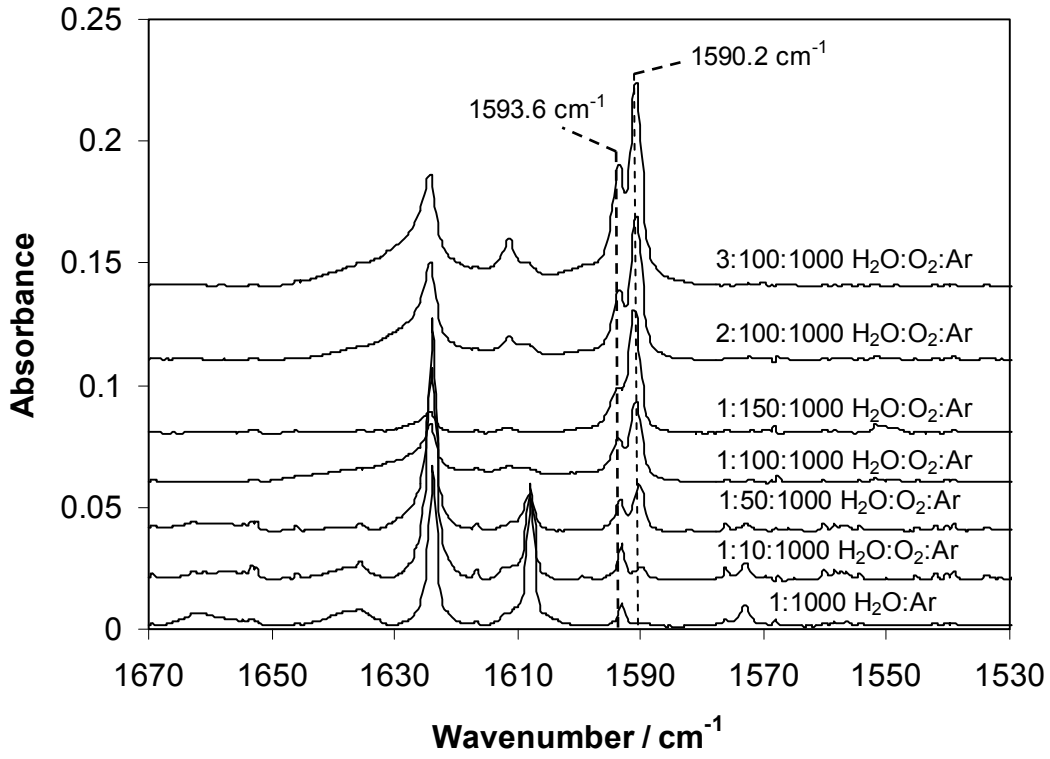

Figure 3.10: *Infrared spectra of H_2O/O_2/Ar matrices at 11 K in the asymmetric HOH bending region of the IR.*

Due to its strong concentration dependence the 1590.2 cm^{-1} band was assigned to the ν_2 vibration of $H_2O{\cdot}O_2$. The 1593.6 cm^{-1} band was also tentatively assigned to the same vibration. While the former frequency was the same as the nrm vibration, the 1:X:3000 spectra in Figure 3.11 indicated that the absorption at these low

concentrations could not be due to nrm because Coussan et al (1997) did not observe nrm at these concentrations in their $H_2O/N_2/Ar$ matrices. This strong evidence also suggested that the intensity of the 1590.2 cm^{-1} band was far too great to come from nrm and so likely came from $H_2O{\cdot}O_2$.

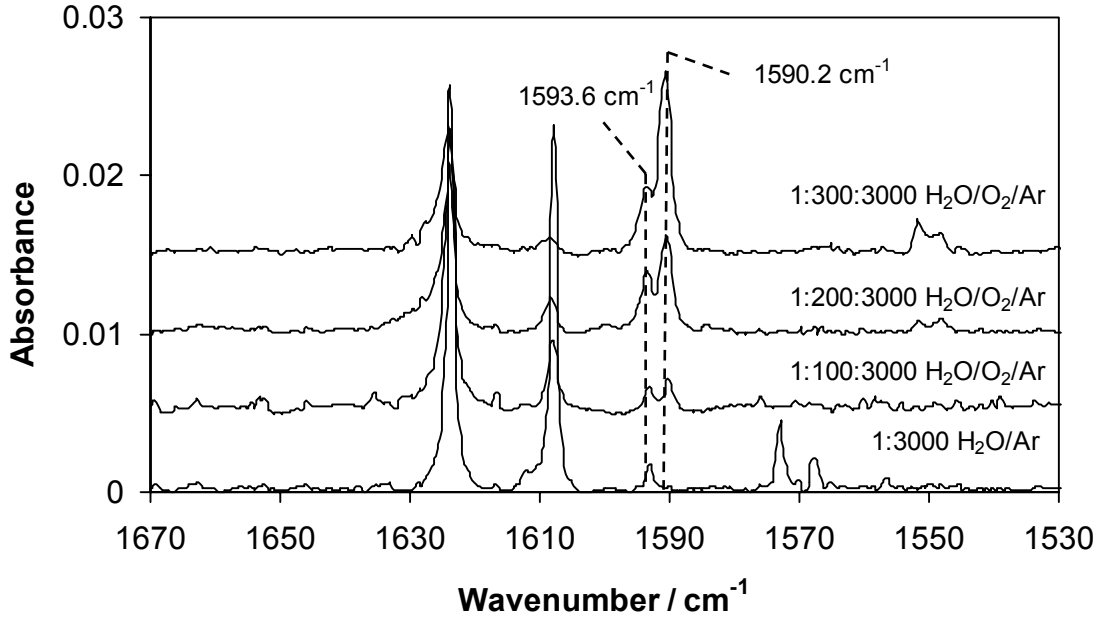

Figure 3.11: *Infrared spectra of 1:X:3000 $H_2O/O_2/Ar$ matrices at 11 K in the HOH bending region of the IR.*

3.1.7 Assignment of the ν_4 Vibration of $H_2O{\cdot}O_2$

Lastly, calculations predict that the forbidden stretching vibration (ν_4) of O_2 becomes slightly active in $H_2O{\cdot}O_2$ and is red-shifted 5 cm^{-1} from the forbidden free O_2 vibration. The O_2 stretch in molecular oxygen had previously been observed when other molecules acted to lower the symmetry of O_2 (Gerakines et al., 1996). It had also been observed in solid O_2 (Cairns and Pimentel, 1965) but was due to defects in the O_2 lattice (Xie et al., 1997). In each case the O_2 fundamental was observed at ~1551 cm^{-1}. Figure 3.12 shows the growth of an absorption band at 1551.9 cm^{-1} with increasing O_2

concentration. At low water concentrations, the vibration was clearly observed to grow with increasing O_2 concentration, and was a doublet with a second peak at 1548.8 cm^{-1},. At higher water concentrations a third peak at 1550.5 cm^{-1} was present (Figure 3.13). None of these peaks were observed when water was not present indicating the induced vibrations were caused by water.

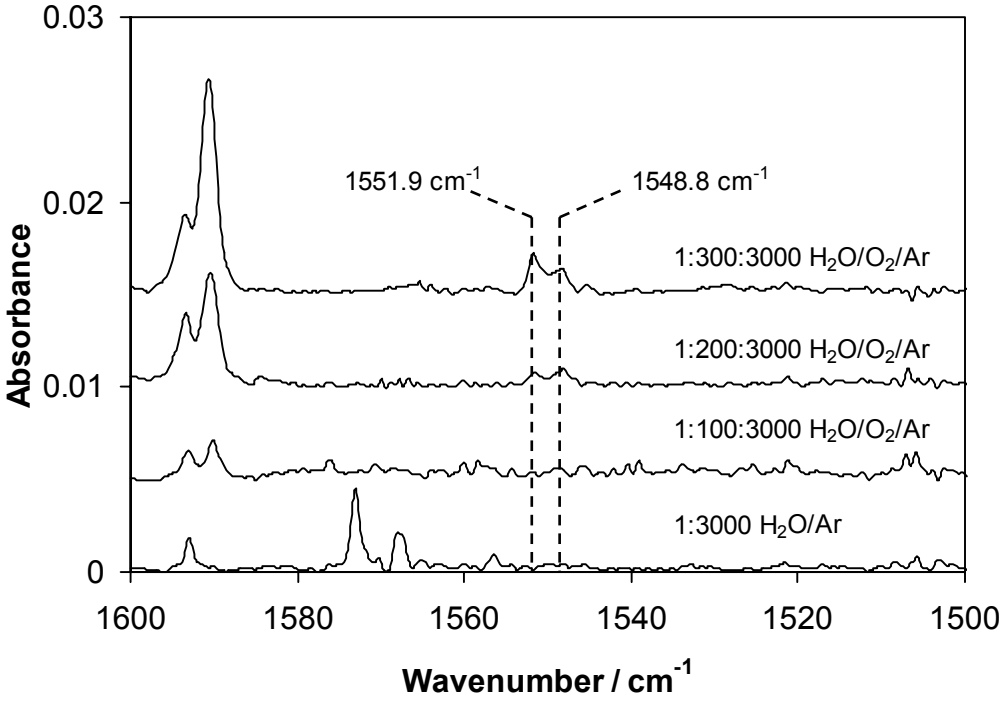

Figure 3.12: *Infrared spectra of 1:X:3000 H_2O/O_2/Ar matrices at 11 K in the OO stretching region of the IR.*

At first it was attractive to assign the higher energy peak to a non-complexed O_2 in a non-homogeneous site and the low energy peak to the $H_2O{\cdot}O_2$ complex. The magnitude and direction of the shift between those two peaks agrees with the calculations. However, a similar doublet was observed by Xie et al. (1997) in glassy Ar/O_2 mixed crystals in which magnetic and quadrupolar moments induced local ordering and caused splitting of the vibration. In addition, they found that the two bands were dependent upon the O_2/Ar ratio. The higher energy band dominated as their

O_2 concentration approached the much lower O_2 concentration used in the present experiments. The lowest O_2/Ar ratio these workers used were ratios of 4.2:10 O_2/Ar whereas the present ratios were typically 0.5-1.5:10 O_2/Ar. Nevertheless, in the present spectra, the high energy band was the most intense in agreement with Xie et al. (1997)

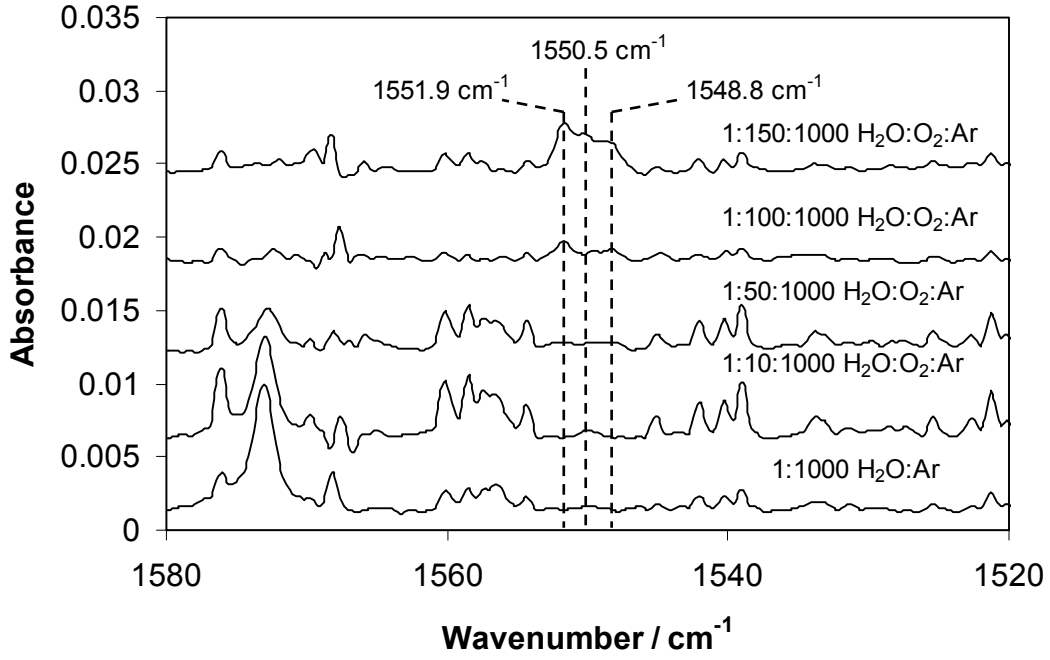

Figure 3.13: *Infrared spectra of 1:X:1000 H_2O/O_2/Ar matrices at 11 K in the OO stretching region of the IR.*

If the bands observed around 1550 cm^{-1} were due to O_2-Ar interactions, then it was likely that the absorptions were from non-complexed O_2 molecules in several non-homogeneous sites and that the 5 cm^{-1} red-shift predicted from theory was too weak to observe. However, in the light of an additional experiment, this may not have been the case. The spectrum of a 1:500 H_2O/O_2 sample, i.e. water in an oxygen matrix, was recorded at 11 K. A similar absorption band structure to that in Ar matrices was observed (Figure 3.14) with three distinct absorption bands. The two higher energy

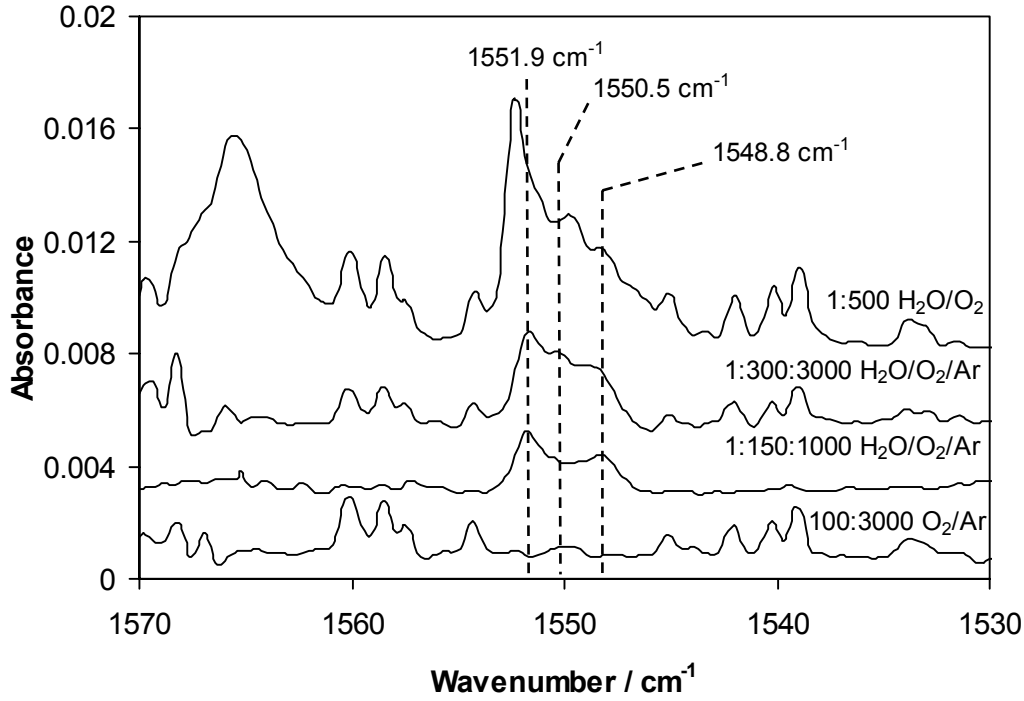

Figure 3.14: *A comparison of the O_2 vibration in H_2O/O_2/Ar matrices and in an H_2O/O_2 matrix.*

bands were slightly displaced compared with the Ar matrix spectra. The absence of Ar means the absorption structure could not be from O_2-Ar interactions. A report of the O_2 vibration from O_2 produced in UV-irradiated H_2O ice (Gerakines et al., 1996) at 1550 cm^{-1} unfortunately only presents one frequency and does not show spectra to make a further comparison, but once again the frequency is in agreement with the present data.

The observed agreement between the frequencies of H_2O/O_2 in Ar matrices, H_2O in O_2 matrices, and O_2 in H_2O matrices, indicated that H_2O must be in very close proximity to O_2 in order to perturb the O_2 vibration. The band structure was not due to magnetic and quadrupolar interactions with Ar but must be due to interactions with a water molecule. There still was the possibility that the structure of the O_2 absorption band was due to nearest neighbour (complexed) and non-nearest neighbour interactions

of O_2 and H_2O. The previously mentioned possible assignment of the lower energy absorption to $H_2O \cdot O_2$ and the higher energy band to non-complexed but perturbed O_2 was still a possibility. There is some evidence for this explanation in Figure 3.14. The non-nearest neighbour O_2 vibrations may have been expected to show a dependence upon the irregular matrix that was activating the vibration. Slight shifts were observed in Figure 3.14 between O_2 and Ar matrices. The lower energy band however did not shift. This would be expected if the source of the vibration were $H_2O \cdot O_2$.

While the relative oscillator strengths of a non-nearest neighbour O_2 vibration and an $H_2O \cdot O_2$ vibration are not known, the relative intensities of the bands could be interpreted to support this assignment. The higher energy absorption band had a greater intensity than the lower energy absorption band which would agree with Figure 3.2 that statistically shows the concentration of non-complexed O_2 should be greater than the concentration of complexed O_2.

The assignment of the ν_4 vibration of $H_2O \cdot O_2$ was much more difficult than the vibrations of the water unit of the complex. It was clear the absorption observed around ~1550 cm^{-1} was the O_2 vibration made infrared active by the symmetry lowering effect of nearby water. However, discrimination between non-complexed and complexed vibrations of O_2 was not definitive. A possible assignment of the absorption structure has been proposed above based upon the experimental and theoretical data. Other experimental techniques such as molecular beam investigations may be useful in making a conclusive decision on this assignment.

3.1.8 Annealing

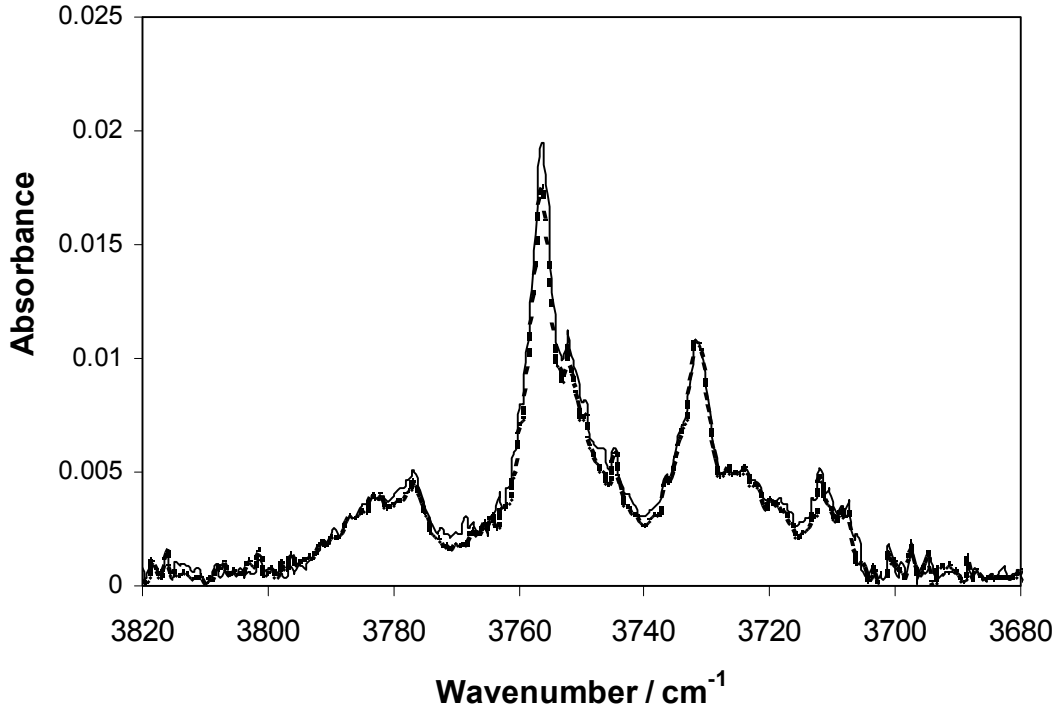

Figure 3.15: *The effect of annealing a 1:100:1000 H_2O/O_2/Ar matrix to 20 K. The bold line represents the absorption spectrum before annealing and the dashed line represents the absorption spectrum after annealing.*

Preliminary annealing experiments were performed in order to ascertain the usefulness of this method to aid in the identification of the $H_2O{\cdot}O_2$ complex.

Annealing a 1:100:1000 H_2O/O_2/Ar matrix at 20 K, did not change the intensity of the absorption bands. Figure 3.15 shows the overlaid spectra in the asymmetric OH stretching region. There was a very slight reduction in water monomer due to dimer formation, but otherwise the spectra are the same. This was also representative of the effect of annealing on the water absorption bands observed in the other regions of the spectrum.

Annealing to 30 K resulted in a decrease of all absorption bands e.g. Figure 3.16. A corresponding increase in water dimer was not observed indicating that some of

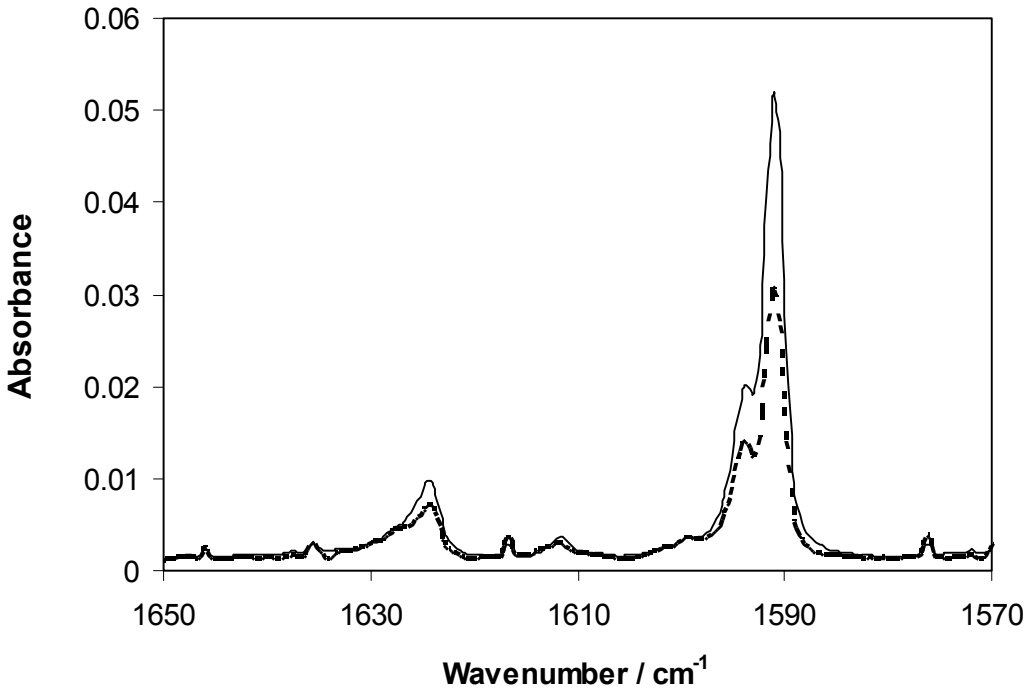

Figure 3.16: *The effect of annealing a 1:150:1000 H_2O/O_2/Ar matrix to 30 K. The bold line represents the absorption spectrum before annealing and the dashed line represents the absorption spectrum after annealing.*

the matrix sublimed during the annealing process. The level of the loss of the matrix was surprising and may indicate some irregularity with the heating or temperature measuring devices in the equipment. Nevertheless, the results obtained from these preliminary experiments did not appear to be very useful in providing any further evidence for the identification of the $H_2O{\cdot}O_2$ complex.

3.1.9 Isotopic Substitution

Experiments were performed by replacing D_2O by H_2O. A sample spectrum of the DOD bending region is shown in Figure 3.17 and as expected is similar to the corresponding spectrum of the HOH bending region. The spectra obtained for D_2O/O_2/Ar matrices showed the absorption bands assigned to vibrations of the $H_2O{\cdot}O_2$ complex shift to lower frequencies, however, the magnitude of the shifts did not provide further clear evidence for the assignment. This was because the size of the

shifts for the $H_2O{\cdot}O_2$ complex are very similar to that of H_2O monomer. Thus, the two species can not be distinguished by different shifts upon isotopic substitution.

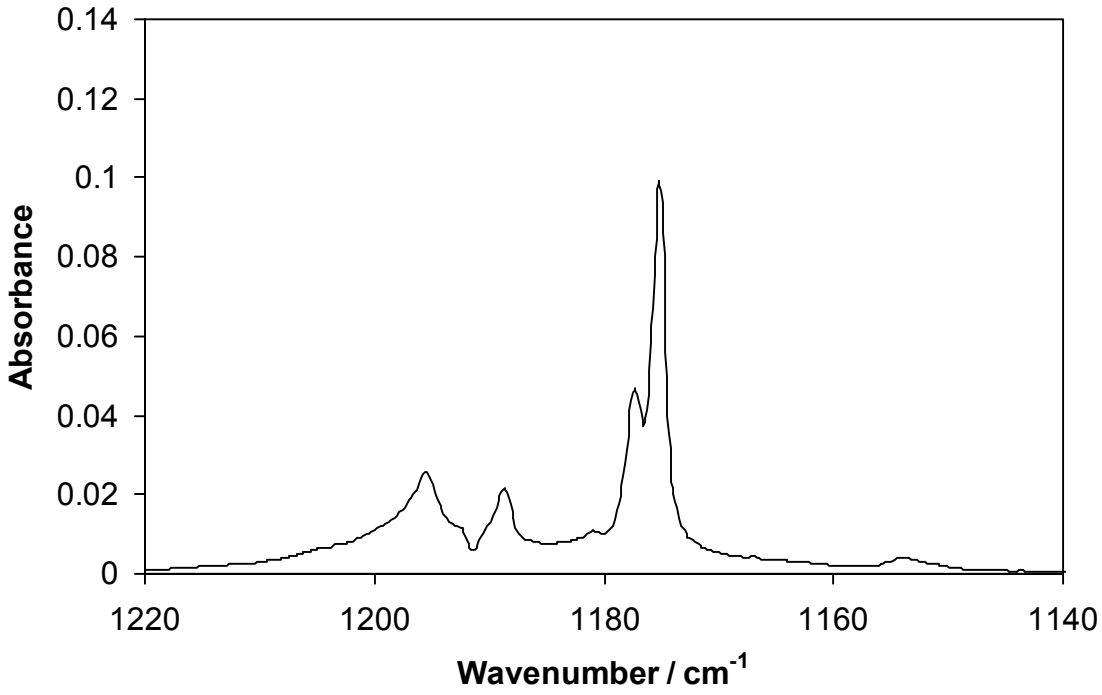

Figure 3.17: *Infrared spectrum of a 3:100:1000 $D_2O/O_2/Ar$ matrix at 11 K in the DOD bending region of the IR.*

3.1.10 Conclusions – Re: The $H_2O{\cdot}O_2$ Complex

The ν_3 (asymmetric OH stretch), ν_1 (symmetric OH stretch), and ν_2(HOH bending) vibrational modes of an $H_2O{\cdot}O_2$ complex (Table 4.2) have been spectroscopically identified in $H_2O/O_2/Ar$ matrices at 11 K. These assignments were deduced by observing specific absorption bands in the IR that increased in intensity with increasing O_2 concentration (at a fixed H_2O concentration). Care was taken to avoid incorrectly assigning absorption bands from non-rotating water monomer, which should also have shown the same intensity behaviour. As shown in Table 4.2 the experimentally determined vibrational energies agreed well with theoretically calculated values.

Table 3.3: *A comparison of the calculated and experimentally determined vibrational energies of H_2O and $H_2O{\cdot}O_2$*

	Calculated H_2O	Calculated $H_2O{\cdot}O_2$	Experimental H_2O	Experimental $H_2O{\cdot}O_2$
Mode	Energy / cm^{-1}	Energy / cm^{-1}	Energy / cm^{-1}	Energy / cm^{-1}
ν_4		1551		1551
ν_2	1596	1593	1590	1590
ν_1	3658	3661	3638	3640
ν_3	3755	3753	3736	3731

The ν_4 (OO stretch) vibration has been much harder to assign. Discriminating between O_2 vibrations induced by non-complexed but symmetry-lowered O_2 and the O_2 vibration of $H_2O{\cdot}O_2$ was not easy. A possible assignment, based upon the experimental and calculated data was tentatively made. It was clear that small amounts of H_2O in the matrix can make the O_2 vibration slightly active, but for a definitive assignment for the ν_4 mode of $H_2O{\cdot}O_2$, different experimental techniques would need to be employed.

3.2 The H_2O·HO Complex

3.2.1 Summary of Calculations of Kjaergaard and Schofield

The research group of Henrik Kjaergaard at the University of Otago collaborates with the research group of Dr. Quickenden and performed all the calculations discussed in the following chapter. While these calculations to *do not* constitute work carried out by the author of this thesis, a brief summary of their work follows as the results of their calculations are very important to this thesis.

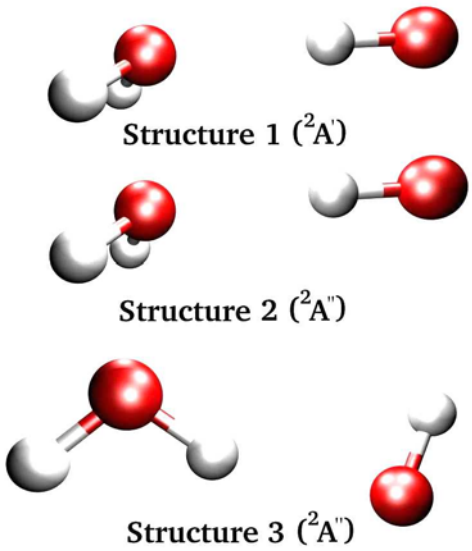

Figure 4.1: *QCISD/6-311++G(2d,2p) optimised structures for the H_2O·HO complex.*

Structures **1-3** (Figure 4.1) were found to be minima for H_2O·HO. This was confirmed by the lack of imaginary frequencies arising in the frequency calculations.

The geometries were optimised with the quadratic configuration interaction including single and double excitations (QCISD) method with the 6-311++G(2d,2p) basis set in Gaussian98.

***Table 4.1**: Calculated binding energies of $H_2O \cdot HO$*

	Structure 1 ($^2A'$)	Structure 1 ($^2A''$)	Structure 1 ($^2A''$)
ΔE / kcal/mol	5.69	5.37	3.51

***Table 4.2:** Calculated vibrational frequencies in cm^{-1} and intensities in km mol^{-1} (in parenthesis) for $H_2O \cdot HO$ structures*

Vibration	Structure 1 ($^2A'$)	Structure 2 ($^2A''$)	Structure 3 ($^2A''$)	Free OH / H_2O
ν_1	165.6 (122)	168.4 (22.5)	87.0 (187.3)	
ν_2	174.4 (1.07)	186.5 (0.0005)	105.9 (219.6)	
ν_3	184.4 (64.6)	199.3 (174.2)	161.0 (73.6)	
ν_4	427.0 (197)	525.0 (170.2)	310.6 (178.8)	
ν_5	621.2 (149)	526.2 (167.3)	369.9 (4.1)	
ν_6	1685.1 (70.3)	1688.9 (69.5)	1697.2 (51.4)	1686.5 (65.6)
ν_7	3697.3 (250)	3694.3 (235.5)	3758.2 (23.7)	3769.7 (12.0)
ν_8	3877.3 (13.8)	3875.1 (13.8)	3853.3 (94.1)	3879.8 (56.1)
ν_9	3978.6 (82.3)	3974.4 (79.1)	3967.3 (116.0)	3982.0 (56.1)

Structure **1** and **2** are very similar, but belong to different electronic states, $^2A'$ and $^2A''$ respectively. Table 4.1 shows that the energy difference between the two structures is small.

Table 4.2 shows the vibrational frequencies and intensities calculated for structures **1-3**. These data can be compared directly with the calculations of other workers, summarised in Table 1.1. It should be noted that the intensity of the ν_7 transition, for both structures **1** and **2,** is greatly enhanced compared with the intensity of free OH. The amounts of complex in the matrices in this work are very small. The observation of the hydroxyl OH stretch of the complex is only made possible by this enhancement in the intensity of the vibration compared with free OH.

The ν_7 vibrational frequency for Structure **1** was then refined using an anharmonic local mode model. Calculations that allow for the anharmonicity of the vibration produce highly accurate results (Low and Kjaergaard, 1999). Details about the anharmonic oscillator model calculations, and further discussions about the implications of all the calculations, can be found in subsequent sections.

3.2.2 Vibrations of the H_2O Unit of $H_2O{\cdot}HO$

Langford (1999) found no absorptions in the regions of the fundamental vibrations of H_2O that could be assigned to $H_2O{\cdot}HO$. The present study similarly did not find any of these vibrations. The theoretical calculations (Table 4.2) predict shifts of between 1 and 4 cm^{-1}. After the experiments for this part of this thesis were completed, Engdahl et al. (2003) reported the observation of the vibrations of the H_2O unit of $H_2O{\cdot}HO$ in Ar matrices. Interestingly, they observed that the vibration was split into a

number of rovibrational bands ie. the H_2O unit of the complex rotates. These workers formed their complexes by the reaction of H_2 and HO_2 in an Ar matrix irradiated by UV laser light. Small amounts of H_2O were also formed under these conditions, but the amounts were very small which enabled the observation of the H_2O bands of $H_2O{\cdot}HO$. In the present work, the concentration of H_2O monomer was very much higher than the concentration of complex. Thus the large absorption from this excess of H_2O monomer in the matrix was the most likely reason why the H_2O vibrations of $H_2O{\cdot}HO$ were not observed.

3.2.3 Far-Infrared Absorptions

The principal motivation of investigating $H_2O{\cdot}HO$ in this thesis was to reconfirm and extend the assignments Langford et al. (2000a) had previously made. The theoretical calculations (Table 4.2) predict that some intense far-IR vibrations could be used to further characterise the complex. The ν_4 and ν_5 vibrations in particular are quite different for Structures **1** and **2** whereas the ν_7 vibrations are similar in frequency. Identification of these bands would help determine the structure of the complex in the Ar matrix. Langford (2000a) only had access to sapphire optical windows that prevented measurements down to 500 cm^{-1} (the low wavenumber limit of the Mattson spectrometer) and any possible investigation of these bands. For Structure **1** the ν_4 mode is the OH bending in the C_s plane while the ν_5 mode bends out of the C_s plane. For Structure **2**, these vibrations are reversed with the ν_4 mode being the OH bending out of the C_s plane and the ν_5 mode being the OH bending in the C_s plane.

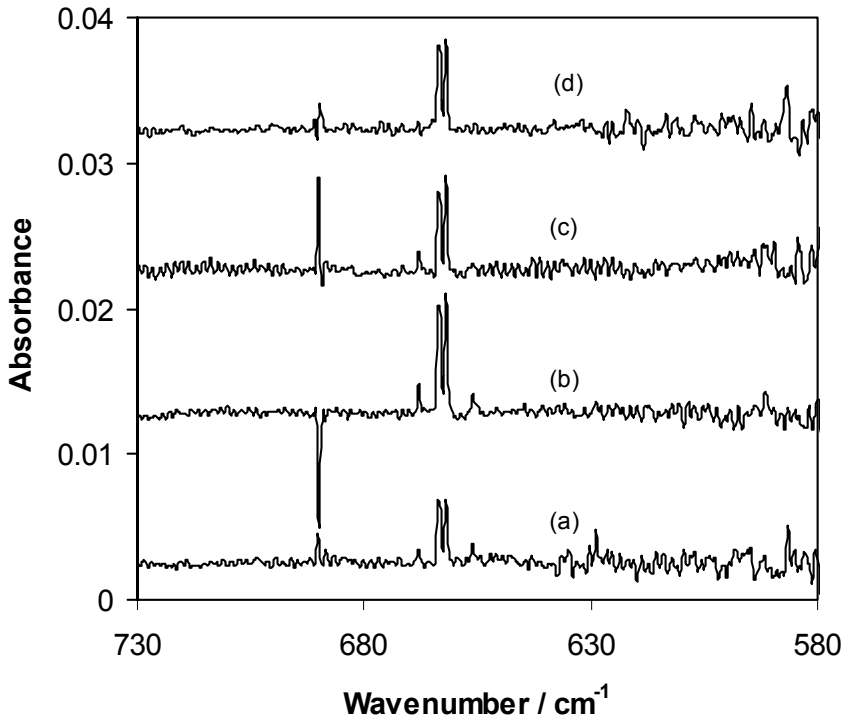

Figure 4.2: *Infrared spectra of a solid H_2O/Ar matrix at 11 K for H_2O/Ar ratios of (a) 1:100, (b) 1:150, (c) 1:250, and (d) 1:500. The variable peak at ~690 cm^{-1} is an artifact produced by the spectrometer as described in Chapter 2.*

With the addition of KBr windows, the mid-IR region from 4000 to 500 cm^{-1} became accessible. H_2O/Ar gaseous mixtures in ratios of 1:100 to 1:500 were passed through the radio-frequency discharge before deposition. As is shown in Figure 4.2, an absorption feature was observed as a doublet of peaks at 661.9 and 663.5 cm^{-1}. In blank experiments without a discharge, the absorption feature was absent.

The absorption bands have substantially higher frequencies than predicted by calculations. If these bands originated from $H_2O{\cdot}HO$, concentration dependence studies, like those performed by Langford et al. (2000a), the intensity of these bands (scaled to the free OH intensity) should have shown a dependence on the initial water concentration. However, no such concentration dependence was found.

Figure 4.3 shows a comparison between the data of Langford et al. (2000a) for the O-H vibration and the 661.9/663.5 cm^{-1} doublet bands. The 661.9/663.5 cm^{-1} bands clearly do not show the same concentration dependence. In fact there does not appear to be any trend. This evidence casts a doubt on the assignment of these bands to $H_2O{\cdot}HO$. Nevertheless, the species causing this absorption was only present when a discharge and water were present in the gaseous precursor mixture.

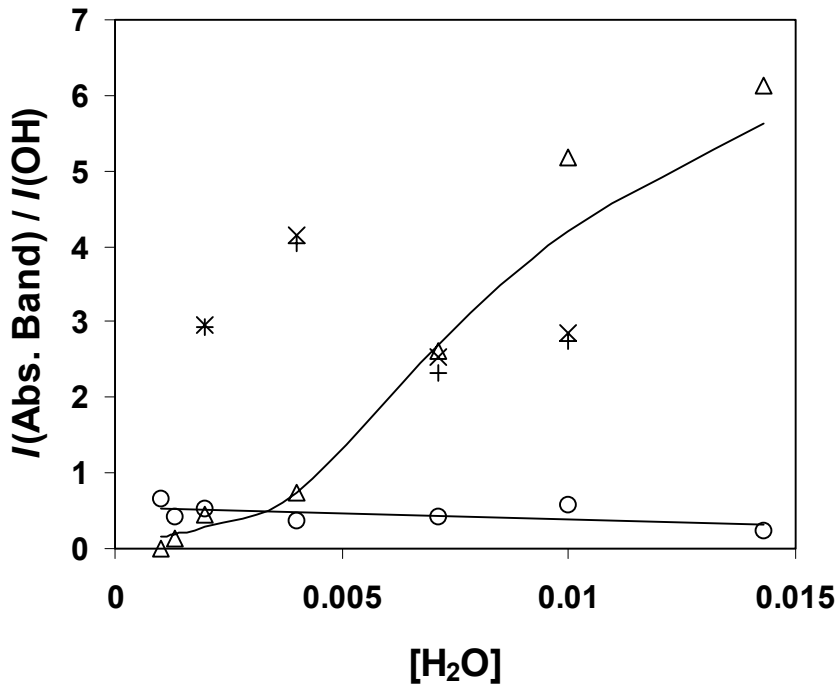

Figure 4.3: *A comparison of the scaled intensities of the 661.9(×) and 663.5(+) cm^{-1} bands with the scaled intensities of the 3452(Δ) and 3428(o) cm^{-1} bands of $H_2O{\cdot}HO$ (Langford et al., 2000a) as a function of the water fraction in an Ar matrix.*

In the present work, when H_2O was replaced by D_2O in an otherwise identical experiment the doublet absorption feature remained unchanged. Clearly, the species causing this absorption was not $H_2O{\cdot}HO$, but was some impurity reacting with water in the discharge. The possibility of a silicon-based molecule was looked into as the

discharge might possibly have been vaporising material from the glass into the H_2O/Ar gas stream. However, nothing in the literature suggested that this was the case.

Finally, it was found that matrix-isolated CO_2 was the cause of the absorption bands. Traces of pump oil must have been reacting with O atoms produced in the discharge to produce CO_2. An alumina filter was consequently installed into the system to prevent interference by these trace impurities.

However, with the absorption bands assigned to CO_2, all possible candidates for intermolecular $H_2O{\cdot}HO$ vibrations were gone. The practical lower wavenumber limit of the Mattson infrared spectrometer was ~580 cm^{-1}. Below this value, low signal-to-noise became a problem. The calculations by our colleagues at the University of Otago predicted that the intensity of the v_4 vibration of $H_2O{\cdot}HO$ was comparable to v_7 and so it should be observed. However, similar vibrations of the $H_2O{\cdot}HCl$ complex have not been observed, despite mid-infrared spectra showing high concentrations of the complex (Engdahl and Nelander, 1996) It was suggested that these bands are very broad and this may be the reason why these vibrations of $H_2O{\cdot}HO$ were not observed here. Alternatively, the vibrations may have frequencies less than ~580 cm^{-1}.

3.2.4 O-H Vibration of the Hydroxyl Radical in $H_2O{\cdot}HO$

Langford et al. (2000a) had observed three bands in the 3460-3420 cm^{-1} spectral region that were present only when the H_2O/Ar precursor gas stream was passed through a Tesla coil discharge prior to deposition. Two of these bands, at 3452.2 and 3428.0 cm^{-1}, were assigned to $H_2O{\cdot}HO$. The third band at 3442.1 cm^{-1} was left unassigned as it had not been previously observed by earlier investigations (Acquista et

al., 1968; Suzer and Andrews, 1988; Cheng et al., 1988). Langford et al. (2000a) reported no concentration dependence of the 3442.1 cm^{-1} band and no isotopic substitution experiments were performed to try and determine the origins of it.

In the present work, the experiments of Langford et al. (2000a) were repeated and extended in order to assign the 3442.1 cm^{-1} band. Figure 4.4 shows the spectra of H_2O/Ar matrices formed by passing an H_2O/Ar gas mixture through an electrical discharge prior to deposition. The hydroperoxy radical was observed as a doublet at ~3410 cm^{-1}, however no evidence of $H_2O{\cdot}HO_2$ was present (Nelander, 1997). Nevertheless, the free OH radical was observed at 3549 cm^{-1} and $H_2O{\cdot}HO$ could be seen at 3452.2 and 3428.0 cm^{-1}. In addition, the unassigned 3442.1 cm^{-1} band was also observed.

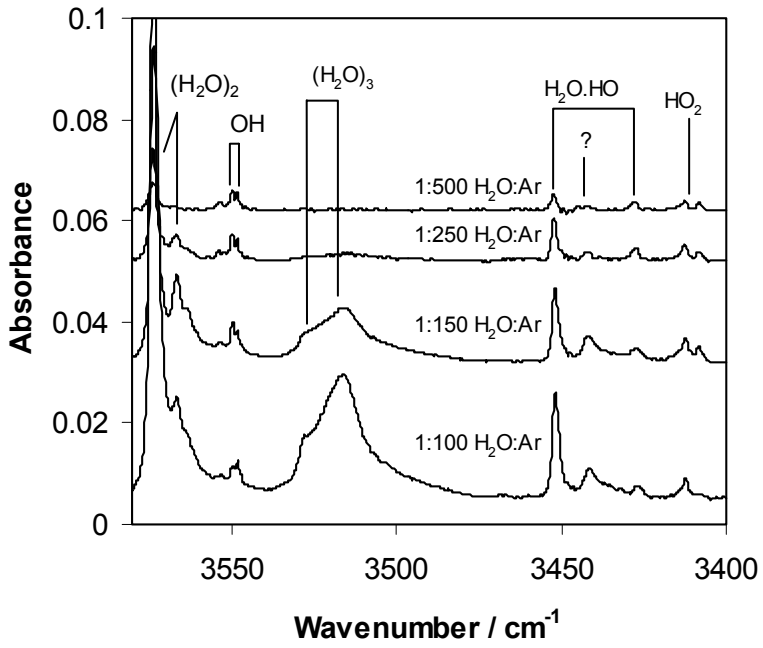

Figure 4.4: *The dependence of the absorption bands produced when H_2O/Ar gas mixtures are electrically discharged and deposited at 11.0 K upon [H_2O].*

The intensity of the unassigned 3442.1 cm^{-1} band in the 3460-3420 cm^{-1} region was scaled to the intensity of the free OH radical. This scaling was important because changes in the efficiency in the production of OH radicals by the discharge across a wide range of initial water concentrations are not known. The free OH radical absorbance thus acted in a similar way to an internal standard. Regardless of any changes in efficiency of the discharge process, the higher the water concentration, the higher the $H_2O{\cdot}HO$ concentration relative to the concentration of free OH. Figure 4.5 shows the scaled intensities of the 3452.2 and 3428.0 cm^{-1} bands obtained by Langford et al. (2000a). That is, the 3452.2 cm^{-1} band exhibits a strong dependence on the initial water concentration. The 3428.0 cm^{-1} band does not show such a dependence.

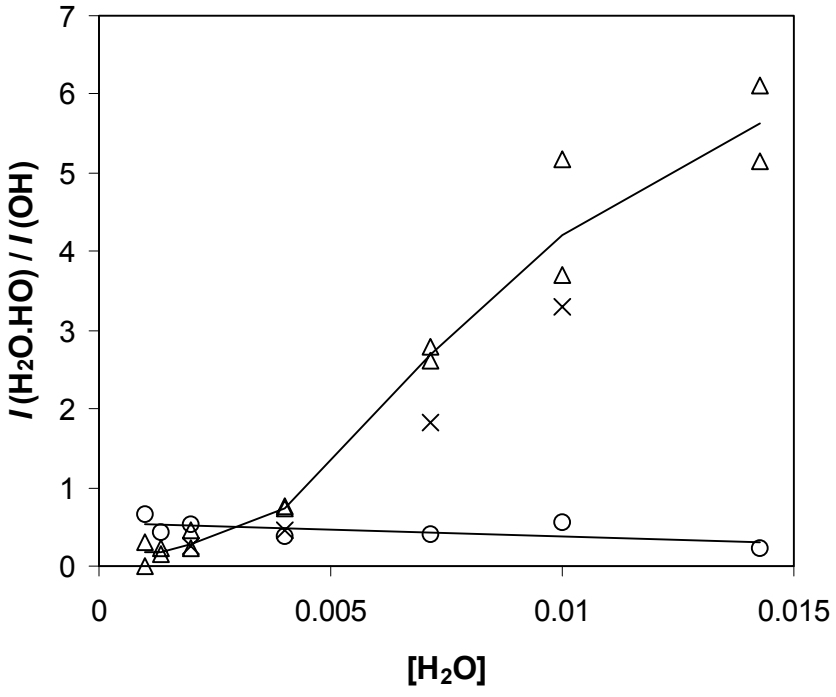

Figure 4.5: *A comparison of the scaled intensity of the 3442 cm^{-1} (×) band with the scaled intensity of the 3452(Δ) and 3428(o) cm^{-1} bands of $H_2O{\cdot}HO$ bands (Langford et al. 2000a) as a function of the water fraction in an Ar matrix.*

Langford et al (2000a) reasoned that this absorption band must be from a site that is unfavourable at high water concentrations. The present experiments do not disagree with this conclusion.

The 3442.1 cm^{-1} band (Figure 4.5) however showed a concentration dependence similar to that of the 3452.2 cm^{-1} band. This suggested that the absorption band was most likely to arise from $H_2O{\cdot}HO$ as it occurred in the same region as the previously assigned $H_2O{\cdot}HO$ vibrations. However, it could also have been some other species produced in the discharge. Isotopic substitution (see Section 4.5) was used to show it indeed was a vibration of $H_2O{\cdot}HO$.

3.2.5 Isotopic Substitution

D_2O was substituted for H_2O in an otherwise identical experiment. Figure 4.6 shows the corresponding region of Figure 4.4 for discharged D_2O/Ar matrices. It was unfortunate that the free OD radical absorption was not observed in this spectrum. The slightly different shifts of vibrational energy of the D_2O dimer and OD radical, resulted in the much more intense D_2O absorption dominating the spectral region where the OD radical stretching vibration should be found. The OH radical vibration at 3549 cm^{-1} shifts to 2616 cm^{-1} (Cheng et al., 1988) and in the present work was totally obscured by D_2O dimer.

A similar concentration dependence investigation (as described in Section 4.4) for D_2O/Ar was made impossible by this masking of the free OD radical band because the process of scaling the $D_2O{\cdot}DO$ complex absorption band intensities to free OD intensities could not be carried out.

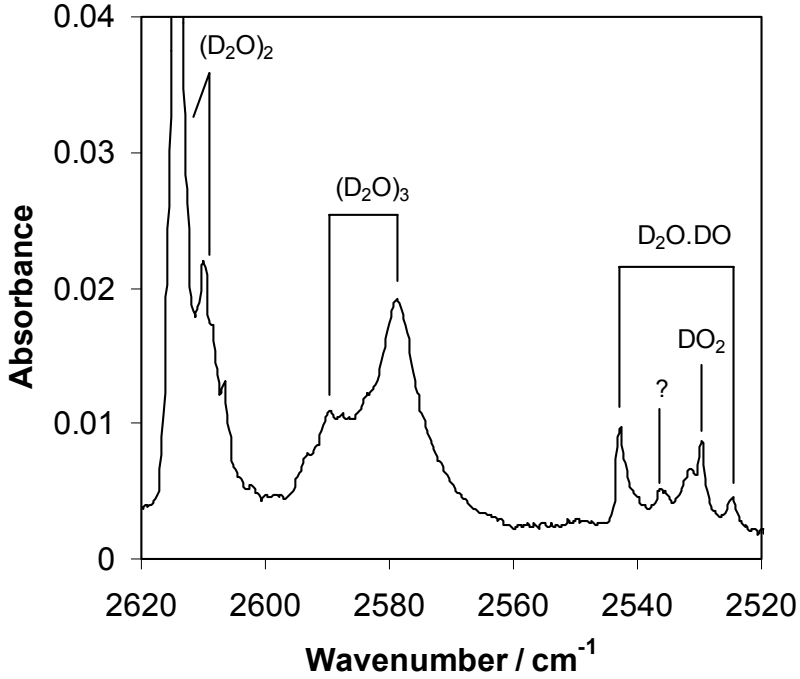

Figure 4.6: *Infrared spectrum of the OD/Ar region of a 1:100 D_2O/Ar matrix at 11.0 K.*

Nevertheless, there was still enough evidence from this data to conclusively prove the original $H_2O{\cdot}HO$ assignments. The corresponding three absorption bands observed for $H_2O{\cdot}HO$ can be seen for the deuterated analog in Figure 4.6 at 2542.9, 2536.4 and 2524.6 cm^{-1}. Importantly, the unassigned middle peak of the set was observed indicating that this absorption must also be assigned to the $H_2O{\cdot}HO$ complex. Interestingly, the DO_2 absorption band shifted in between the two lower energy $D_2O{\cdot}DO$ bands.

The high-level calculations provided by our colleagues at the University of Otago provided compelling evidence for these assignments. Table 4.3 shows the comparison of the theoretical and experimentally determined vibrational energies for

$H_2O{\cdot}HO$ and $D_2O{\cdot}DO$. These calculated values of the OH-stretching vibration were obtained using an anharmonic oscillator local mode model with a Morse potential fit to the QCISD/6-311++G(2d,2p) calculated 15 point grid (-0.3 Å to 0.4 Å) about the equilibrium OH bond length. The calculations estimated the amount of anharmonicity of the OH bond to better predict its vibrational frequency. Previous calculations (Kim et al., 1991; Xie and Schaefer, 1993.), and the calculations shown in Table 4.2, did not consider anharmonicity. The unscaled values in Table 4.3 were the initial values obtained from the anharmonic oscillator model. These data were then scaled (ω by 0.9719 and ωx by 0.8154) by using experimental values of ω and ωx (that are a measure the anharmonicity of the bond) to further refine the calculated value. Experimental values of ω and ωx for $H_2O{\cdot}HO$ do not exist, so values for OH were used as an approximation. These values were found from a Birge-Sponer fit to the $\Delta\nu_{OH}$=1-6 from the HITRAN 2000 database.

Table 4.3: *Comparison of calculated and measured frequencies and isotopic shifts (cm^{-1}) of the hydroxyl OH-stretching band in $H_2O{\cdot}HO$ Structure **1** ($^2A'$).*

	Experimental			**Calculated[a]**	
	Site 1	Site 2	Site 3	Unscaled	Scaled[b]
ν_{OH}	3452.2	3428.0	3442.1	3546.1	3479.0
ν_{OD}	2542.9	2524.6	2536.7	2643.6	2586.8
Isotopic shift	909.3	903.4	905.7	902.5	892.2
% difference				0.75, 0.10, 0.35	1.88, 1.24, 1.5

[a] Anharmonic oscillator local mode model.[b] Scaled using experimental values of ω and ωx. For more details read main text.

The scaled theoretical frequencies were in excellent agreement with those determined from experiment, especially if matrix shifts were considered, and were by far the most accurate calculation of the vibration in the literature. The theoretical and experimental isotopic shifts were also in excellent agreement - differing by only around 1%. This combination of theoretical and experimental evidence led to the conclusion that the bands shown in Figure 4.4 and 4.6 were vibrations of $H_2O{\cdot}HO/D_2O{\cdot}DO$.

3.2.6 The Intensities of the OH (OD) Vibration

While comparisons of vibrational frequency shifts following isotopic substitution are standard practice in infrared spectroscopy, the comparison of intensities

Table 4.4: *A comparison of experimentally measured intensity of vibrational frequencies of $H_2O{\cdot}HO$ and $D_2O{\cdot}DO$*

	Site 1 Intensity / arb. units		**Site 2 Intensity / arb. units**		**Site 3 Intensity / arb. units**	
	$H_2O{\cdot}HO$	$D_2O{\cdot}DO$	$H_2O{\cdot}HO$	$D_2O{\cdot}DO$	$H_2O{\cdot}HO$	$D_2O{\cdot}DO$
	10.6	6.35	3.26	1.77	6.39	1.91
	10.9	7.30	2.20	1.38	4.38	1.74
	12.3	6.74	2.22	1.64	6.97	1.37
	9.82	6.69	2.70	1.00	5.60	2.5
Mean	10.9	6.77	2.60	1.45	5.84	1.87
Std Err in Mean	0.53	0.19	0.24	0.17	0.56	0.68
95% CI	1.69	0.31	0.79	0.54	1.73	1.46

is much rarer. This is mainly because theoretical calculations of vibrational intensity are not highly accurate. The Otago Group however has had recent success in accurately calculating vibrational intensities for the H_2O dimer (Low and Kjaergaard, 1999). Their calculations predicted that the vibration of the OH radical of $H_2O{\cdot}HO$ should decrease by a factor of 0.51 of its original value upon deuteration. This is a large decrease and can easily be tested against the experimental data (Table 4.4) from the present study.

Data from discharged 1:100 H_2O/Ar (D_2O/Ar) matrices were used for this comparison. Four replicates, from a new matrix, were made for each isotope to reduce the effect of random error. The latter arose from small changes in experimental conditions (e.g. slightly different flow rates) and minor variations in the integrating technique caused variations in the data. The software used to perform the integrations had an in-built element of subjectivity arising from through the manual setting of limits of integration and baselines. In addition, problems of slightly overlapping bands and the broadening of small bands near the baseline contributed to the variations in the data.

Table 4.5: *A comparison of the band intensity ratios of the hydroxyl radical OH-stretching band of $H_2O{\cdot}HO$ and its deuterated isotopomer.*

Calculated[a] OD/OH Ratio	Site 1 OD/OH Ratio	Site 2 OD/OH Ratio	Site 3 OD/OH Ratio
0.51	0.62 ± 0.10[b]	0.56 ± 0.27[b]	0.33 ± 0.27[b]

[a] *Anharmonic oscillator local mode calculation.* [b] *Errors estimated at the 95% confidence level*

Despite such sources of error, Table 4.5 shows that the calculated and experimentally determined intensities agree quite well and provide further evidence for the assignment of these bands to $H_2O{\cdot}HO/D_2O{\cdot}DO$.

3.2.7 Band Intensity Comparisons for Free OH and Complex OH

Anharmonic local mode calculations on free OH predict a value of 7 km mol^{-1} for the intensity of the O-H stretching vibrational transition, and a value of 250 km mol^{-1} for the corresponding vibration of the complex. As mentioned previously, this enhancement made the observation of the complex possible, despite its low concentration.

While the actual amounts of OH and $H_2O{\cdot}HO$ in the matrix were unknown, the relative amounts of each were estimated using the statistical method described in 3.1.2 and then compared with experiment. In summary, it was assumed that the kinetic energies of the gaseous OH and H_2O molecules were too high for the formation of the $H_2O{\cdot}HO$ complex prior to deposition. The model also assumed that H_2O, OH and Ar were all the same size and the same interaction forces between each other. Under these constraints, OH and H_2O molecules should deposit randomly on the cold. The probability, *P*, of randomly depositing H_2O next to an OH radical can then be calculated from the following equation:

$$P = {}^{12}\mathrm{C}_n \left(P_{Water}\right)^n \left(P_{Ar}\right)^{12-n} \quad (1)$$

where n is the number of nearest neighbour H_2O molecules, P_{Water} is the fractional amount of H_2O in the matrix, P_{Ar} is the fractional amount of Ar in the matrix, and ${}^{12}C_n = 12!/n!(12-n)!$ and is the number of combinations in which n H_2O atoms can be arranged around a single OH radical in an argon lattice. P_{Water} and P_{Ar} are simply calculated from the ratios of the gaseous mixtures from which the matrices are deposited.

Using this approach it was found that in a matrix formed from a 1:150 H_2O/Ar mixture, ~7.4 percent of the OH radicals would theoretically have a nearest neighbour water molecule. In other words, the molar concentration of H_2O·HO should be around 7.4% of the molar concentration of free OH. The theoretically determined intensity ratio of the IR intensities of the isolated OH stretch to the OH stretch in the complex was (7 km mol^{-1})/ (250 km mol^{-1}) = 0.028. The experimentally determined intensity ratio was 0.032 ± 0.007 after correction for the 7.4 percent nearest neighbour percentage from above. This excellent agreement provides further evidence for the assignment of the H_2O·HO.

3.2.8 Conclusions – Re: The H_2O·HO Complex

The comparison of calculated and experimental changes in vibrational frequency and intensity were made to assign absorption bands at 3452, 3442 and 3428 cm^{-1} to the O-H stretching vibration of the hydroxyl unit of H_2O·HO and the corresponding vibrations of the deuterated isotopomer. The evidence for the assignments includes:

1) Agreement between the calculated vibrational frequencies of H_2O·HO and those measured experimentally.

2) Agreement between the calculated and measured isotopic frequency shifts of the OH-stretching vibration going from $H_2O{\cdot}HO$ to $D_2O{\cdot}DO$.

3) Agreement between the calculated and measured intensity decrease of the OH-stretching vibration of $H_2O{\cdot}HO$ when going to the corresponding O-D stretch of $D_2O{\cdot}DO$.

4) Agreement between the calculated and experimentally determined intensity enhancements of OH-stretching vibration in $H_2O{\cdot}HO$ compared with that in free OH.

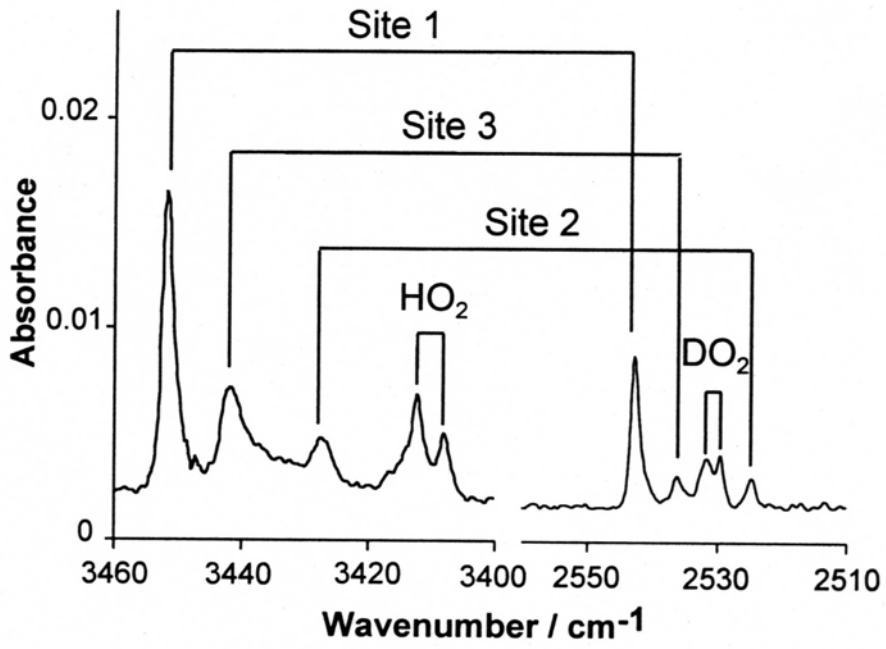

Figure 4.7: *Assignment of the absorption bands of $H_2O{\cdot}HO$ and $D_2O{\cdot}DO$ in the OH/OD stretch infrared region.*

Unfortunately none of the far-infrared absorption bands were identifiable. Structure **1** has the singly occupied molecular orbital perpendicular to the C_s symmetry plane, while Structure **2** has this molecular orbital in the symmetry plane. The ν_4 and ν_5 modes of structures **1** and **2** involve the motion of the hydroxyl hydrogen in and out of this C_s plane. This results in the vibrational frequencies of these transitions being different for the two structures. The measurement of these two modes of vibration would be very useful in identifying the structure of the complex in the matrix.

Determination of the structure of the complex from the present data cannot be made because the theoretically predicted difference in the ν_7 vibration was only small. The interpretation of the three absorption bands was the same as that proposed by Langford et al. (2000a). That is, the bands were assigned to the $H_2O{\cdot}HO$ complex occupying three sites in the Ar matrix (Figure 4.7). Structure **1** of Figure 4.1 is the lowest energy configuration and is the likely structure. It is unlikely that the multiple bands were caused by the other structures of $H_2O{\cdot}HO$ complex as the OH vibrational frequency of Structure **2** is too similar to that of Structure **1** (Table 4.2). The possibility of the multiple bands being the vibrations of Structure **3** was also discarded because the predicted OH vibration of Structure **3** lies within 11 cm^{-1} of the free OH vibration and not around the 100-130 cm^{-1} value observed experimentally.

3.3 A New Mechanism for O_2 Formation in Cosmic Ices

3.3.1 Introduction

As pointed out in Chapter 1, the reason for the interest in O_2 molecules beyond our planet is that it has an important role in most life processes on Earth. Perhaps it will therefore be a prerequisite for life processes beyond Earth. Chapter 1 also highlights some of the difficulties involved in spectroscopically observing the O_2 formed on the icy surfaces of outer solar system bodies. The observation of two absorption bands from apparently solid O_2 at Ganymede by Spencer et al. (1995) indicates that significant quantities of solid O_2 must exist trapped on or near its icy surface. The observation is remarkable, not insofar as O_2 is formed in irradiated ice as this has long been known (Reimann et al. 1984), but is remarkable because the surface temperature of Ganymede is much higher than the sublimation temperature of O_2 (Orton et al., 1996)

The above observations highlight many things that the scientific community does not entirely understand about this area of research. The two principal issues being:

(i) What are the chemical processes that form O_2 in ice?

and,

(ii) How does O_2 remain trapped in ice above its sublimation point?

Some 10 years after the original observations of O_2 in ice on Ganymede were made, these issues have still not been fully resolved.

Europa and Titan currently represent the best two places in our Solar System to find biological life outside of our own biosphere. The Galileo probe found Europa's

surface to be ice-rich and observations by Spencer and Calvin (2002) have shown the presence of O_2 on Europa. At the time of writing this thesis the Cassini-Huygens mission to Saturn has just entered orbit around the ringed-planet but data about its icy satellites has not been collected. Nevertheless, it would appear that where there is ice in the Solar System, there is a good chance that O_2 will also be present and probably produced by radiation.

The mechanism that is proposed to account for the two questions asked above arises from two different, but overlapping pieces of experimental evidence that have been reported in the literature. Firstly, experiments show that H_2O_2 dimers produce O_2 molecules when photolysed (Engdahl and Nelander, 2002). This piece of evidence answers question (i). Secondly, H_2O_2 molecules form aggregates in ice that enables O_2 (formed by the above process) to remain trapped. This evidence answers question (ii). The mechanism proposed is not a reinterpretation of these workers conclusions, but is in itself a new contribution that draws upon multiple sources of evidence to create this mechanism.

3.3.2 Formation and Decomposition of Hydrogen Peroxide

Radiolytic or photolytic destruction of water molecules in irradiated ice is a source of hydroxyl radicals:

(10)

These can react to give hydrogen peroxide:

$$OH + OH \rightarrow H_2O_2 \qquad (11)$$

and then the hydroperoxy radical:

$$H_2O_2 + OH \rightarrow H_2O + HO_2 \qquad (12)$$

The OH, H_2O_2 and HO_2 formed in UV irradiated ice by the above reactions have all been detected in laboratory studies via their infrared absorptions (Gerakines et al., 1996). The H_2O_2, presumably formed via this reaction pathway, has also been identified in the icy surface of Europa (Carlson et al., 1999b).

The photolysis of gas phase H_2O_2 does *not* yield O or O_2 (Vaghjiani et al., 1992), instead the primary products are OH radicals (and H atoms at higher energy). In addition, a summary of the data on the radiolysis and photolysis of ice (Johnson et al., 2003) indicates that trapped O, and not individual peroxide molecules, are the likely precursor for O_2 formation in *fresh laboratory* ice samples (Matich et al., 1993; Johnson et al., 2003).

However, a recent publication (Khriachtchev et al., 1997) has shown that the photolysis of H_2O_2 in a solid inert gas matrix also leads to the production of two OH radicals:

$$H_2O_2 \xrightarrow{h\nu} OH + OH \qquad (13)$$

In the gas-phase the OH radicals move away from each other and react with other species leading low yields of H_2O_2. However, in a solid inert gas matrix the OH radicals must first escape from the cage in which they were formed before a localized loss of H_2O_2 can occur. If neither OH escapes they can re-react to reform H_2O_2:

$$OH + OH \xrightarrow{h\nu} H_2O_2 \quad (14)$$

or form the water-oxygen atom complex, $H_2O•O$, identified by Khriachtchev et al. (1997):

$$OH + OH \rightarrow H_2O•O \quad (15)$$

In ice, the species $H_2O•O$ may be the trapped O discussed by Matich et al. (1993). Similarly, irradiation of the water-hydrogen peroxide complex, $H_2O_2•H_2O$, in solid inert gas matrices results in the formation of an $H_2O•O•H_2O$ intermediate (Engdahl and Nelander, 2000) by the photo-decomposition of the H_2O_2 unit to two OH radicals:

$$H_2O_2•H_2O \xrightarrow{h\nu} HO•HO•H_2O \quad (16)$$

and then the formation of the $H_2O•O•H_2O$ intermediate:

$$HO•HO•H_2O \rightarrow H_2O•O•H_2O \quad (17)$$

which in turn rapidly photo-decomposes back to $H_2O_2•H_2O$.

$$H_2O•O•H_2O \rightarrow H_2O_2•H_2O \quad (18)$$

On the other hand, in solid inert gas matrices, the photo-decomposition of H_2O_2 dimer produces an H_2O dimer and O_2 (Engdahl and Nelander, 2002) via the following mechanism. Each peroxide unit produces a pair of OH radicals:

$$H_2O_2 \bullet H_2O_2 \xrightarrow{h\nu} (OH + OH) + (OH + OH) \quad (19)$$

Each pair of radicals can then form an $H_2O \bullet O$ complex:

$$(OH + OH) + (OH + OH) \rightarrow H_2O \bullet O + H_2O \bullet O \quad (20)$$

However, the highly reactive O atoms very rapidly react with one another to form O_2:

$$H_2O \bullet O + H_2O \bullet O \rightarrow H_2O \bullet H_2O + O_2 \quad (21)$$

Engdahl and Nelander (2002) report that the H_2O_2 dimer decomposes significantly faster than the H_2O_2 monomer which, in turn, decomposes faster than the $H_2O_2 \bullet H_2O$ complex. The high rates of reactions (10) to (12) are important because they make this pathway of O_2 production very efficient. The intermediate species have short lifetimes and are thus unlikely to take part in parasitic side reactions that would reduce O_2 production.

An alternative, primary pathway for O_2 formation in ice is the direct reaction of an O atom with a previously trapped O atom (Johnson et al., 2003) and may be the principal pathway in laboratory studies of *fresh laboratory* ice samples. However, trapped O and freshly produced O are highly reactive, so at first sight, it would seem likely that direct combination of O atoms might occur on a small scale, but not on a

large enough scale to account for the relatively large abundance of O_2 observed on Ganymede (Spencer and Calvin, 1995).

The purpose of the model proposed here is to solve this problem by providing an efficient pathway to O_2 formation after peroxide inclusions have been formed**.** Each peroxide molecule in the dimer contributes an O atom in the same cage, so diffusion of O through the ice lattice to react with another O atom is not required. Therefore, once formed the peroxide inclusions provide a previously unknown, but effective way of producing O_2.

3.3.3 The Formation of H_2O_2 Aggregates in Water Ice

It has been reported that in H_2O ice, H_2O_2 tends to form microcrystals (Gurman et al., 1967). Thus, dilute frozen mixtures of ice will tend to have H_2O_2 present in aggregates within the H_2O matrix rather than being uniformly distributed. This result is not entirely unexpected. The binding energy of the H_2O_2 dimer is calculated to be 6.31 kcal/mol (Engdahl et al., 2001) whereas the H_2O dimer has a binding energy of 4.94 kcal/mol (Schütz et al., 1997). Presumably this greater binding energy for the H_2O_2 dimer is due to the additional oxygen atom in H_2O_2 that allows two hydrogen bonds per dimer instead of one hydrogen bond per dimer for the H_2O dimer. It is therefore, not unreasonable to think that H_2O_2 molecules will preferably form aggregates in H_2O ices due to this higher binding energy. Segregation of species with different cohesive energies during annealing of solids, is well established (e.g. Johnson and Jesser, 1997). Differential thermography was used (Gurman et al., 1967) to establish the presence of microcrystals of H_2O_2 in frozen H_2O_2/H_2O mixtures. A similar technique could be used on irradiated ice to determine the presence of any such H_2O_2 microcrystals.

Once these aggregates have been formed in laboratory ice, radiolytic or photolytic processes might efficiently form O_2 molecules as described above in Section 3.3.2. The O_2 formed in these inclusions may also be more stable than O_2 trapped in ice. The higher binding energy between H_2O_2 molecules, compared with H_2O molecules, may reduce the ability of O_2 to diffuse out of the ice. Under attack by mobile H, the O_2 may form HO_2 and eventually cycle back to H_2O_2 via the reaction:

$$HO_2 + HO_2 \longrightarrow H_2O_2 + O_2 \quad . \tag{22}$$

Additionally, Gurman and Sergeev (1970) have measured the quantum yields of HO_2 and O_2 formation in photolysed frozen H_2O_2 solutions. The reaction shown above (13) was thought to be the major pathway for O_2 production in their experiments. That is, two HO_2 radicals, detected by electron paramagnetic resonance (EPR) spectroscopy, react to produce O_2 upon warming the frozen solution to room temperature. When the quantum yields of HO_2 and O_2 formation were compared, it was found that the amount of O_2 produced could not come from reaction (13) alone. In view of the recent matrix isolation work of Engdahl and Nelander (2002), it would appear likely that the cause of this extra O_2 is the photolysis of H_2O_2 dimer to produce H_2O and O_2 as described in Section 3.3.2.

3.3.4 O_2 Formation on Ganymede and Europa

The primary radiation products from photolysed ice are OH and H (1). H atoms are very mobile within the ice lattice and on forming H_2 are lost from the icy surfaces to the tenuous atmospheres surrounding the satellites (Johnson et al., 2003). The OH radical however can remain trapped in the ice lattice, recombining with H to reform H_2O, or reacting with other species to form secondary and higher order radiation

products. One such secondary product is H_2O_2 that is produced from the reaction of two OH radicals (2). The long irradiation and annealing times of the icy surfaces of Ganymede and Europa might result in highly localised aggregates of H_2O_2 as described in Section 3.3.3. Once these inclusions of H_2O_2 are formed, radiolytic or photolytic processes may result in O_2 formation as described in section 3.3.2.

It is known from the oxygen observations that the absorptions arise from O_2 dimers present at solid-state densities (Calvin et al. 1996). Due to the low fluxes and long annealing times this O_2 can accumulate and form inclusions in ice (Johnson and Jesser 1997; Johnson 1999). Recent work by Chaabouni et al (2000) has shown that a species can remain trapped in ice at temperatures above its sublimation point. However, the stability of these inclusions over times of the order of years at the temperatures relevant to Ganymede and Europa, has been questioned (Baragiola and Bahr 1998; Baragiola et al. 1999). If these criticisms are correct, then a more stable cage may be needed to obtain the observed absorption bands. This is also suggested by the fact that these bands are considerably distorted from laboratory observations of solid or liquid O_2 (Calvin et al. 1996).

Since H_2O_2 has been observed in the icy satellite surfaces (Carlson et al., 1999), it is possible that the stability and density of the trapped O_2 needed to explain the relative band depths and shapes of the 573 and 627 nm absorptions at temperatures that range between ~ 60-120 K can be explained by O_2 formation and trapping in H_2O_2 inclusions. Measurements are clearly needed to confirm this and to identify the spectral shifts associated with the peroxide inclusions.

The process described here does not impinge upon the discussions of the interesting experiments in which O_2 is produced by irradiation of freshly formed ice samples (Reimann et al. 1984; Matich et al. 1993; Sieger et al. 1998). Since the satellite surfaces have been irradiated and annealed at low temperatures for long periods of time, they can be very different from the fresh ice surfaces studied in the laboratory. Whereas O_2 is formed inefficiently in a fresh ice sample, probably requiring the occurrence of pairs of low probability dissociation events of the type $H_2O + h\nu \rightarrow H_2 + O$ (Johnson et al. 2003), the situation is very different once H_2O_2 inclusions have been formed. Single excitation events can then efficiently lead to O_2 production. This model could be readily tested in the laboratory by the study of absorption spectra versus dose in the radiolysis or photolysis of peroxide inclusions in ice. In addition, the spectral shifts of the O_2 absorption bands in an H_2O_2 matrix could be measured and compared with the shifts measured in space observations, and the amounts of H_2O_2 and O_2 in the icy surfaces should be related.

Models for forming O_2 on the Galilean satellites might be distinguished by observations. Solid O_2 cold trapped from the atmosphere has been suggested (Baragiola and Bahr 1998). This could be stable in very cold (night time, polar or shaded) regions, but would begin to rapidly evaporate when exposed to the visible light by which it is observed. The presence of O_2 in hydrogen peroxide inclusions suggested here, rather than O_2 trapped as inclusions in ice (Johnson and Jesser 1997), should show a correlation with the observed distribution of hydrogen peroxide, allowing for differences in absorbance.

3.3.5 Conclusions

A new mechanism has been proposed in which the trapped O_2 seen on the icy satellites is formed by radiolysis or photolysis in H_2O_2 inclusions. This mechanism is based upon two overlapping ideas. Firstly, after long annealing times, even at relatively low temperatures, H_2O_2 is likely to be present as aggregates in ice lattices. Such inclusions have been shown to occur experimentally in pure ice (Gurman et al. 1967) and their presence is consistent with theoretical calculations (Engdahl et al. 2001) which indicate that H_2O_2 dimers have a greater binding energy than H_2O dimers. The extra binding energy in aggregates of H_2O_2 may provide a greater hindrance to the loss of O_2 by diffusion than would an H_2O lattice.

Secondly, dimers of H_2O_2 in a frozen matrix produce O_2 efficiently when irradiated (Engdahl and Nelander, 2002). This relies on the cage effect, which limits the escape of OH radicals from the volume in which they are formed. Oxygen inclusions in pure ice are unstable at the temperatures of interest. However, O_2 may be formed efficiently in H_2O_2 aggregates and remain trapped because of greater H_2O_2 lattice binding energy. This may account for the observed solid O_2 absorption bands on Ganymede and Europa.

APPENDIX A – Wavelengths and Intensities for the Electronic Transitions of Gas Phase O_2

Transition	Wavelength/nm (vibronic band in parenthesis)	Oscillator Strength	Integrated Absorption Cross Sections ($cm^2\ cm^{-1}\ molecule^{-1}$)	Ref
$a\ ^1\Delta_g - X\ ^3\Sigma_g^-$ Near-Infrared Atmospheric Oxygen	1269 (0,0)	1.20×10^{-11}	1.07×10^{-23}	1
	1065 (1,0)	1.70×10^{-12}	1.50×10^{-24}	
$b\ ^1\Sigma_g^+ - X\ ^3\Sigma_g^-$ Atmospheric System	762.1 (0,0)	2.42×10^{-10}	2.14×10^{-22}	2
	688.4 (1,0)	1.70×10^{-11}	1.50×10^{-23}	
$c\ ^1\Sigma_u^- - X\ ^3\Sigma_g^-$ Herzberg II System	292.6 (2,0)	6.78×10^{-14}	6.00×10^{-26}	3
	286.6 (3,0)	2.26×10^{-13}	2.00×10^{-25}	
	281.2 (4,0)	5.31×10^{-13}	4.70×10^{-25}	
	276.1 (5,0)	9.94×10^{-13}	8.80×10^{-25}	
	271.2 (6,0)	1.67×10^{-12}	1.48×10^{-24}	
	267.3 (7,0)	2.52×10^{-12}	2.23×10^{-24}	
	263.5 (8,0)	3.50×10^{-12}	3.10×10^{-24}	
	260.0 (9,0)	4.52×10^{-12}	4.00×10^{-24}	
	256.9 (10,0)	5.31×10^{-12}	4.70×10^{-24}	
	254.1 (11,0)	6.33×10^{-12}	5.60×10^{-24}	
	251.6 (12,0)	7.35×10^{-12}	6.50×10^{-24}	
	249.4 (13,0)	6.44×10^{-12}	5.70×10^{-24}	
	247.6 (14,0)	6.78×10^{-12}	6.00×10^{-24}	
	246.0 (15,0)	6.67×10^{-12}	5.90×10^{-24}	
	244.7 (16,0)	5.09×10^{-12}	4.50×10^{-24}	
	243.8 (17,0)	4.07×10^{-12}	3.60×10^{-24}	
	243.1 (18,0)	2.26×10^{-12}	2.00×10^{-25}	

$A'\,^3\Delta_u - X\,^3\Sigma_g^-$ Herzberg III System[b]	277.1 (2,0)[c]	278.2 (2,0)[d]	3.84×10^{-13}	3.40×10^{-25}	3
	271.6 (3,0)[c]	272.7 (3,0)[d]	1.15×10^{-12}	1.02×10^{-24}	
	266.6 (4,0)[c]	267.7 (4,0)[d]	2.68×10^{-12}	2.37×10^{-24}	
	262.0 (5,0)[c]	263.0 (5,0)[d]	5.24×10^{-12}	4.64×10^{-24}	
	257.9 (6,0)[c]	258.9 (6,0)[d]	8.72×10^{-12}	7.72×10^{-24}	
	254.2 (7,0)[c]	255.1 (7,0)[d]	1.22×10^{-11}	1.08×10^{-23}	
	250.9 (8,0)[c]	251.8 (8,0)[d]	1.58×10^{-11}	1.40×10^{-23}	
	248.1 (9,0)[c]	248,9 (9,0)[d]	1.73×10^{-11}	1.53×10^{-23}	
	245.7 (10,0)[c]	246.5 (10,0)[d]	1.79×10^{-11}	1.58×10^{-23}	
	243.9 (11,0)[c]	244.6 (11,0)[d]	1.35×10^{-11}	1.19×10^{-23}	
	242.7 (12,0)[c]	243.3 (12,0)[d]	6.97×10^{-12}	6.17×10^{-24}	
$A\,^3\Sigma_u^+ - X\,^3\Sigma_g^-$ Herzberg I System	285.6 (0,0)		8.36×10^{-14}	7.40×10^{-26}	3
	279.5 (1,0)		8.02×10^{-13}	7.10×10^{-25}	
	273.8 (2,0)		3.73×10^{-12}	3.30×10^{-24}	
	268.6 (3.0)		1.11×10^{-11}	9.82×10^{-24}	
	263.8 (4,0)		2.51×10^{-11}	2.22×10^{-23}	
	259.4 (5,0)		5.09×10^{-11}	4.50×10^{-23}	
	255.5 (6,0)		8.36×10^{-11}	7.40×10^{-23}	
	252.0 (7,0)		1.22×10^{-10}	1.08×10^{-22}	
	248.9 (8,0)		1.57×10^{-10}	1.39×10^{-22}	
	246.4 (9,0)		1.79×10^{-10}	1.58×10^{-22}	
	244.4 (10,0)		1.64×10^{-10}	1.45×10^{-22}	
	243.0 (11,0)		9.15×10^{-11}	8.10×10^{-23}	
$B\,^3\Sigma_u^- - X\,^3\Sigma_g^-$ Schumann – Runge System	202.6 (0,0)		3.45×10^{-10}	3.05×10^{-22}	4,5
	199.8 (1,0)		3.90×10^{-9}	3.45×10^{-21}	
	197.2 (2,0)		2.38×10^{-8}	2.10×10^{-20}	
	194.8 (3,0)		9.90×10^{-8}	8.75×10^{-20}	
	192.4 (4,0)		3.21×10^{-7}	2.84×10^{-19}	
	190.3 (5,0)		8.52×10^{-7}	7.53×10^{-19}	
	188.2 (6,0)		1.91×10^{-6}	1.69×10^{-18}	
	186.4 (7,0)		3.81×10^{-6}	3.37×10^{-18}	
	184.7 (8,0)		6.68×10^{-6}	5.91×10^{-18}	
	183.1 (9,0)		1.06×10^{-5}	9.39×10^{-18}	
	181.6 (10,0)		1.57×10^{-5}	1.39×10^{-17}	
	180.4 (11,0)		2.09×10^{-5}	1.85×10^{-17}	

08Continued from previous page		
179.3 (12,0)	2.53×10^{-5}	2.24×10^{-17}
178.3 (13,0)	2.88×10^{-5}	2.55×10^{-17}
177.5 (14,0)	3.03×10^{-5}	2.68×10^{-17}
176.8 (15,0)	2.92×10^{-5}	2.58×10^{-17}
176.3 (16,0)	2.59×10^{-5}	2.29×10^{-17}
175.9 (17,0)	2.23×10^{-5}	1.97×10^{-17}
175.6 (18,0)	1.83×10^{-5}	1.62×10^{-17}
175.3 (19,0)	1.44×10^{-5}	1.27×10^{-17}

a) *The Herzberg I bands were measured predominantly at low pressures to prevent possible interference from Herberg II and III lines. Herzberg II and III bands can only be measured at higher pressures because they are much weaker transitions than the Herzberg I transitions.*

b) *Although the A' $^3\Pi_u$ state should produce 3 sub-bands due to spin-orbit coupling, it was found that the Ω=3 sub-band only accounted for ca. 10% of the integrated absorption cross section for each vibrational level and has thus been omitted from this table. The relevant data was also incomplete due to the difficulty of detecting such a weak series of lines. Oscillator strength and integrated absorption cross sections are calculated as the sum of the Ω=1,2,3 bands.*

c) *Ω=1 band*

d) *Ω=2 band*

[1] Smith and Newnham, 2000, [2] Newnham and Ballard, 1998, [3] Mèrienne et al., 2000, [4] Ackerman et al., 1970, [5] Fugol et al., 1976.

APPENDIX B – Wavelengths and Intensities for the Electronic Transitions of Solid Phase O_2[a]

Transition	Wavelength/nm (vibronic band in parenthesis)	Oscillator Strength	Integrated Absorption Cross Sections ($cm^2\ cm^{-1}\ molecule^{-1}$)	Method/State
$a\ ^1\Delta_g - X\ ^3\Sigma_g^-$	1252 (0,0)	2.0×10^{-7}	1.8×10^{-19}	α–O_2 20.6 K
	1056 (1,0)	6.6×10^{-8}	5.9×10^{-20}	
	914.9 (2,0)	9.7×10^{-9}	8.6×10^{-21}	
	808.9 (3,0)	1.8×10^{-9}	1.6×10^{-21}	
$b\ ^1\Sigma_g^+ - X\ ^3\Sigma_g^-$	756.4 (0,0)	9.7×10^{-9}	8.6×10^{-21}	α–O_2 20.6 K
$a\ ^1\Delta_g + a\ ^1\Delta_g - X\ ^3\Sigma_g^- + X\ ^3\Sigma_g^-$	627.1 (0,0)	3.9×10^{-7}	3.4×10^{-19}	α–O_2 20.6 K
	576.3 (1,0)	4.3×10^{-7}	$3.8 \times 10^{--19}$	
	531.7 (2,0)	3.1×10^{-8}	2.8×10^{-20}	
	494.2 (3,0)	6.2×10^{-9}	5.5×10^{-21}	
$a\ ^1\Delta_g + a\ ^1\Delta_g - X\ ^3\Sigma_g^- + X\ ^3\Sigma_g^-$	628.1 (0,0)	1.1×10^{-7}	9.6×10^{-20}	β–O_2 ~35 K
	577.4 (1,0)	1.2×10^{-7}	1.0×10^{-19}	
	532.5 (2,0)	2.3×10^{-8}	2.0×10^{-20}	
	494.6 (3,0)	2.9×10^{-9}	2.5×10^{-21}	
$a\ ^1\Delta_g + a\ ^1\Delta_g - X\ ^3\Sigma_g^- + X\ ^3\Sigma_g^-$	629.7 (0,0)	2.5×10^{-8}	2.2×10^{-20}	γ–O_2 ~49 K
	577.7 (1,0)	4.8×10^{-8}	4.3×10^{-20}	
	532.8 (2,0)	2.7×10^{-9}	2.4×10^{-21}	
$a\ ^1\Delta_g + b\ ^1\Sigma_g^+ - X\ ^3\Sigma_g^- + X\ ^3\Sigma_g^-$	474.8 (0.0)	2.8×10^{-8}	2.5×10^{-20}	α–O_2 20.6 K
	446.0 (1,0)	1.6×10^{-8}	1.4×10^{-20}	
	419.9 (2,0)	9.0×10^{-9}	7.9×10^{-21}	
	397.2 (3,0)	9.7×10^{-10}	8.6×10^{-22}	
$a\ ^1\Delta_g + b\ ^1\Sigma_g^+ - X\ ^3\Sigma_g^- + X\ ^3\Sigma_g^-$	476.2 (0,0)	8.4×10^{-9}	7.4×10^{-21}	β–O_2 ~35 K
	447.1 (1,0)	6.8×10^{-9}	6.0×10^{-21}	
$a\ ^1\Delta_g + b\ ^1\Sigma_g^+ - X\ ^3\Sigma_g^- + X\ ^3\Sigma_g^-$	477.0 (0,0)	3.3×10^{-9}	2.9×10^{-21}	γ–O_2 ~49 K

$b\,^1\Sigma_g^+ + b\,^1\Sigma_g^+ - X\,^3\Sigma_g^- + X\,^3\Sigma_g^-$	378.4 (0,0)	1.7×10^{-8}	1.5×10^{-20}	
	360.8 (1,0)	4.7×10^{-8}	4.1×10^{-20}	α–O_2 20.6 K
	343.7 (2,0)	3.1×10^{-8}	2.8×10^{-20}	

a) Integrated absorption cross sections calculated from Landau et al, 1962.

REFERENCES

Ackerman, M.; Biaumé, F.; Kockarts, G., 1970. *Planet. Space Sci*. **18**, 1639.

Acquista, N.; Shoen, L. J.; Lide, D. R., Jr., 1968, *J. Chem. Phys*. **48**, 1534.

Ayers, G. P.; Pullin, A. D. E., 1976. *Spectrochim. Acta* **32A**, 1629.

Baragiola, R. A.; Bahr, D. A. 1998. *J. Geophys. Res*. **103**, 25865.

Baragiola, R. A.; Atteberry, C. L.; Bahr, D. A., 1999. *J. Geophys. Res*. **E104**, 14183.

Bentwood, R. M.; Barnes, A. J.; Orville-Thomas, W. J., 1980. *J. Mol. Spec*. **54**, 391.

Brus, L. E.; Bondybey, V. E., 1975. *J. Chem. Phys.* **63**, 786

Budzien, S. A.; Feldman, P. D., 1991, *Icarus* **90***,* 308.

Byers Brown, W., 1995. *Chem. Phys. Lett.* **235**, 94.

Byers Brown, W.; Vincent, M. A.; Trollope, K.; Hillier, I. H., 1992. *Chem. Phys. Lett.* **192**, 213.

Cacace, F.; De Petris, G.; Pepi, F.; Troiani, A., 2000 *Angew. Chem., Inter. Ed.*, **39**. 367.

Cairns B. R.; Pimentel, G. C., 1965. *J. Chem. Phys.* **43**, 3432.

Calvin, W. M.; Johnson, R. E.; Spencer, J. R., 1996. *Geophys. Res. Lett.* **23**, 673.

Calvin, W. M., and Spencer, J. R., 1997. Icarus 120, 505-516.

Calvin, W. M.; Anicich, V. G.; Brown, R. H., 2002, unpublished work.

Carlson, R.W.; Johnson, R. E.; Anderson, M.S., 1999a. *Science* **286**, 97.

Carlson, R. W.; Anderson, M. S.; Johnson, R. E.; Smythe, W. D.; Hendrix, A. R.; Barth, C. A.; Soderblom, L. A.; Hansen, G. B.; McCord, T. B.; Dalton, J. B.; Clark, R. N.; Shirley, J. H.; Ocampo, A. C.; Matson, D. L., 1999b. *Science* **283**, 2062.

Chaabouni, H.; Schriver-Mazzuoli, L.; Schriver A., 2000. *J. Phys. Chem. A* **104**, 1962.

Cheng, B.-M.; Lee, Y.-P.; Ogilvie, J. F., 1988. *Chem. Phys. Lett*. **151**, 109.

Cooper, J.F.; Johnson, R.E.; Mauk, B.H.; Garrett, H.B.; Gehrels, N., 2001. *Icarus* **149**, 133.

Coussan, S.; Loutellier, A.; Perchard, J. P., Racine, S, Bouteiller Y., 1998. *J. Mol. Struct*., **471**, 37.

Daniel, J. S.; Solomon, S.; Kjaergaard, H. G.; Schofield, D. P., 2004 *Geophys. Res. Lett.* **31**, L06118

Dianov-Klokov, V. I., 1966. *Optika i Spektroskopiya* **20**, 954.

Ellis, J. W.; Kneser, H. O., 1933. *Z. Physik* **86**, 583.

Engdahl, A.; Nelander, B., 1989. *Mol. Struct*. **193**, 101.

Engdahl, A.; Nelander, B., 1996. *Chem. Phys*. **213**, 333.

Engdahl, A.; Nelander , B., 2000. *Phys. Chem. Chem. Phys*. **2**, 3967.

Engdahl, A.; Nelander, B.; Karlström, G., 2001. *J. Phys. Chem. A* **105**, 8393.

Engdahl, A.; Nelander, B., 2002. *Phys. Chem. Chem. Phys*. **4**, 2140.

Engdahl, A.; Karlström, G.; Nelander, B. J., 2003. *Chem. Phys*. **118**, 7797.

Feldman, P. D., 1996. In: *Atomic, Molecular, & Optical Physics Handbook*, Ed. G. W. F. Drake, American Institute of Physics, New York.

Fugol, I. Ya.; Gimpelevich, L. G.; Timchenko, L. I., 1976. *Opt. Spectrosc*. **40**, 159.

Gehrels, T. 1976, *Jupiter: Studies of the interior, atmosphere, magnetosphere and satellites*, The University of Arizona Press, Tucson.

Gerakines, P. A.; Schutte, W. A.; Ehrenfreund, P., 1996. *Astron. Astrophys*., **312**, 289.

Ghormley, J.; Hochanadel, C., 1971. *J. Chem. Phys.* **75***,* 40.

Goodman, J.; Brus, L.E., 1977 *J. Chem. Phys.*, **67**, 4858.

Grodent, D.; Clarke, J. T.; Waite Jr., J. H.; Cowley, S. W. H.; Gérard, J.-C.; Kim, J., 20003, *J. Geophys. Res.,* **108**, 1366.

Grundy, W. M.; Buie, M. W.; Stansberry, J. A.; Spencer, J. R.; Schmitt B., 1999 *Icarus*, **142**, 536.

Gurman, V. S.; Batyuk, V. A.; Sergeev, G. B., 1967. *Kinetika i Kataliz* **8**, 527.

Gurman, V. S.; Sergeev, G. B., 1970. *Russian J. Phys. Chem.* **44**, 601.

Hansen, J. C.; Francisco, J. S., 2002. *ChemPhysChem*, **3**, 833.

Heidt L. J.; Ekstrom, L., 1957. *J. Am. Chem. Soc.* **79**, 1260.

Herzberg, G., 1932. *Naturwissenschatten* **20**, 577.

Herzberg, G., 1953. *Can. J. Phys.* **31**, 657.

Hobza, P.; Zahradník, R. J., 1977. *Theor. Biol*. **66**, 461.

Huber, K.P.; Herzberg, G., 1979 *Molecular Spectra and Molecular Structure, Volume 4: Constants of Diatomic Molecules*; van Nostrand Reinhold, New York.

Hudson, R. D.; Carter, V. L., 1968. *J. Opt. Soc. Amer.* **58**, 1621.

Johnson, R. E.; Jesser, W. A ,1997. *Astrophys. J. Lett*. **480**, L79.

Johnson, R. E.; Quickenden, T. I., 1997. *J. Geophys. Res*. **102**, 10,985.

Johnson, R. E., 1999. J. Geophys. Res. **104**, 14179.

Johnson, R. E., 2001. In: *Advances Series in Physical Chemistry, Vol. 11: Chemical Dynamics in Extreme Environments*, Ed. R. Dessler, World Scientific, Singapore.

Johnson, R. E.; Quickenden, T. I.; Cooper, P. D.; McKinley, A. J.; Freeman, C. G., 2003, *Astrobiology*, **3**, 823.

Johnson T. V.; Soderblom, L. A., 1982, In: *Satellites of Jupiter*, Ed. Morrison, D., The University of Arizona Press, Tucson.

Jordan T. H.; Streib, W. E.; Smith, H. W.; Liscombe, W. N.; 1964. *Acta Cryst.* **17**, 777.

Khriachtchev, L.; Pettersson, M.; Jolkkonen, S.; Pehkonen, S.; Rasanen, M., 2000. *Chem. Phys*. **112**, 2187.

Kim, K.S.; Kim, H.S.; Jang, J.H.; Kim, H.S., Mhin, B.-J.; Xie, Y.M.; Schaeffer, H.F. III, 1991. *J. Chem. Phys.* **94**, 2057.

Kjaergaard, H. G.; Henry, B. R.; Wei, H.; Lefebvre, S.; Carrington Jr., T.; Mortensen, O. S.; Sage, M. L., 1994. *J. Chem. Phys*. **100**, 6228.

Kjaergaard, H. G.; Low, G. R.; Robinson, T. W.; Howard, D. L.; 2002. *J. Phys. Chem. A* **106**, 8955.

Kjaergaard, H. G.; Robinson, T. W.; Howard, D. L.; Daniel, J. S.; Headrick, J. E.; Vaida, V., 2003. *J. Phys. Chem. A*, **107**, 10680.

Krupenie, P. H., 1972. *J. Phys. Chem. Ref. Data* **1**, 423.

Landau, A.; Allin, E. J.; Welsh, H. L., 1962. *Spectrochim. Acta* **18**, 1.

Langford, 1999. Unpublished work.

Langford, V. S.; McKinley, A. J., Quickenden, T. I., 2000a, *J. Am. Chem. Soc.* **51**, 12859.

Langford, V. S.; McKinley, A. J.; Quickenden, T. I., 2000b, *Acc. Chem. Res*., **33**, 665.

Long, C. A., Ewing, G. E., 1971. *Chem. Phys. Lett.* **9**, 225.

Low, G. R.; Kjaergaard, H. G., 1999. *J. Chem. Phys*. **110**, 9104.

Lucchitta, B. K.; Soderblum, L. A., 1982, In: *Satellites of Jupiter*, Ed. Morrison, D., The University of Arizona Press, Tucson.

Matich, A. J.; Bakker, M. G.; Lennon, D.; Quickenden, T. I.; Freeman, C. G., 1993. *J. Phys. Chem.* **97**, 10,539.

McCord, T. B.; Hansen, G. B.; Matson, D. L.; Johnson, T. V.; Crowley, J. K.; Fanale, F. P.; Carlson, R. W.; Smythe, W. D.; Martin, P. D.; Hibbitts, C. A.; Granahan, J. C.; Ocampo, A.; 1999a. *J. Geophys. Res.* **104**, 11,827.

McCord, T. B.; Hansen, G. B.; Shirley, J. H.; Carlson, R. W.; 1999b. *J. Geophys. Res.* **104**, 27,157.

Merienne, M.; Jenouvrier, A.; Coquart, B.; Carleer, M.; Fally, S.; Colin, R.; Vandaele, A. C.; Hermans, C., 2000. *J. Mol. Spectrosc.* **202**, 171.

Molina, L. T.; Schinke, S. D.; Molina, M. J., 1977. *Geophys. Res. Lett.* **4**, 580.

Mulliken, R. S., 1928. *Phys. Rev.* **32**, 880.

Nelander, B. J., 1997. *Phys. Chem. A*, **101**, 9092.

Newnham, D. A.; Ballard, J., 1998. *J. Geophys. Res.* **103**, 28,801.

Noll, K. S.; Johnson, R. E.; Lane, A. L.; Domingue, D. L.; Weaver, H. A.; 1996. *Science* **273**, 341.

Noll, K. S.; Roush, T. L.; Cruishank, D. P.; Johnson, R. E.; Pendleton, Y. J., 1997. *Nature* **388**, 45.

Orlando, T. M.; Sieger, M. T., 2003. *Surf. Sci*. **528**, 1.

Orton, G. S.; Spencer, J. R.; Travis, L. D.; Martin, T. Z.; Tamppari, L. K., 1996. *Science* **274**, 389.

Palmer, I. J.; Byers Brown, W.; Hillier, I. H., 1996. *J. Chem. Phys.* **104**, 3198.

Paranicas, C.; Carlson, R. W.; Johnson, R.E., 2001. *Geophys. Res. Lett*. **28**, 673.

Perchard, J. P., 2001. *Chem. Phys*. **273**, 217.

Reimann, C. T.; Boring, J. W.; Johnson, R. E.; Garrett, J. W.; Farmer, K. R.; Brown, K. J.; Marcantonio W. L.; and Augustyniak, W. M., 1984. *Surf. Sci*. **147**, 227.

Robinson, G. W.; McCarty, M. Jr, 1958a. *Chem. Phys.* **28**, 350.

Robinson, G. W.; McCarty, M. Jr, 1958b. *Can. J. Phys.* **36**, 1590.

Roder, H. M., 1978. *J. Phys. Chem. Ref. Data* **7**, 949.

Romand, M. J.; Granier-Mayence, J. 1954. *J. Phys. Radium* **15**, 62.

Schofield D. P.; Kjaergaard, H. G., 2004. *J. Chem. Phys*. **120**, 6930.

Schütz, M.; Brdarski, S.; Widmark, P.-O.; Lindh, R.; Karlström, G., 1997. *J. Chem. Phys*. **107**, 4597–4605.

Selby, B. J., Quickenden, T. I., Freeman, C. G., 2004, submitted.

Shardanand, 1969. *Phys. Rev.* **186**, 5.

Sieger, M. T.; Simpson, W. C.; Orlando, T. M., 1998. *Nature* **394**, 554.

Sill, G. T.; Clark, R. N. 1982, In: *Satellites of Jupiter*, Ed. Morrison, D., The University of Arizona Press, Tucson.

Slanger, T.G.; Cosby, P.C., 1988. *J. Phys. Chem.* **92**, 267.

Smith, K. M., Newnham, D. A., 1999. *Chem. Phys. Lett.* **308**, 1.

Smith, K. M.; Newnham, D. A., 2000. *J. Geophys. Res.* **105**, 7383.

Spencer, J. R.; Calvin, W. M.; Person, M. J., 1995. *J. Geophys. Res.* **100**, 19,049.

Spencer, J. R.; Calvin, W. M., 2002 *Astron. J.* **124**, 3400.

Spohn, T.; Schubert, G., 2003, *Icarus* **161**, 456.

Suzer, S.; Andrews, L., 1988. *J. Chem. Phys*., **88**, 916.

Svishchev, I. M.; Boyd, R. J., 1998. *J. Phys. Chem. A* **102**, 7294.

Taub, I. A.; Eiben, K., 1968. *J. Chem. Phys.* **49**, 2499.

Tinti, D. S., 1968 *J. Chem. Phys.*, **48**, 1459.

Vaghjiani, G. L.; Turnipseed, A. A.; Warren, R. F.; Ravishankara, A. R., 1992. *J. Chem. Phys*. **96**, 5878.

Vaida, V.; Headrick, J. E., 2000. *J. Phys. Chem. A* **104**, 5401-5412.

Vidal, R. A.; Bahr, D. A.; Baragiola, R. A.; Peters. M., 1997. *Science* **276**, 1839.

Wang, B.; Hou, H.; Gu, Y., 1999. *Chem. Phys. Lett*. **94**, 2057.

Wayne, R. P., 1991.*Chemistry of Atmospheres, 2nd Ed*.; Clarendon Press: Oxford.

Xie, J.; Enderle, M.; Knorr, K.; Jodl, H., 1997. *J. Phys Rev. B*, **55**, 8194.

Xie, Y. M.; Schaeffer, H. F. III, 1993. *J. Chem. Phys.* **98**, 8829.